Forecasting Vortex Filaments

A thesis
submitted in partial fulfilment
of the requirements for the Degree
of

Master of Science in Physics

in the

University of Canterbury

by

Christopher J Noble

University of Canterbury
Christchurch, New Zealand
1998

PHYSICAL
SCIENCES
LIBRARY
THESIS
Copy 2

Abstract

The accuracy of stratospheric forecasts from the United Kingdom Meteorological Office's (UKMO) assimilation system in the Southern Hemisphere (SH) are studied primarily for a period in October 1994 and also February 1995. Conventional root mean square error (RMSE) calculations for different regions show that stratospheric forecasts are a large improvement over persistence in October 1994 (SH winter) even at five days but not so during February 1995 (SH summer). Systematic errors in the temperature and zonal wind fields were found to occur in relation with the stratopause and polar jet respectively. Studies also show that in general the vortex minimum temperature is forecast too cool and the maximum wind in the polar jet is forecast too strong. An advection scheme on specialised parcel location fields is used to study the differences in the meridional component of the wind vector with results indicating the forecast winds are highly consistent with the analysed winds even after five days in most cases. A back-trajectory mapping technique is employed to generate high-resolution maps of isentropic potential vorticity to permit the study of small-scale structure. The overall structure in a total hemisphere field produced from forecast winds is very similar to that from analysed winds even for filamentary structure near the polar vortex. Qualitative comparisons of aircraft measured tracer structure during the Airborne Southern Hemisphere Ozone Experiment (ASHOE) 1994 with structure from the high-resolution potential vorticity maps shows that large-scale features are represented well by the back-trajectory mapping technique with possibly less success for small-scale structure.

For Mum.

"Every theory of the course of events in nature is necessarily based on some process of simplification of the phenomena and is to some extent therefore a fairy tale."

N Shaw, 1926

Contents

List of Figures

List of Tables

Chapter 1

Introduction

The atmosphere can loosely be described as the layer of air surrounding the Earth. More formally it may be described as that gaseous mixture that surrounds a planet and extends vertically away from it dropping in density with height. We depend on it for survival along with the other animal and plant life co-existing on the surface. Our two nearest terrestrial neighbours also have atmospheres, although they are virtually uninhabitable to us. The atmospheres of both Venus and Mars are composed of roughly 95% carbon dioxide with smaller percentages of nitrogen, argon, and oxygen among others [*Zeilick and Smith (1987)*]. Venus has a runaway greenhouse effect due to thick sulphuric acid clouds causing surface temperatures of hundreds of degrees Celsius with atmospheric pressure almost 100 times higher than here on Earth. Mars on the other hand is a very cold planet with no liquid water to speak of. Temperatures rarely climb above freezing and are often similar to those in Antarctica with an atmospheric pressure around 100 times lower than Earth's.

Here on Earth the composition is roughly 78% molecular nitrogen, 21% molecular oxygen along with much smaller percentages of argon, carbon dioxide, water, hydrogen, helium and substances such as industrial pollutants for example carbon monoxide, nitrogen dioxide etc. [*Zeilick and Smith (1987)*]. The surface temperature varies greatly but is generally around 20°C give or take 20°C or so and the atmospheric pressure is normally in the range 990-1030hPa at the surface. But how do these quantities vary with height? The composition remains roughly the same to a height of ~100km due to turbulent motions and mixing, above which molecular diffusion is able to dominate separating the species to different heights. The lower region is called the homosphere while above 100km is termed the heterosphere. Pressure falls off exponentially as you head away from the surface vertically but more interesting is the temperature variation with height which leads to different regions with individual thermal characteristics.

The troposphere is the first such region extending to approximately 15km, in which occurs the 'weather' - fronts, storms, clouds, rain etc. and is the region in which nearly all commercial flights take place with only high performance jets and weather balloons extending higher. Above that lies the stratosphere stretching to roughly 50km followed by the mesosphere taking us to 85km and finally the thermosphere. The regions are separated by the tropopause, stratopause and the mesopause and are depicted in figure 1.1.

The structure in the temperature profile can be explained by various processes of absorption and emission of solar and terrestrial radiation by different species throughout the atmosphere. As solar radiation enters the Earth's atmosphere the first components to be absorbed out are the shortest wavelengths in the ultraviolet (UV) part of the spectrum. Above 85km the photodissociation of molecular oxygen into excited atomic oxygen is the main process providing a heat source for the thermosphere. As the abundance of molecular oxygen falls away so too does the heating thus giving rise to the temperature minimum at the mesopause. By this stage not all of the UV radiation has been absorbed however and still has an important role to play. As it descends it encounters ozone (O_3), which absorbs most of the remaining UV radiation thus providing a strong heat source giving rise to the temperature maximum at the stratopause. This absorption is balanced mainly by infrared emission by carbon dioxide. Lower still and water vapour and clouds play a major role in both the absorption and more importantly the emission of infrared radiation hence the minimum at the tropopause. Finally

we reach the surface where the remaining radiation is absorbed by the Earth, heating the lower atmosphere from below directly and via re-radiation in the infrared.

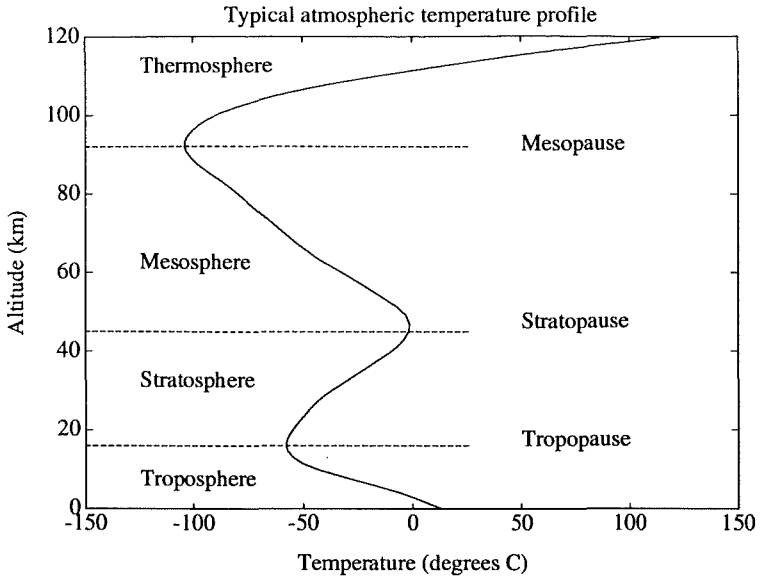

Fig 1.1. A typical atmospheric vertical temperature profile showing the various regions with their temperature characteristics. [after *Dunford (1997)*]

As mentioned above ozone plays an important role in the absorption of ultra-violet radiation. In recent years media attention has focused on the ozone hole that forms in the Antarctic region during late winter and early spring and its relative size compared to previous years. In the summers of 1995/96 and 1996/97, Christchurch's *The Press* regularly printed ozone concentration maps for the polar Southern Hemisphere. An example is given in figure 1.2 for 4 November 1996 showing a large region over the Antarctic with low ozone concentration.

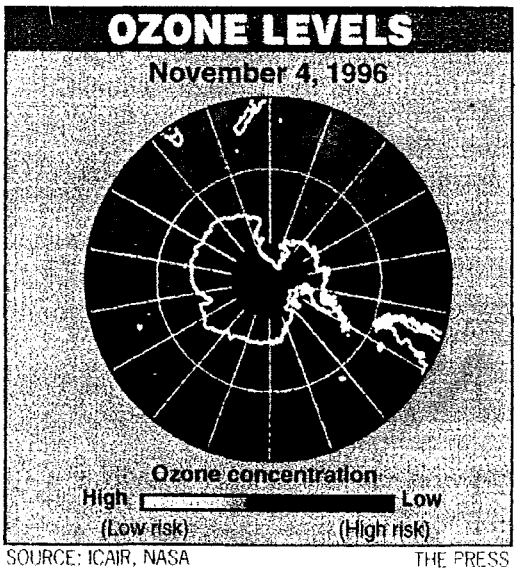

Fig 1.2. An example of the newspaper coverage of Southern Hemisphere ozone depletion, in this case for 4 November 1996. [from *The Press (November 1996)*]

A similar hole also develops in the Northern Hemisphere again following its winter but is not so intense as its southern counterpart. The main cause for concern is that ozone forms a natural barrier between us and most of the sun's harmful rays and a continuing depletion in the layer could be considered to be a potential hazard. Ozone depletion drops away from the pole approaching mid-latitudes, however Antarctic air is transported northward to mid-latitudes exposing humans, animals and plant-life to more harmful ultra-violet radiation than would be otherwise received.

Measurements of stratospheric ozone have been made since the 1960's, the earliest using the Dobson Spectrophotometer and Filter Ozonemeters. Coverage was mostly land-based in the Northern Hemisphere until 1978 when the Total Ozone Mapping Spectrometer (TOMS) was deployed aboard the National Aeronautics and Space Administration's (NASA) Nimbus 7 satellite. Other satellite measurements include those from the Solar Backscatter Ultraviolet Spectrometer (SBUV) aboard Nimbus 7 and also aboard a satellite operated by the National Oceanic Atmospheric Administration (NOAA 11) launched 1 January 1989. The Meteor 3 satellite launched 15 August 1991 also makes TOMS measurements and the Upper Atmosphere Research Satellite (UARS) launched 12 September 1991 carries a Microwave Limb Sounder (MLS) [*Makhijani and Gurney (1995)*]. Supplementing these space-based measurements are many other instruments providing vertical ozone profiles from the ground and by balloon or rocket.

Globally total-column ozone data to early 1994 indicates decreases of ozone in all seasons at mid-latitudes (30°-60°) in both the North and South Hemispheres [*WMO (1994)*]. The trend for the mid-latitude Southern Hemisphere for example averages 4% to 5% per decade [*WMO (1994)*]. Figure 1.3 clearly shows this trend presenting total column ozone values for Christchurch, New Zealand for the period 1978-1993 originating from TOMS data [*Bedorf (1997)*]. A least squares polynomial fit was applied to the average annual total column ozone values revealing a downward trend in total ozone of 8.7% in the 16 year period from 1978-1993.

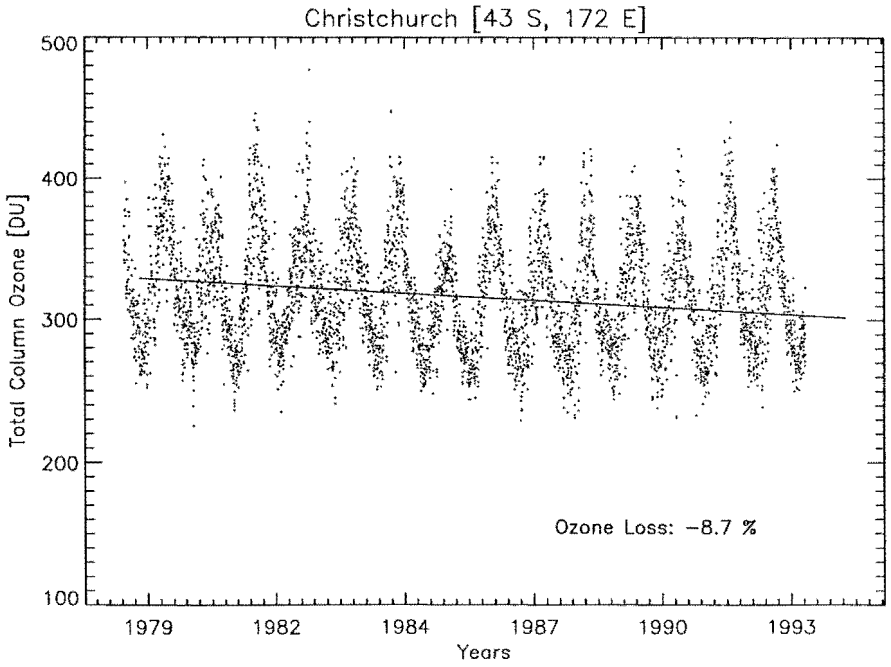

Fig 1.3. Time series plot of total column ozone over Christchurch, NZ for 1978-1993. The ozone loss of 8.7% refers to the entire 16-year period [after *Bedorf (1997)*]

To further enhance our knowledge of ozone processes in the lower stratosphere a number of aircraft studies have been conducted over the years. Previous studies for the Northern Hemisphere include the Airborne Arctic Stratospheric Experiment (AASE) in January and February 1989, the European Arctic Stratospheric Ozone Experiment (EASOE) in the period November 1991 to April 1992 [*Pyle et al. (1994)*] and the Stratospheric Photochemistry, Aerosols and Dynamics Expedition (SPADE) in April and May 1993 [*Waugh et al. (1997)*]. The Southern Hemisphere has also been studied by aircraft in a number of campaigns including the Airborne Antarctic Ozone Experiment (AAOE) in August and September 1989 [*Tuck et al. (1989)*] and the Airborne Southern Hemisphere Ozone Experiment, conducted in concert with, Measurements for Assessing the Effects of Stratospheric Aircraft (ASHOE/MAESA) in the period February to November 1994 [*Tuck et al. (1997)*].

The Airborne Southern Hemisphere Ozone Experiment (ASHOE), was designed to examine ozone loss in the lower Southern Hemisphere stratosphere and how the loss is related to polar, mid-latitude and tropical processes. The second campaign in concert with the first, Measurements for Assessing the Effects of Stratospheric Aircraft (MAESA), aimed to study stratospheric photochemistry and transport for assessing the environmental effects of stratospheric aircraft. Observations for ASHOE/MAESA came primarily from a series of flights of NASA's ER-2 aircraft capable of flying at high altitudes into the lower stratosphere. The ER-2 carried a number of instruments allowing basic meteorological measurements to be made along with observations of various trace gases such as ozone (O_3), nitrous oxide (N_2O), hydrogen chloride (HCl) or chlorine monoxide (ClO), as well as various chlorofluorocarbons (CFC's). During 1994 the ER-2 made 45 flights including test flights with 26 being made from Christchurch, New Zealand during the months March to October. Further observations were also made from the ground, balloons and satellites to supplement the aircraft data. The timing of ASHOE was such to allow the study of stratospheric chemistry through the evolution of the Antarctic polar vortex to its final break-up in early spring. As the vortex begins to break-up, ozone-poor filaments of air are peeled off the vortex edge and transported to mid-latitudes sometimes sweeping over New Zealand.

This study focuses on the Southern Hemisphere spring of 1994 when the ozone hole was well developed and for which data is available from both the ASHOE campaign and the model fields originating from the United Kingdom Meteorological Office's (UKMO) Stratosphere – Troposphere Data Assimilation System. The main aim is to establish the accuracy of the forecast fields originating from the UKMO assimilation system and to determine whether or not we have the ability to predict filaments that are drawn off the polar vortex.

1.1 Thesis Layout

The thesis begins by discussing some basic atmospheric dynamics in chapter two along with giving definitions of quantities used in this study. Chapter three presents the assimilation model, the origins of the data along with how some of the computer code works that is used for the manipulation and eventual presentation of the data. Chapter four provides a description of the circulation of the atmosphere and in particular, processes in the Southern Hemisphere stratosphere. Ozone chemistry is discussed in some detail providing an outline of the many different processes leading to the formation and destruction of ozone in the stratosphere. The results from the study are given in chapter five with discussions on analysis methods and implications of the findings.

The starting point for the results chapter is some basic comparisons between analysed fields and forecast fields to determine the location and size of errors in the predicted stratospheric fields and possible reasons for their presence. Following this a performance study of the forecast fields from the UMKO Data Assimilation System is carried out for available forecasts during October 1994 and in February 1995. Analysis continues with evaluation of the accuracy of the model temperature by comparing output fields, both analysed and forecast, with aircraft measurements made during ASHOE. Next an advection scheme is invoked on specialised particle location fields in both analysed and forecast wind fields to determine the accuracy of the forecast winds at predicting meridional motion. Following that, measurements from ASHOE are examined and compared with high resolution tracer fields generated from a back trajectory analysis scheme to determine if structure observed by the ER-2 could have been predicted from the model forecast fields. The final chapter summarises the results of the study, presents concluding remarks and acknowledges those who have aided in its completion in one way or another.

Chapter 2

Dynamics and Definitions

This chapter serves to define quantities used in this thesis and necessary for the analysis of atmospheric flow. We begin by considering different frames of reference before moving on to co-ordinate systems followed by a build-up to the primitive equations with some approximations and simplifications to them. Finally a most useful quantity for the study of atmospheric motion, namely potential vorticity, is introduced. The content presented in this chapter has been adapted mainly from *Andrews et al. (1987)* and *Lawrence (1997).*

2.1 Frames of Reference

Before making any measurements of a system such as the atmosphere one needs to consider what reference frame is to be used. When dealing with motions in the atmosphere there are two basic choices of reference frame.

The first is based on a stationary frame with relation to geographical features on the surface of the Earth and is called the Eulerian frame of reference. Here measurements are made at a number of grid points throughout the systems domain thus giving a 'snapshot' picture at one instant in time. For example temperature readings at towns and cities throughout the country.

The other choice is the Lagrangian frame of reference. This time we consider a set of parcels of air and move with them thus following the flow of the fluid or motions of the atmosphere. The analogy this time would be making some sort of measurements in a hot air balloon that is moving with the surrounding air.

Maps based on an Eulerian frame built up from many observations at different locations can provide an insight into fluid motion but for actual parcel trajectories, as required for parts of this project, a Lagrangian frame must be used.

2.2 Vertical Co-ordinate Systems

The most widely understood co-ordinate system would have to be geometric height where altitude is measured in metres or feet above the surface or mean sea level depending on what the situation requires. When dealing with dynamical aspects of the atmosphere however, this is not always the most convenient system or the simplest in terms of the governing equations.

Atmospheric pressure falls exponentially with height and can be defined as,

$$p = p_s e^{(-z/H)} \tag{2.1}$$

where p is pressure, p_s the standard reference pressure (usually taken as 1000mb), z the vertical co-ordinate and H a scale height defined as,

$$H = \frac{kT}{mg} \tag{2.2}$$

where k is Boltzmans' constant, T temperature in Kelvin (note $T(°C)=T(K)-273$), m the mean mass and g gravity. Note that H varies with height in the atmosphere primarily due to the large temperature changes. Stratospheric data for this project is based on a constant scale height of 6950m. Rearrangement of equation 2.1 yields the first of the alternative vertical co-ordinates and is called the 'log-pressure' co-ordinate defined as,

$$z = H \ln(p / p_s) \tag{2.3}$$

The second vertical co-ordinate to be defined here is potential temperature. Potential temperature θ is simply the temperature a parcel of air at pressure p and temperature T would have if it were expanded or compressed adiabatically (without heat transfer) to the reference pressure p_s and is defined as,

$$\theta = T(p_s / p)^{\kappa} \tag{2.4}$$

where $\kappa = R/c_p$; the gas constant for dry air divided by the specific heat at constant pressure. Potential temperature increases with height and is conserved for adiabatic motion. Thus we can define constant potential temperature surfaces, called isentropic surfaces, on which parcels will travel provided they move adiabatically in the flow.

Another measure of the vertical co-ordinate is geopotential height. Geopotential Φ at a given height z is defined as the work required to raise a unit mass to that height from mean sea level;

$$\Phi = \int_0^z g dz \tag{2.5}$$

Therefore the new vertical co-ordinate, geopotential height Z, can be defined as,

$$Z \equiv \frac{\Phi(z)}{g_0} \tag{2.6}$$

where g_0 is the global average of gravity at sea level.

2.3 The Primitive Equations

To describe the dynamics of the atmosphere we need to have a set of equations covering the forces that act on parcels of air, quantities that are conserved in the atmosphere and thermodynamic properties. The equations referred to are called the primitive equations and although a full derivation is not presented a brief background to them will be given.

2.3.1 Forces

The first force that should be considered arises from the fact that we are not in an inertial frame of reference, that is, we live on a rotating planet. Two forces owe their origin to the rotation of the Earth and give rise to the Coriolis acceleration and centripetal acceleration.

The Coriolis acceleration is present whenever something moves over the rotating planet and is defined as $2\underline{\Omega}\times\underline{u}$ where $\underline{\Omega}$ is the rotational angular velocity of the Earth and $\underline{u}$ the velocity vector with components (u,v,w) in the zonal (east-west), meridional (north-south) and vertical directions respectively.

The centripetal acceleration is directed perpendicularly away from the rotation axis and is defined as $\underline{\Omega}\times(\underline{\Omega}\times\underline{r})$ where $\underline{r}$ is the position vector.

Three other forces are important and are as follows. Gravity $\underline{g}$ directed downwards toward the centre of the Earth, a pressure force of the form $-\rho^{-1}\nabla p$ (where ρ represents density) and finally frictional (or viscosity) forces $\underline{F}$.

Combining all these together we get the equation of motion with respect to the rotating frame of reference,

$$\frac{D\underline{u}}{Dt}=-2\underline{\Omega}\times\underline{u}-\underline{\Omega}\times(\underline{\Omega}\times\underline{r})-\underline{g}-\frac{1}{\rho}\nabla p+\underline{F} \tag{2.7}$$

with all quantities and terms previously defined. It should be noted that forces due to electromagnetic fields have been omitted as they are important at greater heights in the atmosphere (in particular the ionosphere extending from 60km upwards) and are not relevant to this project which focuses on the stratosphere in which the atmosphere is neutral.

We are now in a position to state the first two primitive equations that express momentum balance in the zonal and meridional directions. Using spherical co-ordinates, i.e. latitude, λ, and longitude, ϕ, with log pressure height, z, as the vertical co-ordinate the equations are,

$$\frac{Du}{Dt}-\frac{uv}{a}\tan\phi-fv+\frac{1}{a\cos\phi}\frac{\partial\Phi}{\partial\lambda}=X \tag{2.8a}$$

$$\frac{Dv}{Dt}+\frac{u^2}{a}\tan\phi+fu+\frac{1}{a}\frac{\partial\phi}{\partial\lambda}=Y \tag{2.8b}$$

where a is the mean Earth radius, X and Y are the friction terms and f represents the Coriolis parameter (the vertical component of the Earth's rotation vector) defined as,

$$f\equiv 2\Omega\sin\phi \tag{2.9}$$

Note that since f depends on latitude it will be negative in the Southern Hemisphere and positive in the Northern Hemisphere.

2.3.2 Hydrostatic Balance

If the atmosphere is assumed to be in hydrostatic equilibrium then the pressure difference in the vertical in a volume of air will be that just sufficient to support the weight of the volume of air. Consider a volume with unit area cross section and height ∂z with pressure p at the top and $p+\partial p$ at the bottom. The difference in pressure will therefore be the weight force of the volume, i.e.,

$$\partial p = -\rho g \partial z \tag{2.10}$$

With a little manipulation and treating the atmosphere as an ideal gas (described by the state equation $p=\rho RT$), we arrive at the third primitive equation expressing hydrostatic balance in the vertical which, using temperature, can be written as,

$$\frac{\partial \Phi}{\partial z} = \frac{RT}{H} \tag{2.11}$$

or with potential temperature in which case takes the form,

$$\frac{\partial \Phi}{\partial z} = \frac{R\theta}{H} e^{(-\kappa z/H)} \tag{2.12}$$

2.3.3 Mass Continuity

When performing any sort of modelling of the atmosphere it is important that the total mass remains conserved as it is unphysical to have any sort of gain or loss. If we consider the mass of a volume element in a flow, the continuity equation states that the net flow of mass into a unit volume per unit time is equal to the local rate of change of density, or,

$$\nabla \cdot \rho \underline{u} = -\frac{\partial \rho}{\partial t} \tag{2.13}$$

where $\underline{u}=(u,v,w)$, the velocity vector as before. Expanding the dot product on the left and writing the density as a mean background value with some small perturbation as,

$$\rho(x,y,z,t) = \rho_0(z) + \rho'(x,y,z,t) \tag{2.14}$$

yields,

$$\frac{1}{\rho_0}\left(\frac{\partial \rho'}{\partial t} + \underline{u}\cdot\nabla\rho'\right) + \frac{w}{\rho_0}\frac{d\rho_0}{dz} + \nabla\cdot\underline{u} \approx 0 \tag{2.15}$$

It turns out that the first terms in the brackets involving the density perturbation can be neglected as they are smaller than the other terms by an order of magnitude, thus we can simplify the equation into vector notation as, $\nabla\cdot(\rho_0\underline{u})=0$, which when expanded in spherical co-ordinates, gives the fourth primitive equation for continuity of mass,

$$\frac{1}{a\cos\phi}\frac{\partial u}{\partial \lambda}+\frac{1}{a\cos\phi}\frac{\partial(v\cos\phi)}{\partial\phi}+\frac{1}{\rho_0}\frac{\partial(\rho_0)}{\partial z}=0 \tag{2.16}$$

2.3.4 Thermodynamics

Chapter one outlined the temperature variation with height for our atmosphere with a brief description of the principle causes for each region. The changing temperature has a sizeable effect on the state of the atmosphere and it is this that the last of the primitive equations is based on. The first law of thermodynamics states that 'the change in internal energy of a system is equal to the difference between the heat added to the system and the work done by the system'. This can be represented as,

$$c_v dT = dq - pd\alpha \tag{2.17}$$

where c_v is the specific heat at constant volume and $\alpha = 1/\rho$. The term on the left-hand side is the change in internal energy and the terms on the right are the change in heat and the work done by the system respectively. In the atmosphere heat transfer is normally slow compared to other processes, thus on shorter timescales we can treat the atmosphere as being adiabatic. Over longer timescales there is normally a net transfer of heat in which case the process is called diabatic. The most common heat flux in the atmosphere comes via radiative processes as briefly outlined in chapter 1, hence the thermodynamic equation may be written with total derivatives and J as the radiative heat flux as,

$$J = c_v\frac{DT}{Dt}+p\frac{D\alpha}{Dt} \tag{2.18}$$

Following which, elementary manipulation leads to,

$$Q=\frac{DT}{Dt}-\kappa T\frac{D\ln p}{Dt} \tag{2.19}$$

where $Q=J/c_p$. Evaluation of the second derivative on the right hand side shows that the term $w\partial \ln p/\partial z$ is much larger than the other terms, which can be neglected. Thus, we have arrived at the last of the primitive equations which expresses the material rate of change of temperature,

$$\frac{DT}{Dt}+\frac{\kappa wT}{H}=Q \tag{2.20}$$

or using potential temperature,

$$\frac{D\theta}{Dt}=Q \tag{2.21}$$

2.3.5 Summary: The Primitive Equations

The primitive equations as previously outlined using spherical and log-pressure co-ordinates are,

$$\frac{Du}{Dt} - \frac{uv}{a}\tan\phi - fv + \frac{1}{a\cos\phi}\frac{\partial\Phi}{\partial\lambda} = X \tag{2.22a}$$

$$\frac{Dv}{Dt} + \frac{u^2}{a}\tan\phi + fu + \frac{1}{a}\frac{\partial\phi}{\partial\lambda} = Y \tag{2.22b}$$

$$\frac{\partial\Phi}{\partial z} = \frac{R\theta}{H}e^{(-\kappa z/H)} \tag{2.22c}$$

$$\frac{1}{a\cos\phi}\frac{\partial u}{\partial\lambda} + \frac{1}{a\cos\phi}\frac{\partial(v\cos\phi)}{\partial\phi} + \frac{1}{\rho_0}\frac{\partial(\rho_0)}{\partial z} = 0 \tag{2.22d}$$

$$\frac{D\theta}{Dt} = Q \tag{2.22e}$$

The first two expressing momentum balance in the zonal and meridional directions respectively, the third hydrostatic balance, the fourth mass continuity and finally the rate of change of potential temperature. It should be noted that *D/Dt* is the material derivative and is,

$$\frac{D}{Dt} \equiv \frac{\partial}{\partial t} + \frac{u}{a\cos\phi}\frac{\partial}{\partial\lambda} + \frac{v}{a}\frac{\partial}{\partial\phi} + w\frac{\partial}{\partial z} \tag{2.23}$$

in the present co-ordinate system.

2.4 Geostrophic Approximation

The primitive equations are still relatively involved and cover many aspects of atmospheric flow. It is possible however to make some simplifications to them when dealing with motion in a particular region or on a certain scale. The easiest method to make a simplification to a complicated equation is to apply a scale analysis to the various terms whereby each is evaluated with a typical magnitude for each quantity thus allowing the relative size of the terms to be compared.

Applying a scale analysis to the momentum equations for synoptic scales (typically of ~1000km) shows that the curvature terms, time dependant derivative terms and the friction terms can be neglected. A further approximation can be made to capture the basic latitudinal variation of the Coriolis parameter, expressing it as,

$$f = f_0 + \beta y \tag{2.24}$$

where $f_0 = 2\Omega\sin\phi_0$ and $\beta = 2\Omega a^{-1}\cos\phi_0$ with ϕ_0 denoting some reference latitude about which the flow will be considered.

The result is that the Coriolis terms are balanced by the horizontal gradients of geopotential or alternatively,

$$fu = -\frac{1}{\rho}\frac{\partial p}{\partial y} \tag{2.25a}$$

$$fv = \frac{1}{\rho}\frac{\partial p}{\partial x} \tag{2.25b}$$

where $f=f_0$. Geostrophic balance holds for synoptic scale, low-frequency (slowly varying), extra-tropical flow away from the surface of the earth. These conditions can be formalised as in *Andrews et al. (1987)* in the following way,

$$Ro \equiv U / f_0 L << 1 \tag{2.26a}$$

$$\partial / \partial t << f_0 \tag{2.26b}$$

$$\beta L << f_0 \tag{2.26c}$$

$$|X|, |Y| << f_0 U \tag{2.26d}$$

where Ro is the Rossby number and U and L are typical orders of magnitude of the horizontal wind speeds and length scales respectively. Condition (a) states that the Rossby number measureing the ratio of the non-linear terms $\underline{u} \cdot \underline{\nabla}(u, v)$ to the Coriolis terms be small thus giving large scale motion, while (b) states that the ratio of the time derivatives to the Coriolis terms also be small ensuring steady or low-frequency flow. The next condition, (c), allows the use of just f_0 while finally (d) ensures that the friction terms are small.

2.5 Quasi-Geostrophic Flow

These equations can next be manipulated to allow study of the time development of the geostrophic flow, achieved by expanding the winds around geostrophic balance.

The basic method is to first define the departure, T_e, of the temperature profile from a reference temperature profile, $T_0(z)$, in the following way,

$$T_e \equiv T - T_0(z) \tag{2.27}$$

with an entirely similar result for potential temperature with θ in place of T. Next the winds are split into their geostrophic and ageostrophic components,

$$u = u_g + u_a \tag{2.28a}$$

$$v = v_g + v_a \tag{2.28b}$$

$$w = w_a \tag{2.28c}$$

where $|u_a| << |u_g|$ and $|v_a| << |v_g|$. These modifications give rise to the equations describing 'quasi-geostrophic flow' as outlined in *Andrews et al. (1987)*,

$$D_g u_g - f_0 v_a - \beta y v_g = X \tag{2.29a}$$

$$D_g v_g + f_0 u_a + \beta y u_g = Y \tag{2.29b}$$

$$\frac{\partial u_a}{\partial x} + \frac{\partial v_a}{\partial y} + \frac{1}{\rho_0}\frac{\partial(\rho_p w_s)}{\partial z} = 0 \tag{2.29c}$$

$$D_g \theta_e + w_a \frac{\partial \theta_0}{\partial z} = Q \tag{2.29d}$$

where the time derivative following the geostrophic wind is,

$$D_g \equiv \frac{\partial}{\partial t} + u_g \frac{\partial}{\partial x} + v_g \frac{\partial}{\partial y} \tag{2.30}$$

Note that $w_a \theta_z$ has been replaced by $w_a \theta_{0z}$ under the assumption that the departure θ_e from the reference temperature $\theta_0(z)$ is small i.e. $|\theta_{ez}| << \theta_{0z}$.

2.6 Eulerian-Mean Equations

The equations can then be simplified in terms of a zonal mean whereby quantities are averaged around latitude circles. An average such as this is most useful as the flow is predominately zonal anyway and allows multiple level global data to be displayed graphically with ease as in many parts of this thesis.

Mathematically the zonal mean is calculated in spherical co-ordinates as,

$$\bar{u}(\phi, z, t) = \frac{1}{2\pi}\int_0^{2\pi} u(\lambda, \phi, z, t) d\lambda \tag{2.31}$$

The departure from the zonal mean is then specified and following substitution into equations 2.22 yields the rather messy set of primitive equations for the Eulerian mean flow in spherical co-ordinates (see *Andrews et al. (1987)* for a full derivation). It turns out that due to periodicity $\bar{v}_g = 0$, therefore the zonal-mean geostrophic wind $(\bar{u}_g, \bar{v}_g, 0)$ is purely zonal. A transformation can then be applied by defining a residual mean meridional circulation giving the Transformed Eulerian-Mean (TEM) Equations to make dealing with specific eddy fluxes a little easier.

2.7 Vorticity

Vorticity is a measure of the rotation in a fluid and is defined as the curl of the velocity,

$$\underline{\omega} = \underline{\nabla} \times \underline{u} \tag{2.32}$$

Absolute vorticity (usually denoted with a subscript a) is calculated by using the absolute or 'true' velocity in an inertial frame of reference. Relative vorticity is calculated with the velocity relative to the local co-ordinate system, which may be a non-inertial rotating frame of reference for example. In dynamical meteorology we are generally only concerned with the vertical components of absolute and relative vorticity, hence without further mention it is these components that are referred to when dealing with vorticity.

The difference between the absolute or total vorticity, Γ, and the relative vorticity, ζ, is the planetary vorticity or more commonly known as the Coriolis parameter, f, thus giving,

$$\Gamma = \zeta + f \tag{2.33}$$

where the relative vorticity in Cartesian co-ordinates is,

$$\zeta = \frac{\partial v}{\partial x} - \frac{\partial u}{\partial y} \tag{2.34}$$

Applying the partial derivatives to the quasi-geostrophic equations 2.29b and 2.29a respectively yields the vorticity equation,

$$D_g \zeta_g = \frac{f_0}{\rho_0} \frac{\partial (\rho_0 w_a)}{\partial z} - \frac{\partial X}{\partial y} + \frac{\partial Y}{\partial x} \tag{2.35}$$

where the total quasi-geostrophic vorticity is,

$$\zeta_g \equiv f_0 + \beta y + \frac{\partial v_g}{\partial x} - \frac{\partial u_g}{\partial y} \tag{2.36}$$

2.8 Potential Vorticity

Ertel's potential vorticity is defined as,

$$P = \frac{1}{\rho} \underline{\omega}_a \cdot \underline{\nabla} \theta \tag{2.37}$$

which under the same approximations that gave rise to the primitive equations in section 2.3.5 is given by,

$$\rho_0 P \equiv \theta_z \left(f - \frac{(u \cos\phi)_\phi}{a \cos\phi} + \frac{v_\lambda}{a \cos\phi} \right) - \frac{\theta_\lambda v_z}{a \cos\phi} + \frac{\theta_\phi u_z}{a} \tag{2.38}$$

In isentropic co-ordinates the vertical velocity $D\theta / Dt$ is equal to the diabatic heating term Q, thus adiabatic flow will have no motion across isentropic surfaces (θ = constant). Therefore for frictionless adiabatic flow ($X,Y,Q = 0$), manipulation of equation 2.37 yields,

$$\frac{DP}{Dt} = constant \tag{2.39}$$

(See also *Clough et al. (1985), Hoskins et al. (1985)* and *Andrews et al. (1987)*). Thus isentropic potential vorticity (IPV) is conserved (following adiabatic frictionless motion) over timescales of a few days throughout the stratosphere. It is this property that provides us with a very useful atmospheric tracer (used later in this thesis to visualise stratospheric motion) derived solely from the dynamical properties of the flow eliminating the need to follow a trace gas for example when studying motions.

Beginning with equation 2.35, we can construct the quasi-geostrophic potential vorticity equation by eliminating w_a and using a little manipulation (see *Andrews et al. 1987*) to yield,

$$D_g q_g = -X_y + Y_x + f_0 \rho_0^{-1} (\rho_0 Q / \theta_{0z})_z \tag{2.40}$$

where the quasi-geostrophic potential vorticity q_g is,

$$q_g \equiv \zeta_g + f_0 \rho_0^{-1} (\rho_0 \theta_e / \theta_{0z})_z \tag{2.41}$$

Again for adiabatic frictionless motion $(X,Y,Q = 0)$ the quasi-geostrophic potential vorticity, q_g, is conserved following the horizontal geostrophic flow. Note that P is conserved following the total flow even when the quasi-geostrophic conditions (2.26) do not apply.

Chapter 3

The Model and the Data

This chapter presents a brief description of the assimilation model including the origin of the data used in this thesis. Some of the software used for data analysis and the techniques employed by the computer code are also described.

3.1 Data Assimilation System

The United Kingdom Meteorological Office (UKMO) uses a data assimilation system to provide analysis of a mixture of observations in the stratosphere and troposphere which is based on the analysis correction scheme at the UKMO used routinely for operational weather forecasting. The system is used to provide three dimensional near real time analysis of the atmosphere up to the lower mesosphere, a task that is rather computationally expensive requiring the power of a supercomputer. The following provides a brief outline of the system and numerical model (adapted from *Swinbank and O'Neill (1994)*).

Once observational data has been collected from the UKMO data banks and transferred to the computer system it undergoes a pre-processing stage for the purposes of quality control. Observations are checked statistically against forecast (or background) values for the same location as the observation to determine if the data is grossly in error. If the data is in large disagreement then it is discarded and not passed on to the assimilation stage. Another check carried out is the "buddy check" whereby if two independent sets of data are in agreement they are likely to be accepted even if they disagree with the forecast data. This check is not however applied to satellite data where neighbouring observations come from the same instruments hence can not treated as independent.

The assimilation stage follows involving integration of the numerical model forward in time in assimilation mode. The model uses a regular grid with a resolution of 2.5° latitude by 3.75° longitude. The vertical co-ordinate system is a series of constant pressure surfaces at high levels which become terrain following near the ground with 42 levels spaced by approximately 1.6km (10 levels per factor of 10 in pressure) with the top of the model at 0.28hPa (approximately 56km). The radiation scheme used in the model was originally designed for use in the troposphere thus was amended to provide smoother and more accurate longwave heating rates at high levels. One problem that arose in the stratosphere was the noise from the gravity-wave scheme also developed for tropospheric models. This was overcome by retaining the gravity-wave scheme in the troposphere and lower stratosphere but replacing it by Rayleigh friction at higher levels.

The model is integrated forward in time with a dynamical advection time step of 20min. Each advection step involves three adjustment steps whereby the model is nudged toward the observed data to ensure the model is a realistic representation of the atmosphere. This nudging must be performed gently as any sudden changes will induce unphysical forces that will push the assimilation away from the real state of the atmosphere. Each adjustment step involves using the pressure gradient, the main part of the Coriolis terms and the vertical advection of potential temperature to update the pressure, temperature and winds. The zonal

wind from several adjustment steps is averaged to provide the horizontal and vertical advection in the next advection step.

The model may also be run in forecast mode whereby no data is assimilated allowing the model to evolve freely with no nudging governed only by the model equations. These forecast fields are then used for the quality control check of the next observations as mentioned above. Fields are written out every six hours during assimilation mode for two main reasons, namely quality control for observational data and for validation of the assimilation process. This data is termed the observational processing dataset (or ODP) and comprises the observed value and its difference from both the analysis and background values for the purpose of statistical analysis at a later date.

3.2 Data Origins

3.2.1 Satellite Data

The main source of data used in the stratosphere for the UKMO data assimilation system are temperature soundings from the TIROS-N series of polar orbiting satellites operated by the National Oceanic Atmospheric Administration (NOAA). The satellites are in sun-synchronous circular orbits at an altitude of ~1000km with periods of approximately 100 minutes. Because the Earth is spinning under the satellite its consecutive orbits move westward by about 30° in longitude, and due to the period of the satellites orbit compared to that of the Earth, orbits on successive days also do not overlap but gradually fill in the gaps between individual tracks thus mapping out the entire atmosphere [*Andrews et al. (1987)*].

Temperatures are derived from layer mean temperature soundings originating from measurements of the radiance of various regions in the atmosphere. There are two ways of obtaining the data, namely nadir sounding which involves looking below the satellite and by limb sounding involving looking sideways through the limb of the atmosphere. Different depths in the atmosphere can be sampled by measuring the radiance at different wavelengths since radiance varies with the opacity of the atmosphere which depends on how much atmosphere you are looking through. Two sources of data are used – SATEM reports that have approximately 500km horizontal resolution and extend to 1hPa (approx. 48km) and high-resolution soundings with 120km resolution up to 0.4hPa (approx. 54km) [*Swinbank and O'Neill (1994)*].

While satellite data is the primary source it is not the only one however. Radiosonde soundings of both temperatures and winds are also available normally up to around 50hPa (approx. 20km) and occasionally up to 10hPa (approx. 32km). Other sources include aircraft winds and temperatures, satellite cloud track winds and surface observations of pressure.

Temperature data can then be processed to provide the other necessary quantities for the model. See *Randel (1987)* for a discussion and comparison of methods of obtaining horizontal wind fields from geopotential height data.

For the purpose of this study four main quantities output from the model (temperature (T), geopotential (G), zonal (MU) and meridional (MV) winds) are compared and statistically analysed to provide a performance assessment of the forecast fields. Data files available for analysis cover various periods in 1994/95 including October 1994 with analysis files for each

day for the four quantities along with a series of forecasts for selected days extending out to five and sometimes seven days (see Appendix A).

3.2.2 Aircraft Data

In 1994 an international collaboration of nine countries embarked on a comprehensive study of the stratosphere, in particular the lower Southern Hemisphere stratosphere. The study was a combination of two campaigns conducted together. The Airborne Southern Hemisphere Ozone Experiment (ASHOE) was designed to study ozone loss and how that is related to different atmospheric processes, and secondly, Measurements for Assessing the Effects of Stratospheric Aircraft (MAESA), for assessing the environmental effects of future high flying aircraft by measuring stratospheric photochemistry and transport. The main data collection method was via NASA's ER-2 high-altitude research aircraft (illustrated in figure 3.1), which throughout 1994 conducted 45 flights, including test and transit flights. The two main locations for which flights were conducted from were Barber's Point, Hawaii (5 flights) and Christchurch, New Zealand (26 flights) (see Appendix B) [documentation on the *NASA ASHOE/MAESA CD-ROM*].

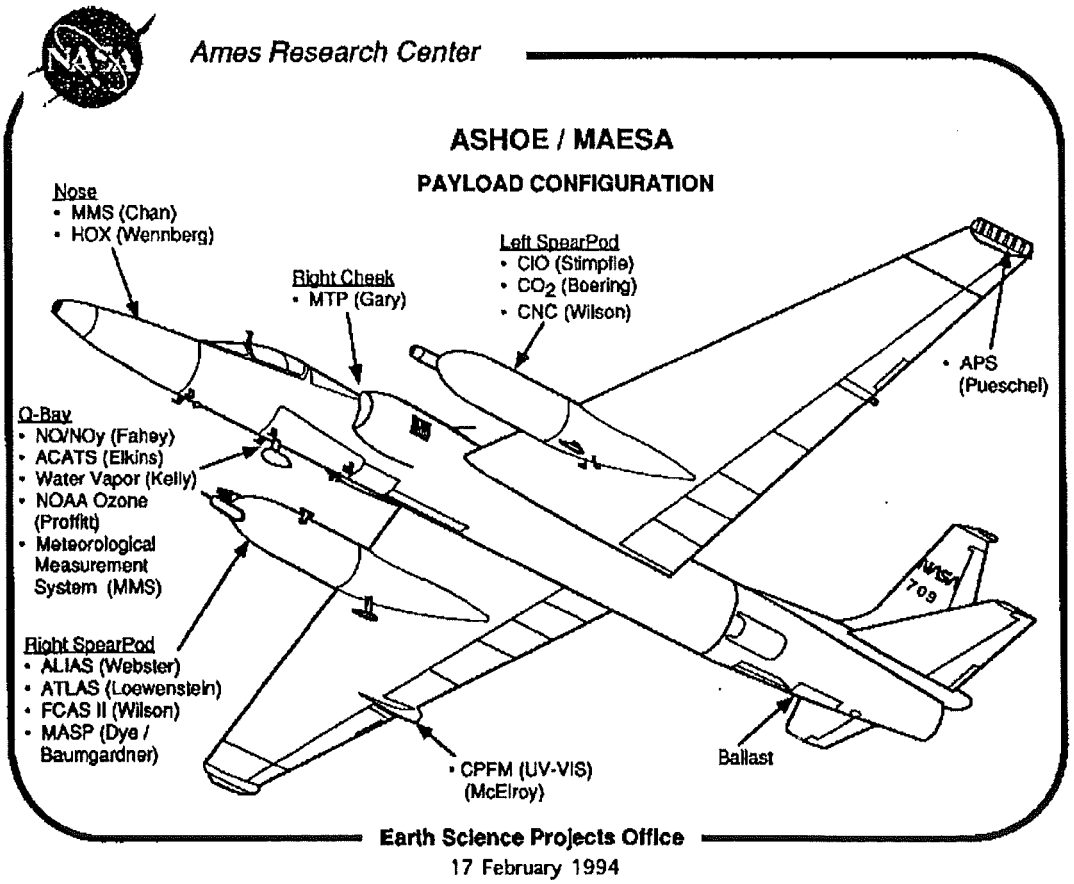

Fig 3.1. NASA's ER-2 with instrument locations and principle investigators. [from the project handbook on the *NASA ASHOE/MAESA CD-ROM*]

During ASHOE many of the flights conducted were of eight hour duration, enabling the ER-2 to fly as far south as ~68°S from Christchurch and as far North as ~19°S at an altitude of around 18-20km, in the lower stratosphere. A typical flight profile is depicted in figure 3.2 which presents time plots of latitude, longitude, height, and potential temperature. The data

used to generate the plots in figure 3.2 and later analysis in chapter five originates from the *NASA ASHOE/MAESA CD-ROM.*

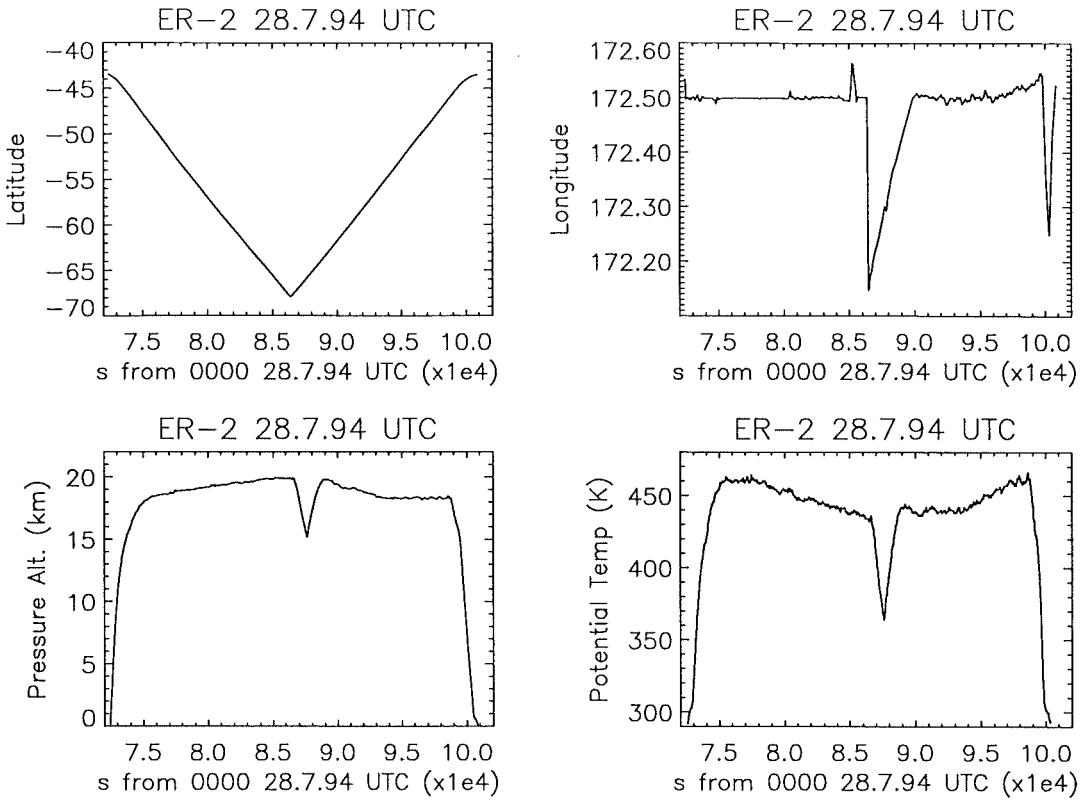

Fig 3.2. Time plots for the ER-2 flight on July 28 1994 of (a) latitude, (b) longitude, (c) pressure altitude and (d) potential temperature.

The payload for ASHOE consisted of more than a dozen different instruments measuring many different quantities in the stratosphere. The aircraft instruments provide the position information, latitude, longitude, height and time along with values of pitch, roll, airspeed etc. The ER-2 Meteorological Measurement System (MMS) also measures pressure (to an accuracy of ±0.3mb), temperature (±0.3K), horizontal wind ($\pm 1 ms^{-1}$) and vertical wind ($\pm 0.1 ms^{-1}$) [from the project handbook on the *NASA ASHOE/MAESA CD-ROM*]. Many other instruments were carried aboard the ER-2, (briefly described in Appendix B), for such things as chemical abundance and aerosol and CFC loading of the stratosphere. For the purpose of this study data originating from the Aircraft Laser Infrared Absorption Spectrometer (ALIAS) is used for comparison with high-resolution isentropic potential vorticity, to determine the position of filamentary structure from the vortex.

ALIAS is a high resolution scanning tunable diode laser spectrometer which measures nitrogen dioxide (NO_2), hydrogen chloride (HCl), methane (CH_4), and nitrous oxide (N_2O). The basic operation is to inject laser light in the 3.4 to 8 micron wavelength range into a one-metre 80-pass Herriott absorption cell fitted with a mechanical fringe-spoiler in a flowing configuration with a cell flush time of 1 to 2 seconds. The spectrometer is run by a 486-based computer with a 200Mb hard-disk. ALIAS has an accuracy of 5-10% depending on infrared spectral parameters and the signal to noise ratio with precision dependant on observed atmospheric concentrations and the signal to noise ratio. Detection limits for the species are, NO_2 and HCl; 0.05ppbv, CH_4; 0.2ppbv and N_2O; 0.1ppbv. The response time of the

instrument is 3 second data collection with 30 second full integration time for the sensitivities listed above [from the project handbook on the *NASA ASHOE/MAESA CD-ROM*]. A sample of typical data files is also given in Appendix B.

3.3 MADPO

The software package used for the analysis of data for this project is the Middle Atmosphere Dynamics Package at Oxford (MADPO). The package was designed for studying middle atmospheric data sets and accepts inputs in a number of formats including various aircraft and satellite data and of course the UKMO stratospheric analyses. The package is modular in design linking many programs and subroutines together making it very easy to add an option to a program or modify an existing one to suit the users needs.

As well as having a number of options for the graphical display of data including latitude-longitude plots or full colour polar stereographic plots for example, MADPO also allows the statistical analysis of data files to be carried out with ease. Various options are available including subset extraction either in the vertical or horizontal, simple field differences, root mean square differences, and horizontal mean standard deviation, all of which are used during the data analysis and manipulation later in this project.

An important point to note is the differences in 3D grids between the UKMO stratospheric analyses and the output from MADPO. For use in MADPO data is interpolated onto a 3° latitude by 3° longitude grid in the horizontal thus giving 120 longitude values including the Greenwich meridian and 60 latitude values starting at 88.5°S extending to 88.5°N so that the equator and poles are not included where computational complications can arise. The vertical resolution is 2km with 28 levels stretching from 2km to 56km thus covering both the troposphere and stratosphere. This interpolation from the UKMO's grid should not affect the subsequent analysis of the fields.

3.4 Back-Trajectory Mapping

When observing and analysing the atmosphere it is desirable to have both high spatial resolution and global coverage but in practice only one or the other is normally available. Aircraft measurements for example give high resolution but poor coverage while satellites give global coverage but low resolution. There exists however a means to obtain high resolution fields computationally from low resolution fields with good spatial coverage, namely back-trajectory mapping, also commonly referred to as reverse domain filling.

The basic method is to take a long-lived tracer such as potential vorticity and advect it forward in time with the wind field (obtained from the assimilation scheme) to generate a higher resolution field at some later time. The major problem with forward advection is that the parcels tend to disperse irregularly causing gaps in the field to develop. To demonstrate this phenomenon a global field of parcels was initialised on a 1° latitude × 1° longitude grid and then advected for five days using analysed winds from the assimilation scheme. Figure 3.3 is a plot of the final locations of the parcels clearly showing the gaps that have developed in the field. The advection was at a height of 20km and for the period 8-13 October 1994. This is overcome by computing the trajectories of a regular grid backward in time and then labelling the irregular locations with the appropriate value of potential vorticity at that initial

time. Next assuming the conservation of potential vorticity, the values are traced forward along the trajectories and mapped onto the regular grid thus giving the higher resolution field at the later time.

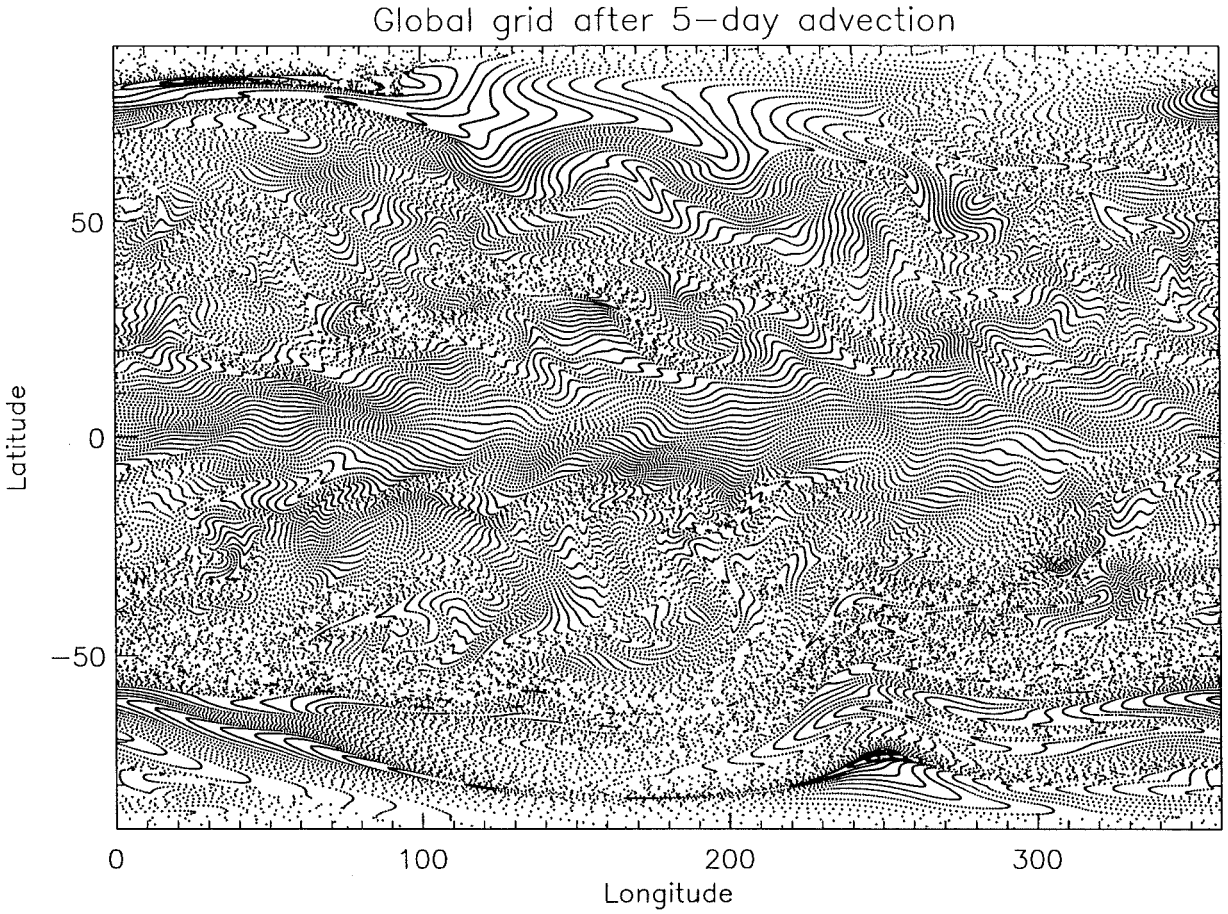

Fig 3.3. The final locations of a regular 1°×1° grid of parcels following five days of advection by analysed wind fields. Note the gaps in the field particularly near the north and south poles.

Practical application of the back-trajectory scheme is easiest when the motion is studied on an isentropic surface. In that case the flow is considered to be adiabatic since motion through the isentropic surface is negligible over short timescales thus ensuring the conservation of PV (see section 2.8). To obtain PV fields MADPO takes the model output temperature fields and first computes potential temperature (PT) fields thus allowing the location of isentropic surfaces to be known. Next zonal and meridional winds are interpolated onto these surfaces thus giving the isentropic zonal (IMU) and meridional (IMV) wind fields in PT co-ordinates which are then used to calculate isentropic potential vorticity (IPV).

Figures 3.4 and 3.5 give an example of a low-resolution isentropic potential vorticity field (3.4) and the high-resolution field (3.5) for the same time obtained from the back-trajectory scheme. Both are polar stereographic views for the IPV field on 20 October 1994 on the 500K isentropic surface (~20km). The high-resolution field was calculated using analysed wind fields.

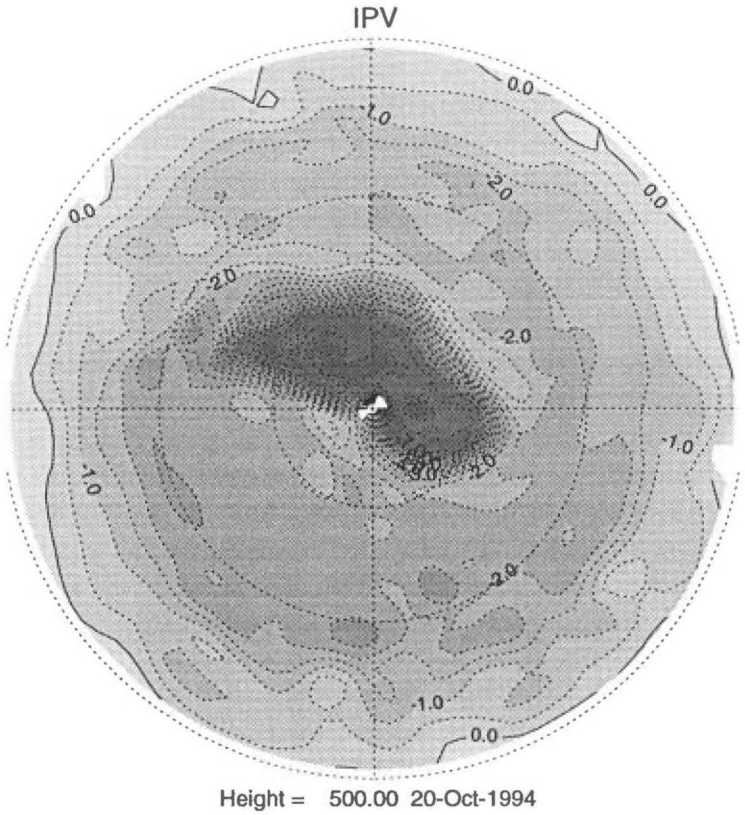

Fig 3.4. Low-resolution IPV field for 20 October 1994 at 500K (3°×3° grid).

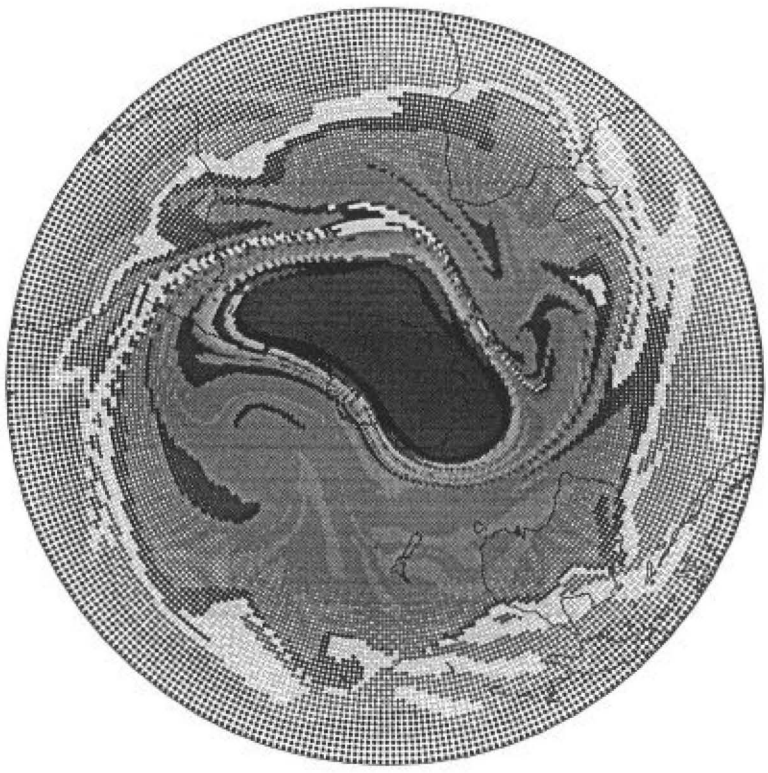

Fig 3.5. High-resolution IPV field for 20 October 1994 at 500K generated from the back-trajectory scheme (1°×1° grid). Note the fine structure near the vortex not present in fig 4.3 above.

Numerical implication of the trajectory scheme uses either the 12 or 24-hour wind fields from the assimilation scheme with a fourth order Runge-Kutta method to integrate the advection equations. The time step must be short enough to ensure that parcels do not travel more then one grid space per timestep, currently a two hour timestep is used. The co-ordinate system is polar stereographic near the poles to avoid inaccuracies and spherical co-ordinates away from the poles with velocities at parcel locations determined by bilinear interpolation from the surrounding grid points.

Later during analysis high-resolution maps are computed using a trajectory calculation time of five days primarily as no forecast files during October 1994 extended longer. Furthermore *Sutton et al. (1994)* argued that in a back trajectory scheme, five days would permit sufficient small-scale structure to develop without excessive error growth. *Sutton et al. (1994)* also studied the time reversibility of the trajectory calculations. Particles were advected backwards in time for five days and then forwards in time for five days. They found that 78% of all particles had a net displacement between initial and final locations of less than 100km and that 95% had net displacements less than 400km.

Chapter 4

Southern Hemisphere Stratosphere

An outline of the circulation of the atmosphere in particular the Southern Hemisphere stratosphere is presented in this chapter along with a more detailed description of the Antarctic polar vortex. A basic outline of the dynamics and chemical processes leading to ozone destruction is also given.

4.1 General Circulation

The axis of the Earth is not perpendicular to the plane of its orbit but is tilted by an angle of 23.5°. The major effect of this is of course the seasons in which the length of day varies more from summer to winter as you get further from the equator. At the time of the solstice the winter polar region remains in darkness for approximately three months with the summer polar region in daylight for an equal time. This gives rise to differential heating in the middle atmosphere which when coupled with atmospheric wave motions, drives a mean meridional circulation with rising motions over the summer pole, meridional drift at high levels and sinking motions over the winter pole. This diabatic circulation is depicted in figure 4.1.

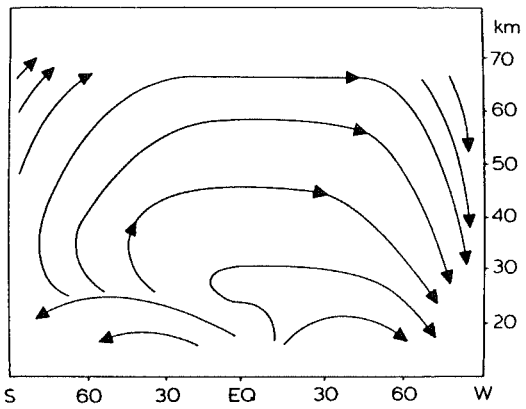

Fig 4.1. The diabatic circulation at solstice represented by the streamlines where the 'S' and 'W' indicate the summer and winter poles respectively. [from *Andrews et. al. (1987) after Dunkerton (1978)*]

The meridional motion experiences a Coriolis torque due to the rotation of the Earth, which causes zonal westerlies in the winter hemisphere and easterlies in the summer hemisphere which are in approximate thermal wind equilibrium with the temperature field [*Rosier (1996)*]. Figure 4.2 shows the mean zonal wind at solstice while figure 4.3 shows the mean zonal temperature at the same time with the summer and winter poles in each diagram indicated. While these figures present a reasonable representation of the general features found in the two hemispheres it should be noted that in reality there may be large differences in the circulation for both the North and South Hemispheres.

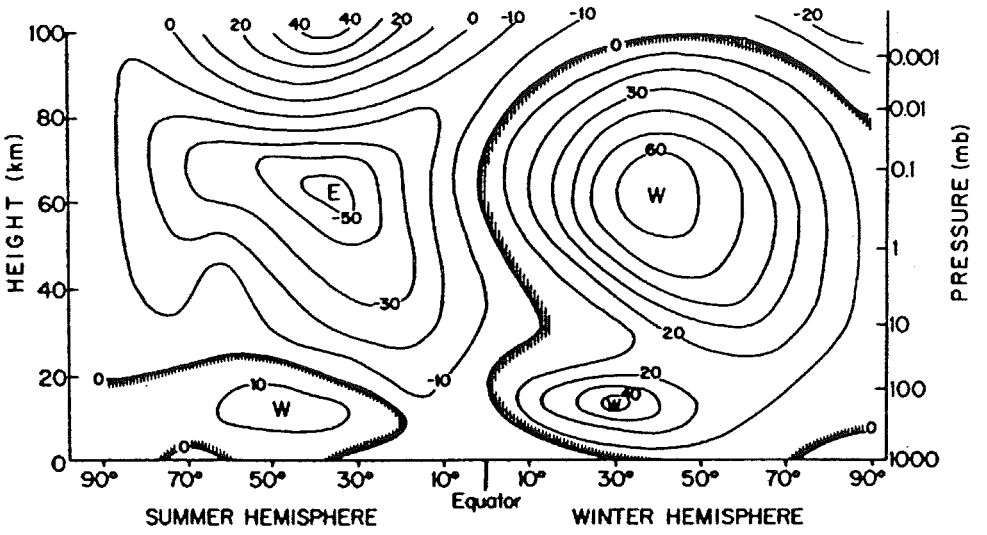

Fig 4.2. Latitude-height cross section of the atmosphere at solstice showing the zonal mean wind in m/s, with 'W' and 'E' representing westerly and easterly winds respectively. [after *Andrews et. al. (1987) courtesy of R. J. Reed*]

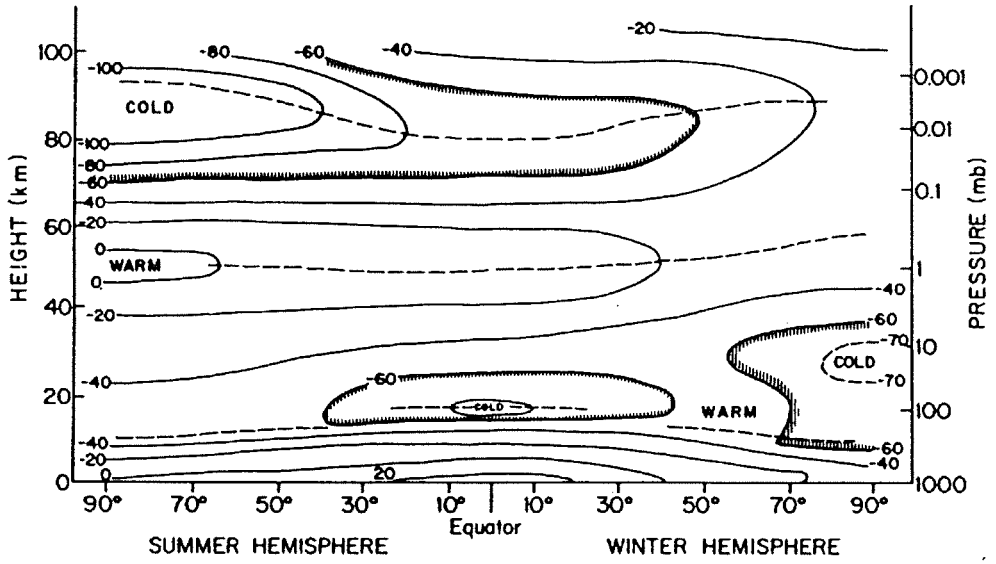

Fig 4.3. Latitude-height cross section of the atmosphere at solstice showing the zonal mean temperature in °C. The dashed lines indicate the tropopause, stratopause and mesopause. [after *Andrews et. al. (1987) courtesy of R. J. Reed*]

At the equinoxes the diabatic circulation is weaker with rising motions in the equatorial region due to planetary wave activity thus causing a meridional poleward drift in both the North and South Hemispheres (NH and SH). This time the Coriolis torque causes weaker zonal westerlies in both hemispheres.

4.2 Annual Evolution

The following presents an overview of the evolution of the zonal wind field for both hemispheres through 1994, the period covered by this study. The description is based on the

analysed model fields from the UKMO's assimilation system which were available for selected times during 1994 and early 1995 (see Appendix A).

A common feature for both hemispheres throughout the year was the presence of the tropical jets at the uppermost regions of the troposphere around 10-15km. The winds were always westerly with the winter jet being stronger in general than the summer jet and further equatorward in location. In the SH summer of 1994 for example the tropical jet was at ~50°S while later in winter it was at ~30°S.

The SH stratosphere was dominated by easterlies in the summer (around December) with the main feature being the tropical mesospheric jet peaking above the model lid at around 56km. At the same time the NH was dominated by a westerly flow with the maximum winds also occurring at mid-latitudes at the same height. Progressing through January and February, the easterlies in the SH strengthened a little with westerlies in the NH remaining strong. Through March and into April westerlies began to develop in the SH at high latitudes (near the pole) and began to strengthen with the first easterlies beginning to penetrate into the NH at the tropics as the westerlies weakened.

By June the situation was the complete reverse of December. Westerlies simply died away in the NH being replaced by easterlies while the SH was dominated by westerlies throughout the stratosphere. The line of maximum winds in the SH tilted equatorward with height from high latitudes at the tropopause with the region of strongest winds above the stratopause. As winter progressed in the SH, winds throughout both hemispheres strengthened. By August the line of maximum westerlies in the SH was nearly vertical at around 60°S defining the polar vortex with the core of the jet beginning to descend to the stratopause while remaining very strong at ~100m/s. Around September the first westerlies grew in the NH while the jet core in the SH continued to descend and move poleward.

In October the majority of the NH was in westerly flow with the maximum winds at mid-latitudes around the stratopause. In the SH the core weakened to around 60m/s and dropped to ~25km with the line of maximum winds now tilting poleward with height from mid-latitudes near the tropopause. Easterlies began to move further south into the SH from the tropics in November while westerlies continued to gain strength and dominate the whole of the NH. The descent and eventual disappearance of the core of the jet in the SH saw the return to the SH summer circulation.

4.3 The Polar Vortex

During the stratospheric winter large meridional temperature gradients exist due to the lack of sunlight in the polar region causing very cold temperatures there. As previously mentioned the winds are in thermal equilibrium with the temperature field hence the very strong polar night jet is further intensified by radiative cooling of the polar night air. Figure 4.4 is a zonal mean plot of the zonal wind for 1 August, 1994. The location of the polar night jet is clearly seen at ~60°S defining the polar vortex with winds around 100m/s at the core. In the case of the Antarctic vortex the lack of dynamical forcing from planetary waves gives rise to a very stable, and very cold vortex [*Salby and Garcia (1990)*]. While a vortex also forms in the Arctic, it is much more active and consequently less intense than the SH vortex. The main cause being the more frequent and larger planetary wave activity in the north due to the more dominant orographic features of the continents extending to much higher latitudes than in the SH. The strength of the vortex isolates the air inside from mid-latitudes thus inhibiting

transport and mixing with air from outside the vortex. Ozone destroying species will then build-up in the favourable vortex environment prevented from other reactions that would decrease their abundance. Thus we get a coupling mechanism between the dynamics and chemical destruction of ozone. The primary destruction of ozone by chemical means (see following section) results in less solar heating giving lower temperatures thus resulting in a colder more stable vortex.

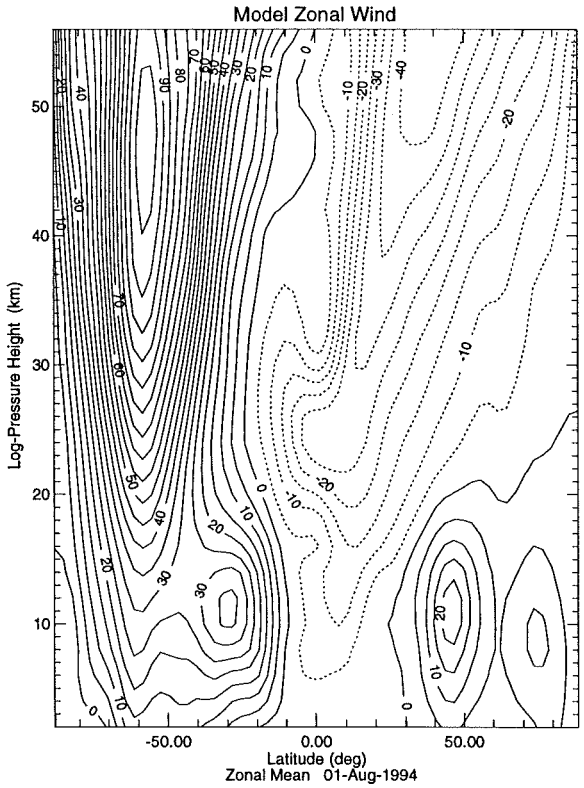

Fig 4.4. Latitude-height cross section of the zonal mean wind for Aug 1 1994. Note the strong polar jet at 60°S defining the edge of the polar vortex.

While large-scale transport is inhibited from the stable vortex, air is ejected in the form of filamentary structure from the edge of the vortex via Rossby wave breaking [*Waugh et al. (1994)*]. It is this process that leads to ozone-poor air reaching mid-latitudes. These filaments are mostly too small to alter the local wind field and are therefore 'passively advected' by the large-scale flow [*Schoeberl and Newman (1995)*]. For more rigorous discussions on the formation of filaments via Rossby wave breaking the reader is referred to *Waugh et al. (1994)*, *Polvani and Plumb (1992)* and *McIntyre and Palmer (1983, 1984 and 1985).*

4.4 Ozone and its Depletion

4.4.1 Natural Pathways

Ozone is both produced and destroyed naturally in the stratosphere. As mentioned in chapter one, ultra-violet (UV) radiation is absorbed by ozone thus heating the stratosphere. Not all UV radiation is absorbed however. Weak UV radiation with wavelengths of 320-400nm passes through the atmosphere and reaches the surface. Only the stronger UV radiation with

shorter wavelengths has sufficient energy to dissociate (or break up) certain gas molecules. Molecular oxygen (O_2), will undergo photodissociation by wavelengths in the range 40-240nm producing two atomic oxygen atoms,

$$O_2 + h\nu(40 - 240nm) \rightarrow O + O \tag{4.1}$$

where $h\nu$ is the energy of a photon of frequency ν, with h representing the Planck constant. The oxygen atoms can then undergo a three-body reaction to form ozone,

$$O_2 + O + M \rightarrow O_3 + M \tag{4.2}$$

where M is some other molecule such as molecular nitrogen (N_2), required to carry off the excess energy released in the bonding process. Thus we have the primary process by which ozone is produced in the atmosphere. A vertical profile for ozone is shown in figure 4.5 indicating the main position of the ozone layer in the stratosphere.

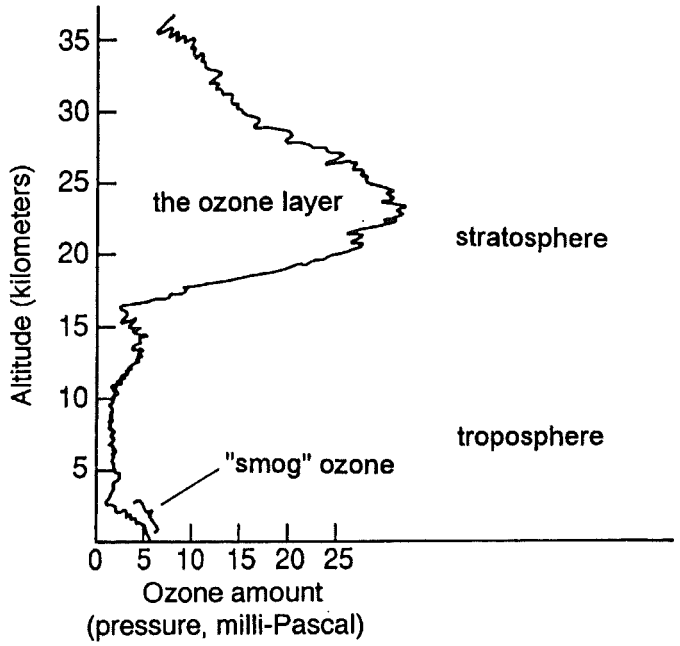

Fig 4.5. Vertical profile for ozone in the atmosphere. [from *Nilsson (1996) adapted from Scientific Assessment of Ozone Depletion: 1994*]

Ozone molecules are somewhat more weakly bound than a molecular oxygen molecule for example and can be photodissociated by UV radiation with wavelengths in the range 240-320nm,

$$O_3 + h\nu(240 - 320nm) \rightarrow O_2 + O \tag{4.3}$$

Therefore through the absorption processes by molecular oxygen and by ozone, most of the harmful UV radiation is removed before it can penetrate to the surface. However, as one might expect, any dramatic change in the ozone layer will consequently change the amount of UV radiation reaching the surface of the earth.

4.4.2 Human Acceleration

In 1985 the British Antarctic Survey Team at Halley Bay, Antarctica led by Joseph Farman announced there had been a severe depletion of ozone during the Antarctic spring [*Nilsson (1996)*]. Seven years earlier in 1978 the Nimbus-7 satellite was launched with the Total Ozone Mapping Spectrometer (TOMS) on board allowing the global seasonal variation of ozone to be studied with ease. The low values found by the survey team were not recorded by the satellite measurements as they were filtered out as anomalies. Farman had to ask for the original data to be studied before the Halley Bay measurements could be confirmed. The alarming discovery was the depletion in Antarctic ozone by as much as 50% compared with ground based measurements made in the 1960's. Data from the British Antarctic Survey Team for Halley Bay, Antarctica is presented in figure 4.6 showing the general decline of total ozone column over the years.

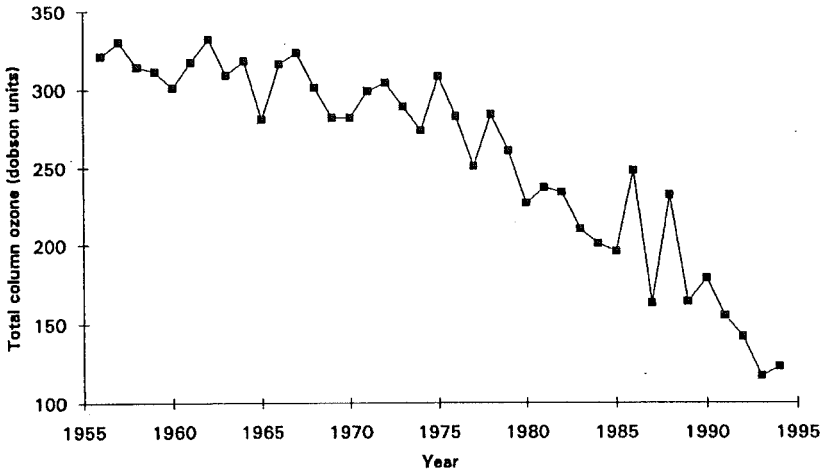

Fig 4.6. October mean total column ozone over Halley Bay, Antarctica. [from *Makhijani and Gurney (1995), data communicated by J.D. Shanklin in Dec 1994*]

The main cause for this depletion is now understood to be attributed to the chemical destruction of ozone intensified by the dynamical processes in the atmosphere, namely the presence of the polar vortex. As many of us are now aware, thanks to the media attention focused each year on the ozone hole, the origins of destructive compounds can be traced largely to aerosol propellants and refrigerants now being replaced by less harmful substances. The compounds to which we refer are chlorofluorocarbons or CFC's for short. Some examples of CFC's include CF_2Cl_2, $CFCl_3$, $CBrCl_3$, CH_3CCl_3 and many more. These gases are quite inactive so once released into the atmosphere can remain chemically inactive at lower levels until eventually they reach the stratosphere. Once at these heights they are exposed to strong UV radiation which breaks them up releasing chlorine (Cl) or bromine (Br), for example;

$$CFCl_3 + h\nu \rightarrow CFCl_2 + Cl \tag{4.4}$$

following which other reactions take place much faster such as;

$$\begin{aligned} CFCl_2 + O_2 &\rightarrow CFCl_2O_2 \\ CFCl_2O_2 + NO + O_2 &\rightarrow CFClO + NO_2 + ClO_2 \end{aligned} \tag{4.5}$$

thus releasing halogens as highly reactive atoms which then progress down destructive paths via catalytic cycles. Represented below is the general catalytic cycle resulting in the destruction of ozone as shown by the net result, taking an oxygen atom and an ozone molecule and producing two oxygen molecules. The *X* indicates a general species and can be replaced by chlorine, nitrogen (N), bromine, hydrogen (H) or a hydroxyl (OH) molecule for example.

$$\begin{aligned} X + O_3 &\rightarrow XO + O_2 \\ XO + O &\rightarrow X + O_2 \\ \hline O + O_3 &\rightarrow 2O_2 \end{aligned} \qquad (4.6)$$

Note that the cycle does not remove the destroying element but returns it to its original state thus leaving it ready to continue on its destructive path. The result is that one reactive chlorine atom can destroy about 1000 ozone molecules before transformation to an inactive form [*Makhijani and Gurney (1995)*]. There are however, several mechanisms reducing the number of harmful molecules present in the system. Firstly the catalytic equations do not simply stand alone but are coupled to many other reactions. Consider the following for just one example,

$$ClO + NO \rightarrow Cl + NO_2 \qquad (4.7)$$

which increases the activity of the chlorine monoxide (ClO) cycle, but also leads to,

$$ClO + NO_2 \rightarrow ClNO_3 \qquad (4.8)$$

giving a relatively stable product thus partially blocking the catalytic cycles involving ClO and nitrogen dioxide (NO_2).

Secondly, the catalytic cycles do have terminating points removing dangerous chlorine and other molecules from the system,

$$Cl + CH_4 \rightarrow HCl + CH_3 \qquad (4.9)$$

$$Cl + H_2O \rightarrow HCl + OH \qquad (4.10)$$

$$NO_2 + OH \rightarrow HNO_3 \qquad (4.11)$$

Equations 4.9 and 4.10 both remove a chlorine atom producing hydrogen chloride (HCl), which is relatively stable, as is nitric acid (HNO_3) resulting in the removal of NO_2 (equation 4.11). Chlorine is later permanently removed from the stratosphere when the HCl molecules diffuse across the tropopause and are eventually rained out, however the transport is slow and takes some 2-5 years [*Makhijani and Gurney (1995)*].

4.5 The Ozone Hole

The processes leading to the destruction of ozone in the previous section are normally described as 'homogeneous' since all the reacting compounds are in the gas-phase. We now turn our attention to 'heterogeneous' reactions which involve compounds in various phases such as gas and ice or gas and liquid.

The depletion of ozone due to the release of CFC's and other gases into the stratosphere is insignificant to the massive depletion causing the ozone hole over the south pole where a temporary loss of ozone of up to ~70% within a few weeks occurs. This takes place during the local spring and is a result of both dynamical and chemical contributions. During the winter, as previously mentioned, a stable vortex forms isolating a very cold and dry region from lower latitudes. Temperatures plunge to around 80-90°C below zero enabling polar stratospheric clouds (PSC's) to form. There are two main types of PSC's that form in this cold environment in the lower stratosphere [*Pitari et al. (1992)*]: Type I PSC's form when nitric acid trihydrate (NAT) particles ($HNO_3 \cdot 3H_2O$) condense onto sulphate aerosol particles below 198K (-75°C) resulting in a final particle size of ~1μm. Type II PSC's are much larger (10's of μm) and form when ice accumulates on NAT particles below 192K (-81°C). Special surface reactions then take place on PSC's which break up stable 'reservoir' gases into more active molecules denitrifying the lower stratosphere. Some examples of the reactions with the solid phase H_2O or HCl are;

$$\begin{aligned} HCl + ClNO_3 &\rightarrow HNO_3 + Cl_2 \\ ClNO_3 + H_2O &\rightarrow HOCl + HNO_3 \\ N_2O_5 + H_2O &\rightarrow 2HNO_3 \end{aligned} \qquad (4.12)$$

In early September when sunlight returns to the polar region chlorine molecules are broken up releasing active chlorine atoms which then begin the destruction,

$$\begin{aligned} Cl_2 + h\nu &\rightarrow 2Cl \\ Cl + O_3 &\rightarrow ClO \end{aligned} \qquad (4.13)$$

Other pathways include, with chlorine,

$$\begin{aligned} ClO + ClO &\rightarrow Cl_2O_2 \\ Cl_2O_2 + h\nu &\rightarrow Cl + ClO_2 \\ ClO_2 + N_2 &\rightarrow Cl + O_2 + N_2 \end{aligned} \qquad (4.14)$$

and with bromine,

$$\begin{aligned} Cl + O_3 &\rightarrow ClO + O_2 \\ Br + O_3 &\rightarrow BrO + O_2 \\ ClO + BrO &\rightarrow Br + Cl + O_2 \end{aligned} \qquad (4.15)$$

It is these reactions that are responsible for the rapid depletion and are able to proceed since the 'reservoir' gases have been removed due to denitrification. Figure 4.7 shows the strong anti-correlation of ClO to ozone with respect to latitude through the edge of the vortex. The sharp jump in ClO and hence drop in ozone as you penetrate into the vortex highlights just how stable and isolated the air is inside the vortex. Note that the ClO mixing ratio increases some 500% in the space of roughly 1° or ~110km.

As mentioned in section 4.3, the Antarctic vortex is more stable than its northern counterpart due to weaker planetary wave activity in the SH. In the case of the NH vortex, stronger planetary waves keep the Arctic vortex warmer thus preventing PSC's from readily forming [*Salby and Garcia (1990)*]. The implication of these inter-hemisphere differences is more severe ozone depletion over the Antarctic compared to that over the Arctic.

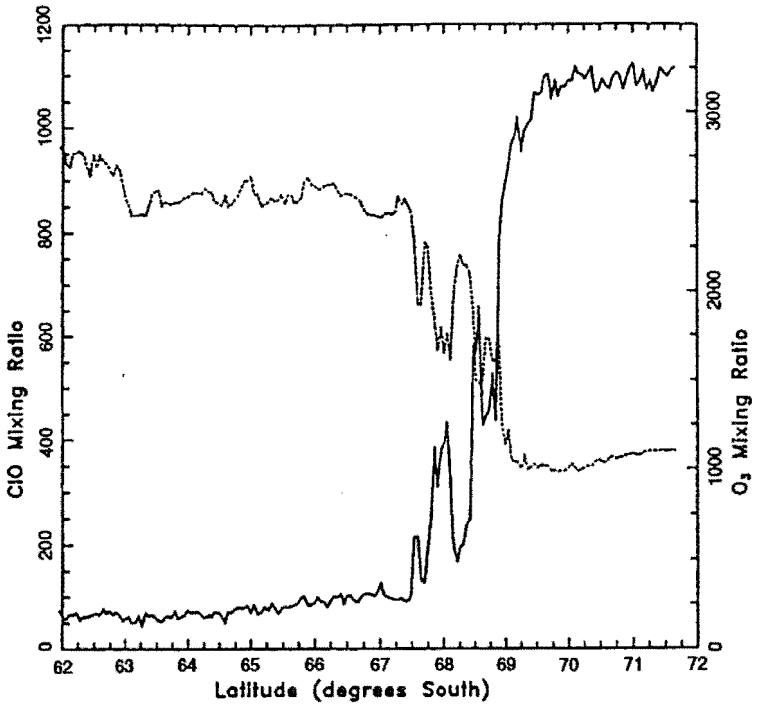

Fig 4.7. Anticorrelation of ClO (solid line, parts per thousand) and ozone (dotted line, parts per billion) over the Antarctic on 16 September 1987. [from *Makhijani and Gurney (1995), after Anderson et. al. (1989)*]

As the temperature rises through October the PSC's evaporate releasing the nitrogen compounds and water vapour for example,

$$HNO_3 + h\nu \rightarrow OH + NO_2 \tag{4.16}$$

which allows the active chlorine atoms and molecules to be re-captured,

$$\begin{aligned} Cl + H_2O &\rightarrow HCl + OH \\ ClO + NO_2 &\rightarrow ClNO_3 \end{aligned} \tag{4.17}$$

As November progresses the vortex begins to break up allowing the hole to fill from lower latitudes via horizontal transport of ozone rich air.

4.6 Other Depletion Mechanisms

Although the main processes leading to ozone loss have been outlined, three more should be noted that also contribute to a decline in ozone levels in the stratosphere. All three involve direct injection of harmful compounds into the stratosphere.

The first is volcanic eruptions. Most eruptions are not violent enough for emissions to overcome gravity and make it into the stratosphere, however over the past two decades, four have been sufficiently strong. They are; Mount St. Helens, United States of America, which erupted on 18 May 1980 sending emissions to a height of 19km, El Chichon, Mexico, 1982, Mount Pinatubo, Philippines, June 1991 after lying dormant for 600 years and Mount Hudson,

Chile, August 1991 [*Makhijani and Gurney (1995)*]. Following eruptions such as these, increased sulphate aerosol loading in the stratosphere was observed permitting heterogeneous ozone-destroying reactions to take place on the surface of sulphuric acid particles. Chlorine can also be injected directly into the stratosphere from an eruption in the form of HCl as in the case of El Chichon following which HCl levels rose significantly. (See *Hofmann and Solomon (1989)* for a discussion of ozone destruction following the eruption of El Chichon.)

The second source of emissions leading to a reduction in ozone levels is due to aircraft. Much research has gone into assessing the effects of present subsonic aircraft operating high in the troposphere and low stratosphere and of proposed fleets of supersonic aircraft flying in the stratosphere near 20km. Currently "subsonic aircraft flying in the North Atlantic flight corridor emit 56% of their exhaust emissions into the upper troposphere and 44% into the lower stratosphere on an annual basis." [*WMO (1994)*]. While there is uncertainty in supersonic assessments, models have shown "additional annually averaged ozone column decreases of 0.3-1.8% for the Northern Hemisphere." [*WMO (1994)*].

The third and final process outlined here is also due to direct emissions to the stratosphere but this time from solid fuel rockets. The largest rockets are the American Space Shuttle and Titan IV and the European Ariane 5 which all release nitrogen, hydrogen compounds and chlorine (mainly HCl) into the stratosphere which then contribute to the catalytic destruction of ozone. The main conclusions of studies into rocket launches have found that depletion in the local area of the exhaust wake (within a few kilometres) to be nearly total at heights of 30-40km. Due to rapid mixing however this effect will dissipate out relatively quickly. Local ozone decreases were calculated to be only 0.2% with changes in ozone column to be less than 0.1% [*WMO (1994)*].

Chapter 5

Results and Discussion

This chapter begins by outlining the period covered by the study and the main reasons for that particular choice before moving on to present the results. Firstly various errors between the analysed and forecast fields are outlined before moving on to a more in-depth look at RMS errors found in different regions in the stratosphere. The chapter moves on to model/aircraft temperature comparisons and then presents analysis of a Lagrangian approach to atmospheric motion. Finally small-scale structure from the back trajectory mapping technique is compared with measurements from the aircraft during ASHOE.

5.1 Period Studied

The primary focus of the study was on a period in October 1994 with both analysis and forecast datasets for comparison. This time of the year was chosen primarily because of the availability of aircraft data originating from the Airborne Southern Hemisphere Ozone Expedition (ASHOE) thus making model/aircraft comparisons possible. Furthermore, at this time of the year the vortex is well established and is beginning to decrease in strength before the final break-up in spring and as a result filamentary activity should be observed.

Six five day forecasts were available in October for comparison with assimilated data with the first day of the forecast being on the 9th, 11th, 13th, 16th, 17th and 19th October 1994. Assimilated data was available for the period 8-31 October 1994. Further data was also available at other selected times in the year including differing periods in Jan, Feb, May-Aug and Dec of 1994 and Jan-Apr of 1995 (see appendix A).

It should be noted that throughout the course of this study any differences have been calculated as analysis minus forecast.

5.2 Temperature and Wind comparisons

5.2.1 Minimum Temperature

When modelling chemistry in the Antarctic vortex region, one of the most important parameters to forecast accurately is the temperature. Polar Stratospheric Clouds only form in temperatures below about -80°C (or below ~190K) and are primarily responsible for the large-scale destruction leading to the ozone hole as outlined in chapter four. It is therefore important to forecast temperature in the vortex accurately so as to get the chemistry correct.

To obtain some measure of how well the model does, minimum temperatures from the forecast files were compared with those from the analysis files in the region 45°S to the South Pole. This region was chosen as it will contain the coldest temperatures during October inside the vortex as demonstrated in figure 5.1. The plot shows an analysed temperature field for 9 October 1994 with the coldest part of the vortex on that occasion at the South Pole at around

18km. Furthermore this choice forces the analysis to ignore the very cold region in the tropical lower stratosphere (see figure 5.1) where temperatures can be even colder than those found in the vortex.

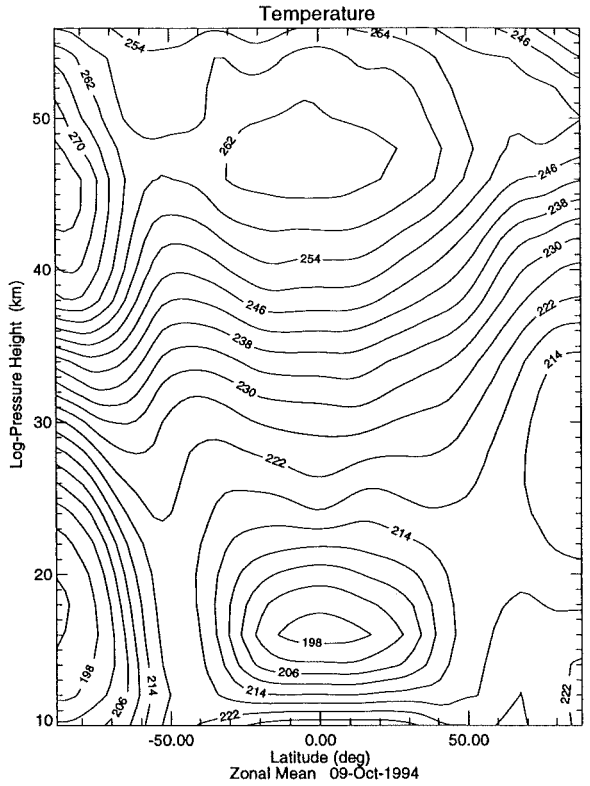

Fig. 5.1. Zonal mean plot of temperature for 9 October 1994. Note the coldest region of the vortex at around 18km with temperatures less than 194K.

Comparisons were made for the six five-day forecasts available in October 1994 with results revealing that the largest difference was no more than 3K (for all forecast periods) with the root mean squared error (RMSE) for minimum temperature at five days equalling 1.66K with a standard deviation of 0.85K. Note that the standard deviation was calculated from the spread of the six data points for each forecast period. Results of the comparisons are shown in figure 5.2.

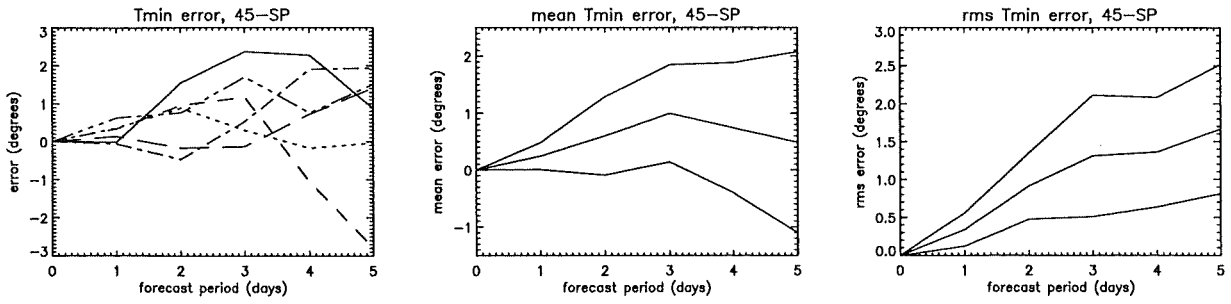

Fig 5.2 (a), (b) and (c). Results of the minimum temperature comparisons over the region 45°S-South Pole. Differences for individual files are shown in (a), the average of those differences ± one standard deviation are in (b), while (c) gives the RMS differences with the same error bounds.

Of the six five-day comparisons able to be made with the data, 22 occasions had the forecast minimum temperature too cold. This is further highlighted by the bias indicated in figure 5.2(b). Note that the mean minimum temperature error is positive through all forecast periods showing that in general the forecasts have the minimum temperature too cold (since the differences are calculated as analysis minus forecast). *Waugh et al. (1997)* found that the Australian Bureau of Meteorology's (ABOM) Global Assimilation and Prediction Scheme (GASP) forecast the minimum temperatures at 50hPa (~20km) too warm and that differences increased with forecast time with a monthly mean for October 1994 of ~4±2.5K after five days.

These results were based on a small number of comparisons, thus conclusive evidence can only be obtained through further study. However it is worth noting that the major effect of a systematic bias in minimum temperatures will be on the formation of PSC's in the cold Antarctic vortex in model simulations. Given a cold bias for polar temperatures, chemical models based on temperature fields would allow more PSC's to form in the colder modelled vortex following which an increased rate in the heterogeneous surface reactions would result (see chapter four). The net effect would be to overestimate the amount of chemical processing and hence ozone depletion compared to observations of the real atmosphere.

5.2.2 Maximum Wind

A second comparison of an extreme value was that of the maximum zonal wind in the Antarctic vortex region. The maximum wind will provide a measure of how well the forecasts predict the strength of the polar jet and hence the strength of the vortex. The strength of the polar jet at the edge of the vortex has implications on mixing across the vortex boundary coinciding with a region of steep PV gradients. *Manney et al. (1994)* show that increased mixing is consistent with weaker PV gradients and a weaker polar night jet (see also *Pierce et al. (1994)* and *Schoeberl et al. (1992)*). To accurately predict the mixing of polar air with mid-latitudinal air it is therefore important to forecast the strength of the polar jet correctly.

As winter progresses the region of maximum winds descends as outlined in chapter four and by October lies at approximately 30km at around 60°S (see figure 5.3). Differences were again calculated over the region 45°S to the South Pole, thus encompassing the entire vortex and strong polar jet. Thirty comparisons were made in October 1994, with 17 occasions having the forecast maximum zonal wind stronger than the analysed wind, with the largest differences measured at five days of ~6.5m/s. Results are presented in figure 5.4 which shows the individual cases, mean differences and RMS differences. As for the minimum temperature comparisons, the standard deviation error bounds were calculated from the spread of the six data points for each forecast period.

The findings suggest a relatively small systematic over-prediction of the maximum wind strength in the polar jet indicated by the bias in figure 5.4(b) which was no greater than 2m/s even out to five days. These results have the potential to lead to stronger PV contours at the vortex edge and hence an under-estimation of the mixing across the boundary in chemical models of the polar region. Note however that again a relatively small number of comparisons were made leading to a large variation in the averaged values shown by the size of the error bounds.

A possible cause for the over-prediction of the strength of the polar jet is given by *Carver et al. (1994)* in their study of the UK Universities Global Atmospheric Modelling Programme

(UGAMP) Global Circulation Model (GCM) (or UGCM) in forecasting the stratospheric vortex in the NH in 1992. They investigated the effects of the gravity wave drag (GWD) parameterisation scheme on the lower stratosphere. As expected the results showed that the forecast with no GWD produced a stronger stratospheric jet than the forecast with the GWD scheme. Recall from chapter three that in the UKMO model Rayleigh friction replaces the gravity-wave scheme at higher levels.

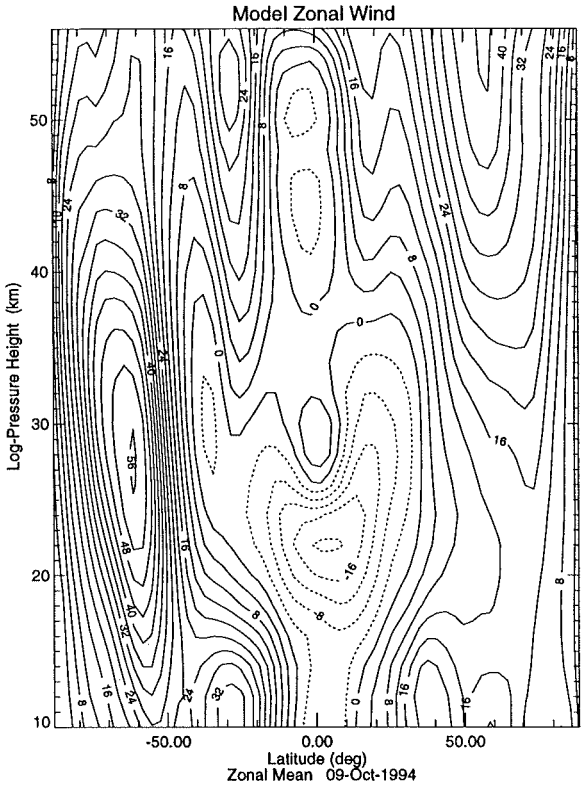

Fig 5.3. Zonal mean plot of zonal wind for 9 October 1994. Note the strongest part of the vortex at approx. 60°S and 30km.

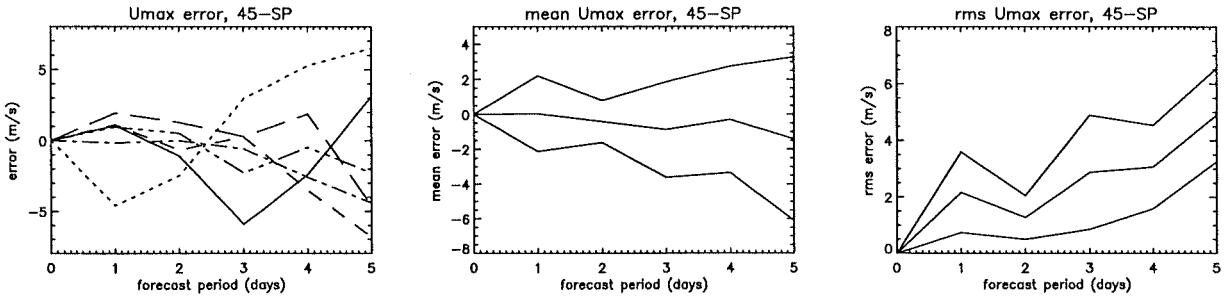

Fig 5.4 (a), (b) and (c). Results of the maximum zonal wind comparisons over the region 45°S-South Pole. Differences for individual files are shown in (a), the average of those differences ± one standard deviation are in (b), while (c) gives the RMS differences with the same error bounds.

Waugh et al. (1997) also conducted comparisons such as these and found maximum zonal winds were under-predicted by the Australian model at 50hPa (~20km) with a monthly-mean difference at five days of ~7.5±4.5 m/s.

A useful verification to the above observations would be the application of the Elliptical Diagnostic approach made by *Waugh et al. (1997)*, in which the vortex is examined in a "vortex-oriented view". One measure that was used for vortex strength in their study was the area of PV contours, or alternatively, the equivalent latitude (the latitude that encompasses the same area as the PV contour, i.e. a higher latitude corresponds to a smaller area and hence a weaker vortex). They found that the forecast vortex (from the ABOM's GASP) was weaker than the analysed vortex on the 500K isentropic surface (~20km), consistent with biases found towards under-predicting the maximum wind strength, and forecasting the minimum temperature too warm. Given the results of *Waugh et al. (1997)* and those in this study (for minimum temperature and maximum winds) one might expect an elliptical approach to indicate a stronger forecast vortex from the UKMO assimilation system than the analysed one.

5.3 Vortex Orientation

Further Elliptical Diagnostics were calculated by *Waugh et al. (1997)* and are most useful in analysing the vortex. The basic method involves fitting an ellipse to a chosen contour of IPV in the vortex (see *Waugh (1996)* for a concise discussion on the calculation of elliptical diagnostics). Comparisons of the properties of two ellipses, in this case a forecast and analysis ellipse, can then be made with ease. Basic diagnostics include the location (of the centre of the ellipse), elongation (or the aspect ratio, calculated as the semi-major axis divided by the semi-minor axis) and orientation of the ellipse (the angle of the semi-major axis to some reference direction).

While an elliptical approach was not employed in this study, a measure of the difference in orientation of the forecast to the analysis vortex can be achieved by examining where the features at the edge of the vortex are positioned. A crude but simple method to use is to compute field differences and examine one height, looking for a large dipole in the difference field at one latitude associated with a feature of the vortex such as a 'dip' or a 'lump' in the contours at the edge of the vortex. Figure 5.5 gives an example based on IPV contours at 500K (~20km). The analysed IPV field is shown in (a) with the edge of the vortex easily seen by the steep gradients in the plot at ~60°S, while (b) shows the difference between the analysis and forecast fields for that occasion.

In this case the 'dip' in the contours of IPV in figure 5.5(a) at ~160°E has been forecast too far eastward thus giving rise to the large +/- dipole in the difference plot in 5.5(b) at ~75°S.

This more eastward orientation of the forecast vortex was common in comparisons made throughout October 1994 and produced the same result as the elliptical approach by *Waugh et al. (1997)*. For example, they found that a five-day forecast of 9 October 1994 had the forecast ellipse orientated around 15° further east than the analysed ellipse. The largest difference found was for a seven-day forecast of 28 October 1994 when the forecast ellipse was orientated approximately 60° to the east of the analysed ellipse.

While PV is the best indicator of vortex position, other quantities associated with the vortex such as geopotential and temperature also showed the same dipole in latitude-longitude plots at the same height for the same occasion.

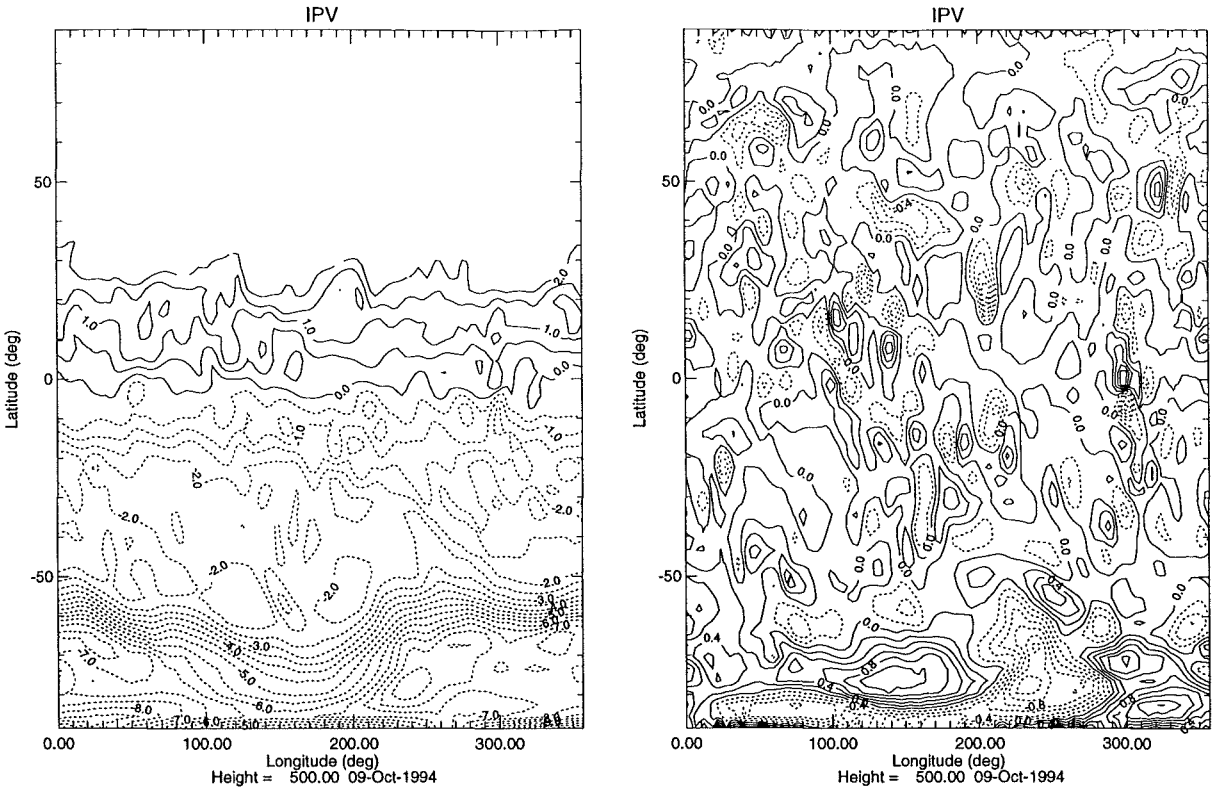

Fig 5.5(a) and (b). Latitude-longitude plots at 500K for 9 October 1994 showing (a) the analysed IPV field and (b) the difference between the analysed field and a one-day forecast.

5.4 Systematic Temperature Errors

Simple difference plots of the temperature fields reveal the largest errors are in the upper stratosphere near to the poles in the North and South Hemispheres. Figure 5.6(a) shows one such difference between the analysed temperature field for 9 October 1994 and a one-day forecast of the same day. The contour interval for this plot is 0.5K.

As can be seen from the plot, there are three main places where errors are occurring. They are, the large positive region of errors in the lower mesosphere close to the North Pole indicating the forecast is too cool there, and the +/- regions near the stratopause in the Southern Hemisphere near the South Pole. The large dipole in the errors near the South Pole suggests that the position of the stratopause (see figure 5.1) has been forecast incorrectly – too high in this case implying that the model forecast fields have the diabatic circulation incorrect with not enough descent in the Antarctic polar region at those heights. This observation is consistent with that of *Manney et al. (1995)* in their study of Lagrangian Transport Calculations using UARS Data. They conclude that "diabatic descent rates are too weak almost everywhere in the SH" due to a "possible bias in the SH UKMO temperatures".

These errors were roughly the same through October 1994 in both size and position and increased in magnitude as the forecast period increased thus were concluded to be systematic errors in the model forecast fields. For a 5-day forecast of 13 October 1994 for example, the maximum errors were approximately 15K at 50km in the Northern Hemisphere near the pole and -6K at 50km and 9K at 38km in the Southern Hemisphere near the pole.

These three large error regions were not unique to just the Southern Hemisphere winter. Approximately six months later, on 31 March 1995, the same was observed for the Northern Hemisphere winter as illustrated in figure 5.6(b). Again there is a large positive error region at present 50km near the South Pole and the same +/- dipole in the Northern Hemisphere at 40 and 50km respectively, near the North Pole. The contour interval is the same as for (a) at 0.5K.

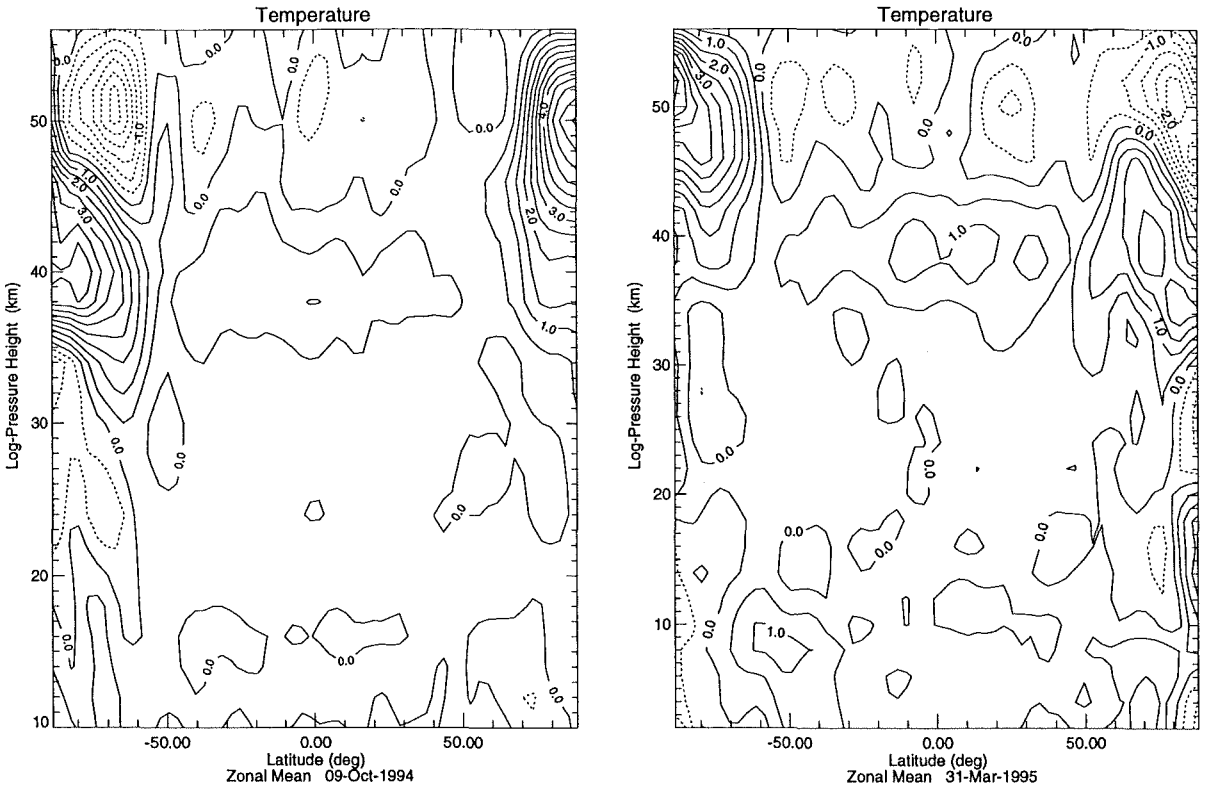

Fig 5.6(a) and (b). Zonal mean difference plots for one-day forecasts of temperature on (a) 9 October 1994 and (b) 31 March 1995. Note the similar structure in the systematic errors during the winters and summers of the North and South Hemispheres.

5.5 Zonal Wind Errors

Errors in the zonal wind field tended to be small from low to mid-latitudes throughout the stratosphere but were larger from mid-latitudes to the pole especially in the winter Hemisphere. These errors are directly associated with the vortex, in most cases presumably due to an incorrect position of the polar jet (see figure 5.3) thus leading to a large dipole error in the difference field in much the same way as the incorrect stratopause position leads to, in the temperature differences. Figure 5.7 shows two cases for October 1994. In each case the contour interval is 1m/s.

Wind strength was often over-predicted inside the vortex in both hemispheres for their respective winters as in figure 5.7(a), however this was not always the case as 5.7(b) shows where the strength of the polar jet has been under-predicted on this occasion. A further significant feature in both plots is the consistent over-prediction of the mesospheric jet in the Northern Hemisphere lower mesosphere near the pole.

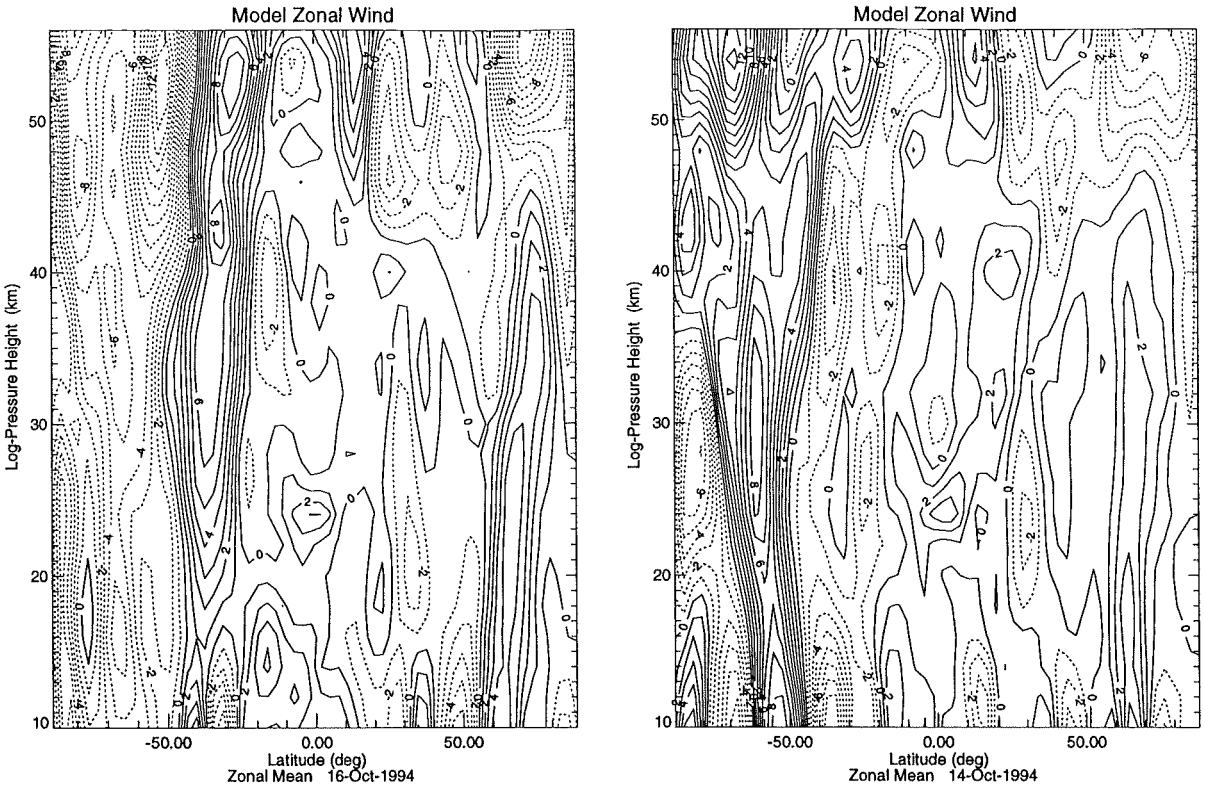

Fig 5.7(a) and (b). Zonal mean difference plots between analysed zonal wind and four-day forecasts of (a) 16 October 1994 and (b) 14 October 1994.

The direction of the +/- dipoles associated with the polar jet in figures 5.7(a) and (b) suggest that on those occasions the jet has been forecast (a) too far poleward and (b) too far equatorward.

The increase in errors at the top of the model throughout the atmosphere is most probably due to the proximity to the model lid and the lack of gravity-wave parameterisation there (being replaced by Rayleigh friction through the middle and upper stratosphere).

5.6 General Model Forecast Performance

The general performance of the model forecast fields was measured by calculating root mean square errors (RMSE) for differences between analysis and forecast fields as well as analysis and persistence fields. A standard RMSE was calculated in the following way,

$$RMSE = \sqrt{\frac{\sum_{i=1}^{n} (A_i - F_i)^2}{n}} \qquad (5.1)$$

where A is the analysis field, F the forecast field with the sum taken over the n grid points in the chosen domain. RMS errors for persistence were calculated by replacing the forecast fields in the above equation with the initial analysis field. For example, the forecast RMSE for 9 October uses the analysed field for 9 October with the 1-day forecast from 8 October while the persistence RMSE for 9 October uses the analysed field for 9 October with the

analysed field for 8 October. Therefore a prediction based on persistence is simply saying 'the field tomorrow will be the same as it is today'.

The calculations were performed for temperature, winds and geopotential at three heights of 20km, 32km and 48km, for three latitude regions in the Southern Hemisphere of 55°S-SP, 45°S-SP and 25°S-60°S. These regions were chosen primarily to allow comparison of results with those of *Waugh et al. (1997)*. Furthermore, 20km is around the height at which most of the ozone depletion occurs and the location of the coldest part of the vortex, 32km is around the middle of the stratosphere close to the maximum winds in the vortex and 48km is roughly the level of the stratopause and close to the model lid.

Lahoz (1997) also conducted a performance analysis entirely similar to that here and of *Waugh et al. (1997)* but with a view to determine the forecast skill in the lower stratosphere of three different versions of the UKMO model during October 1994. The three versions had: (1) 49 levels (L49), a model top at 0.1hPa (with the lid at 0.08hPa) and ~1.3km resolution, (2) 19 levels (L19), a model top at ~5hPa (with the lid at 0.5hPa) and ~5km resolution in the lower stratosphere and (3) 43 levels (L43), a model top at ~1hPa (with the lid at 0.5hPa) and ~1.3km resolution.

5.6.1 October 1994

Analysis for October 1994 was performed for a series of six overlapping five-day forecasts with the first field on 9, 11, 13, 16, 17 and 19 October 1994. RMS errors were calculated for each field in each file and then averaged according to forecast period across the files to give mean values for each successive forecast day.

Figures 5.8(a)-(d) present plots of forecast period vs. RMSE for temperature, zonal wind, meridional wind and geopotential respectively. Errors between analysis and forecast fields are shown in blue while errors between analysis and persistence fields are given in red. Both have ± one standard deviation error bounds indicated by the dotted lines with the appropriate colour. Each sequence of nine plots covers the three different regions at each of the three heights with the region and height stated in the title of each sub-plot.

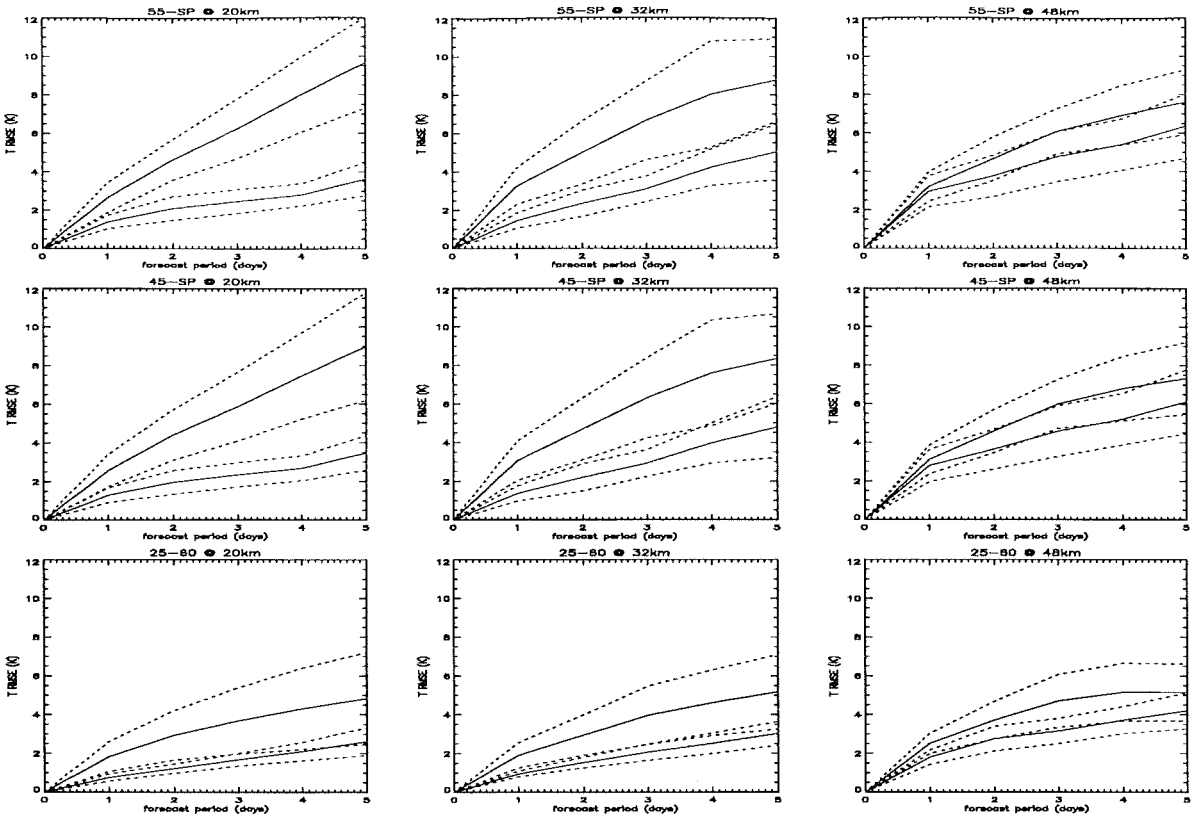

Fig 5.8(a). Temperature RMSE, Oct 1994. Forecast is in blue and persistence in red (solid) both with ± one standard deviation error bounds (dotted).

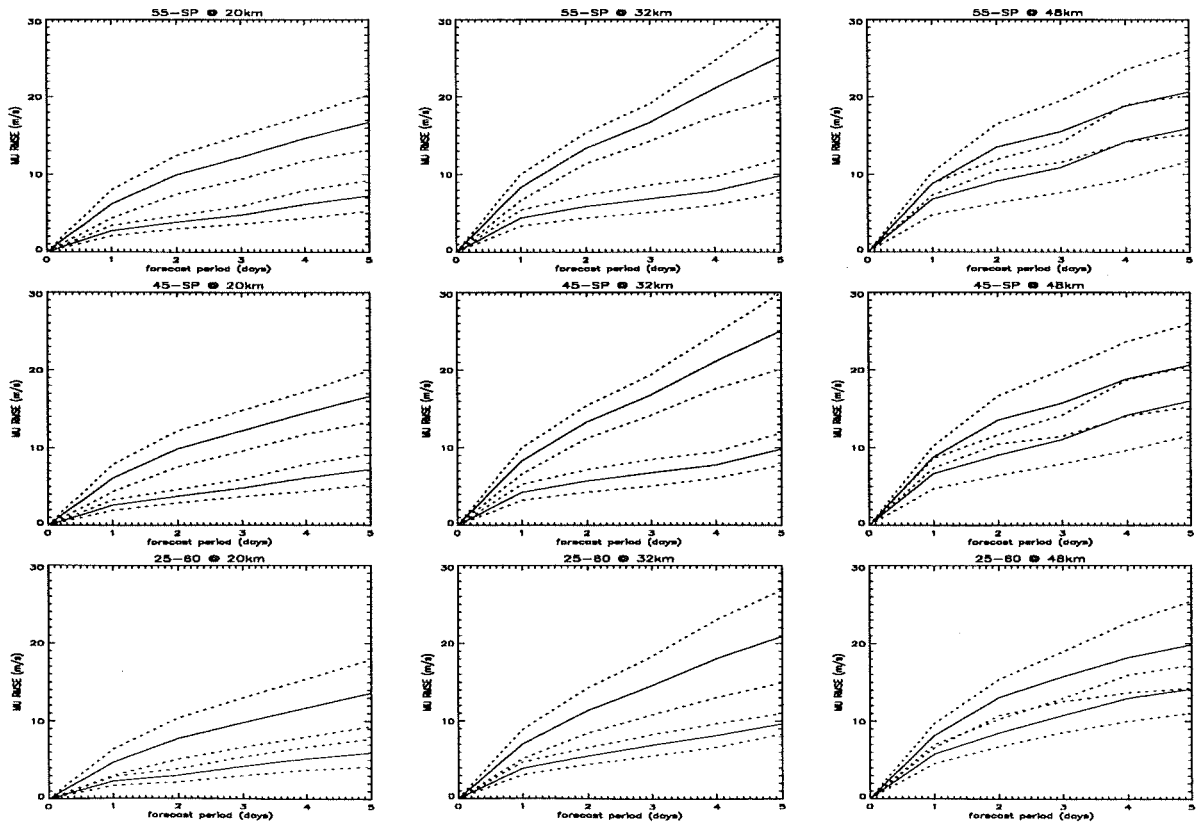

Fig 5.8(b). Zonal wind RMSE, Oct 1994. Forecast is in blue and persistence in red (solid) both with ± one standard deviation error bounds (dotted).

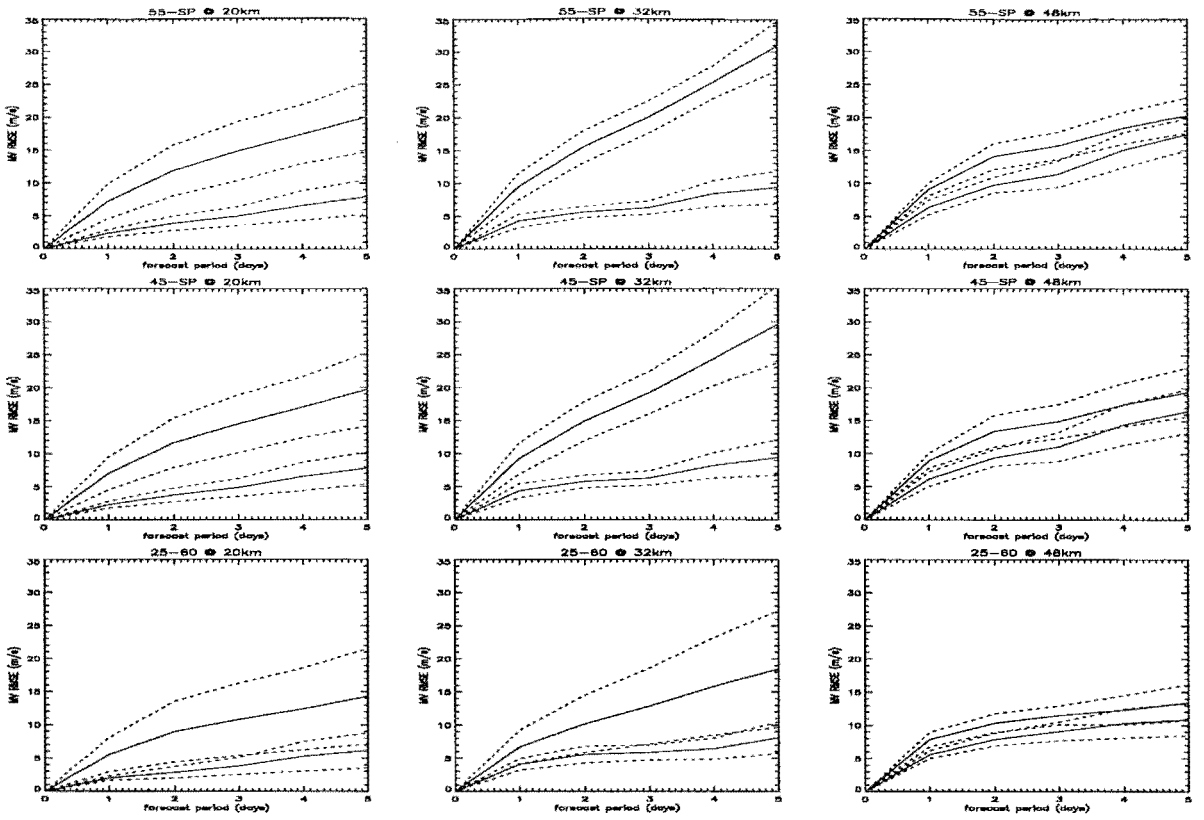

Fig 5.8(c). Meridional wind RMSE, Oct 1994. Forecast is in blue and persistence in red (solid) both with ± one standard deviation error bounds (dotted).

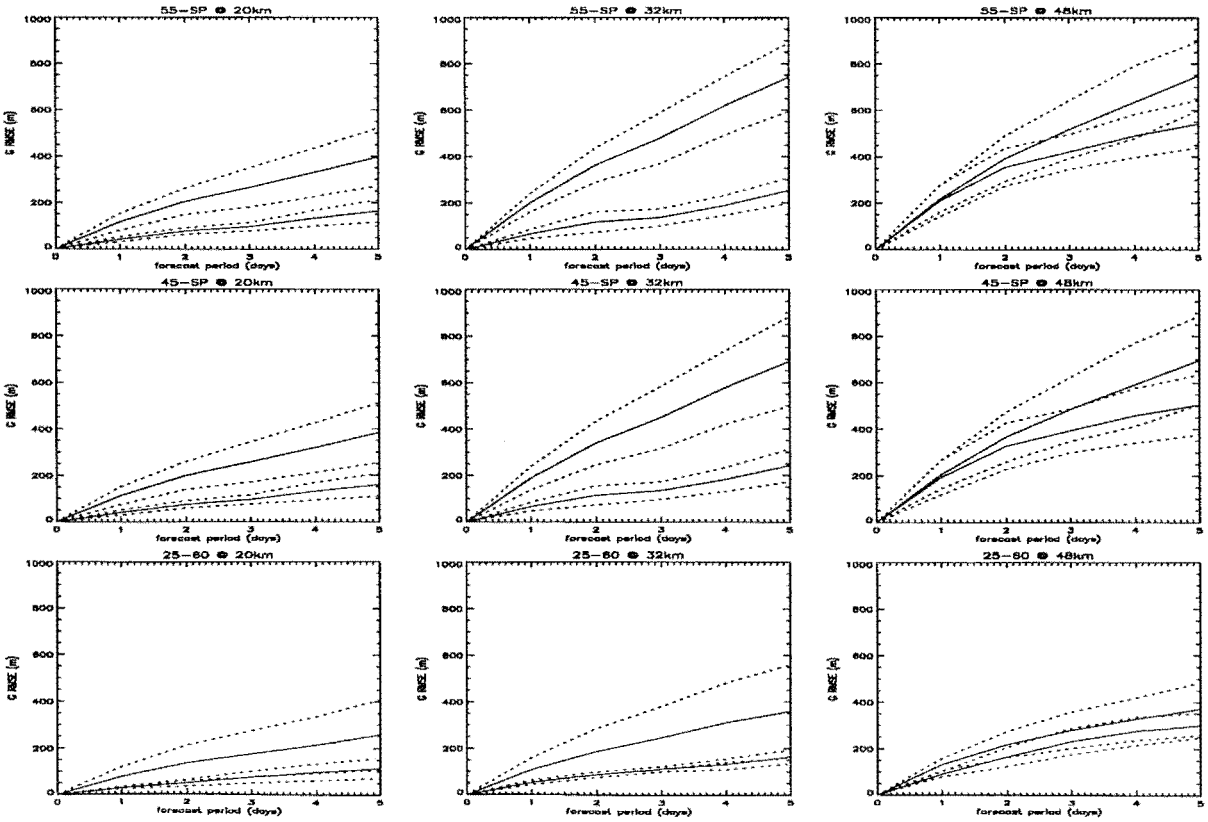

Fig 5.8(d). Geopotential RMSE, Oct 1994. Forecast is in blue and persistence in red (solid) both with ± one standard deviation error bounds (dotted).

The smallest errors measured were at 20km in the latitude annulus from 25°S-60°S followed closely by the other two regions also at 20km. At 48km there was often an entire overlap of the persistence error bounds with the RMSE values for the forecasts, indicating our ability to forecast accurately at that height is poor. The largest errors were at 48km most probably due to the proximity of the model lid. These observations were consistent through all quantities, for example, zonal wind RMSE in the region 55°S-SP at five days was ~7±2m/s at 20km and ~16±4m/s at 48km.

A measure of the forecast skill is to compare the errors obtained from a persistence field with those from a forecast field. In all cases the model forecasts perform better than persistence but by varying amounts over the different regions. In the region 55°S-SP the forecast RMSE for temperature at five days was ~37% of persistence at 20km, ~60% at 32km and ~84% at 48km showing a decreasing skill for prediction over that region with height. Zonal wind comparisons over the same region showed that forecast RMSE also at five days was ~42% of persistence at 20km, ~39% at 32km and ~78% at 48km. Again the poorest performance was at 48km although the best gain over persistence this time was at 32km, close to the strongest winds in the polar jet for that time of year.

Comparison of the above results with those of *Waugh et al. (1997)* shows that RMSE values are similar but slightly less in magnitude indicating a marginally better performance of the UKMO model over the ABOM's GASP. The temperature RMSE for example at 20km in the region 45°S-SP for a five-day forecast was ~4.5K for the Australian model and ~3.5K for the UK model, both with one standard deviation errors of ~1K.

It is difficult to compare the numerical results of *Lahoz (1997)* with those above although they appear to be in close agreement. *Lahoz (1997)* concluded that all three versions of the model (L49, L43 and L19) show significant improvement over persistence and that increased forecast skill is achieved by a better representation of the stratosphere with more levels in the vertical. Both the L49 and L43 versions had significantly more skill in the lower stratosphere for T, G and MU than the L19 version. As well as the RMSE calculations *Lahoz (1997)* also computed the anomaly correlation (AC) and the bias of the forecast fields. The bias found for the zonal wind showed that the model forecast tended to overestimate the zonal wind consistent with a deeper vortex and stronger westerly winds supporting the findings of section 5.2.2.

5.6.2 February 1995

The same analysis was applied to a series of forecasts in February 1995 for comparison of model forecast performance in winter with that of summer. Five overlapping seven-day forecast files were available with the first field in each file on 29 January, 1, 5, 8, and 13 February 1995. RMS errors were calculated and averaged in the same way as for October 1994 and plots for forecast period vs. combined RMSE for temperature, zonal wind, meridional wind and geopotential are shown in figures 5.9(a)-(d) respectively. Again errors between analysis and forecast fields are shown in blue while errors between analysis and persistence fields are given in red. Both have ± one standard deviation error bounds indicated by the dotted lines with the appropriate colour. The presentation of plots is the same as for October 1994 with the region and height stated in the title of each sub-plot.

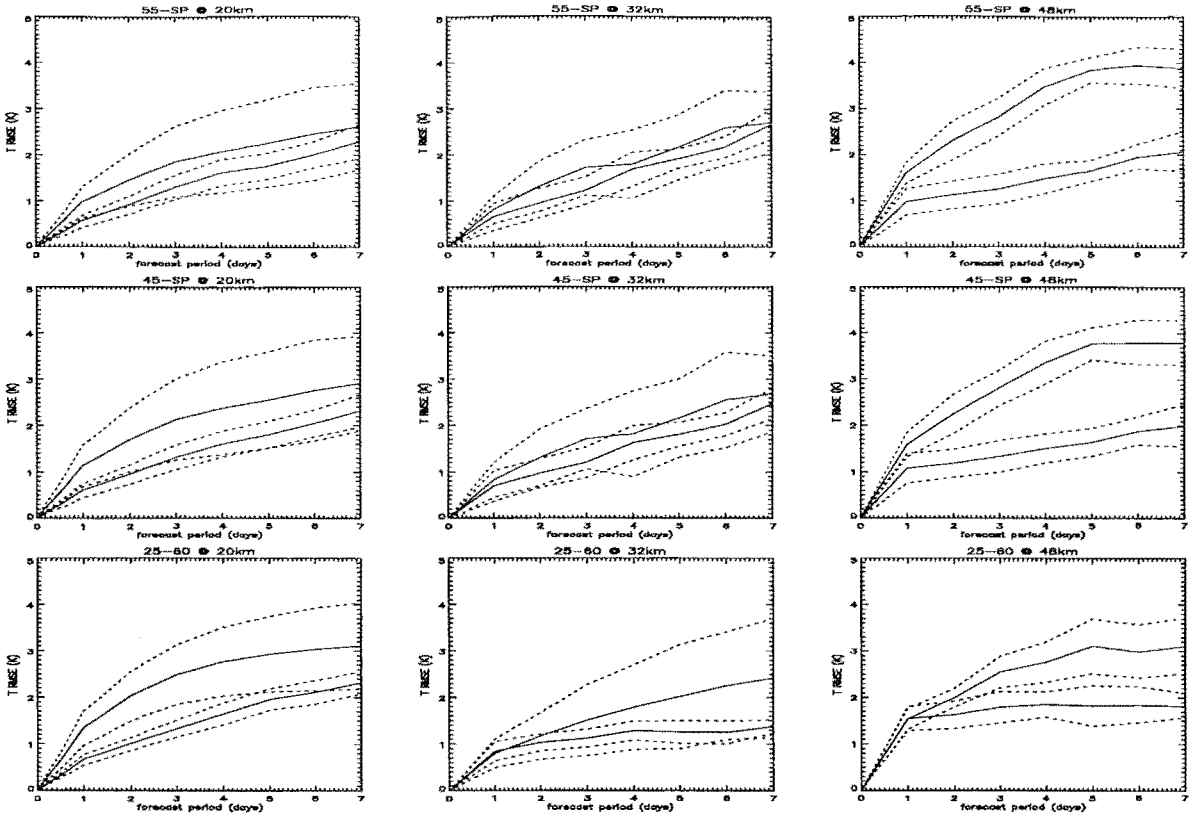

Fig 5.9(a). Temperature RMSE, Feb 1995. Forecast is in blue and persistence in red (solid) both with ± one standard deviation error bounds (dotted).

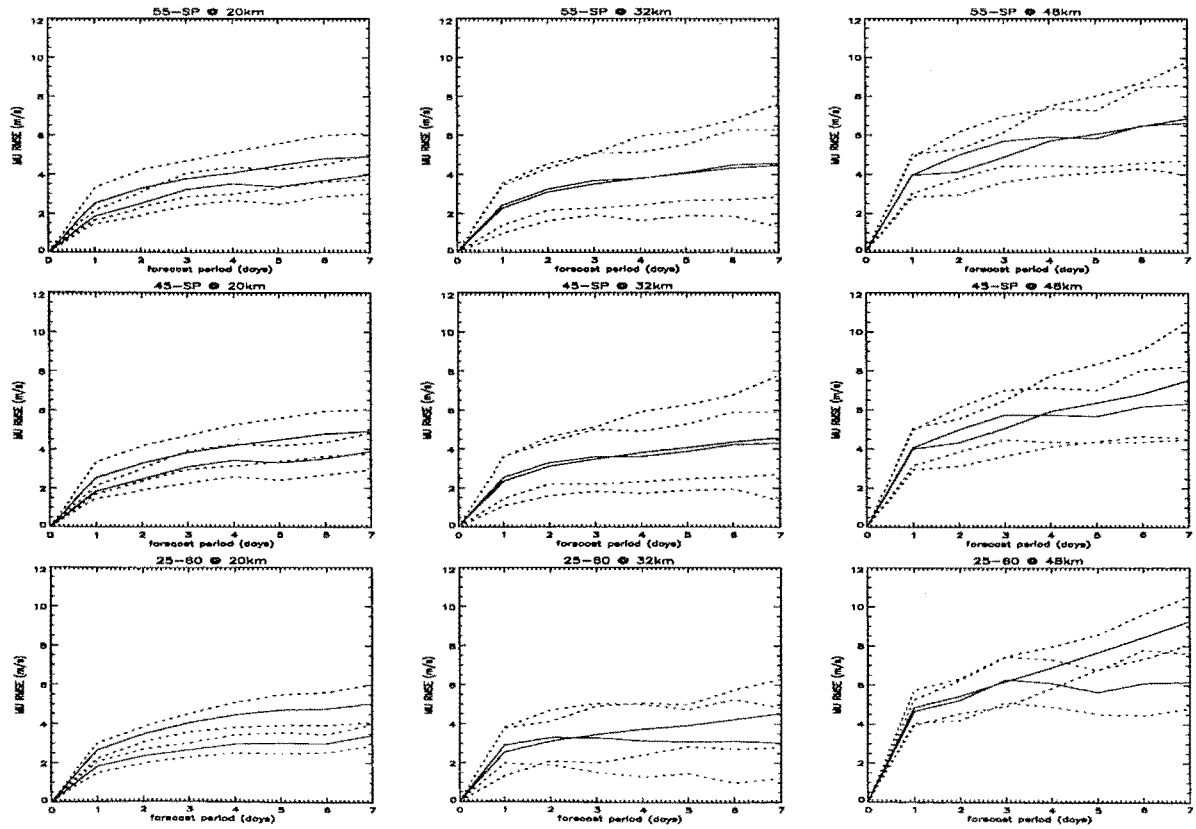

Fig 5.9(b). Zonal wind RMSE, Feb 1995. Forecast is in blue and persistence in red (solid) both with ± one standard deviation error bounds (dotted).

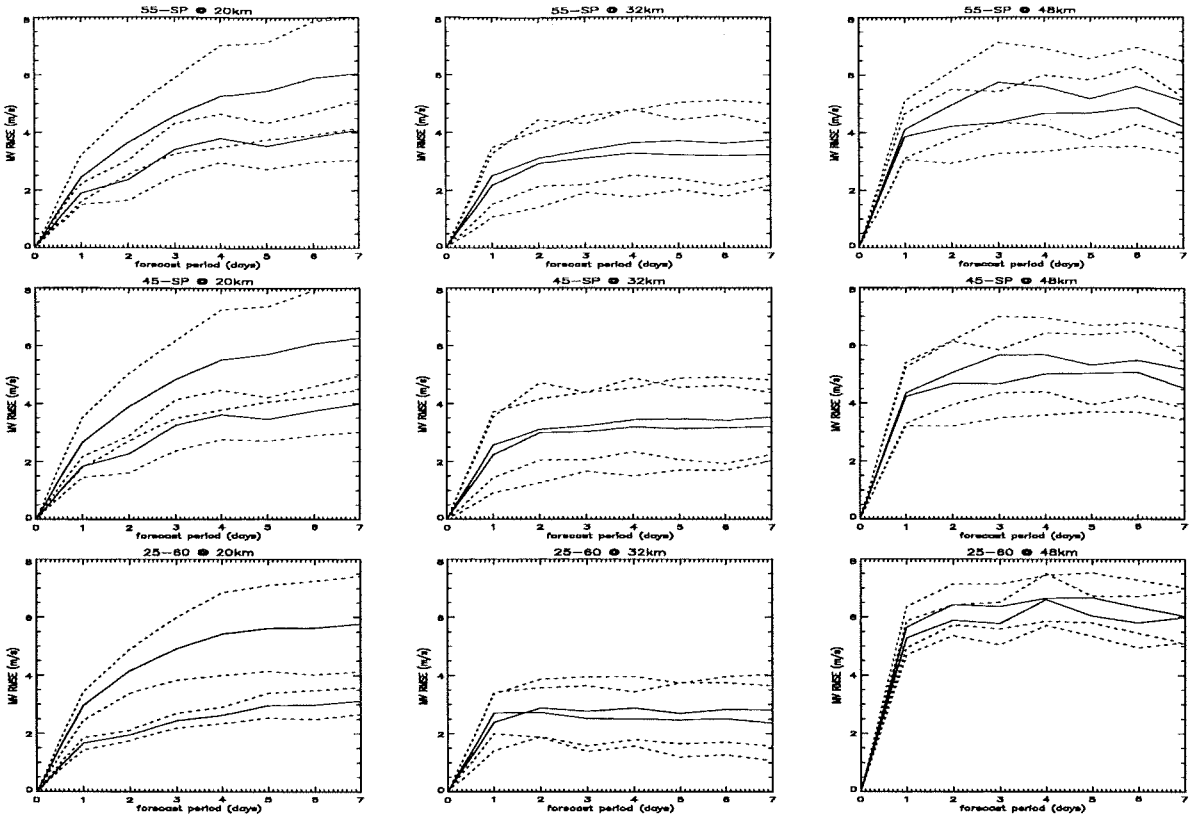

Fig 5.9(c). Meridional wind RMSE, Feb 1995. Forecast is in blue and persistence in red (solid) both with ± one standard deviation error bounds (dotted).

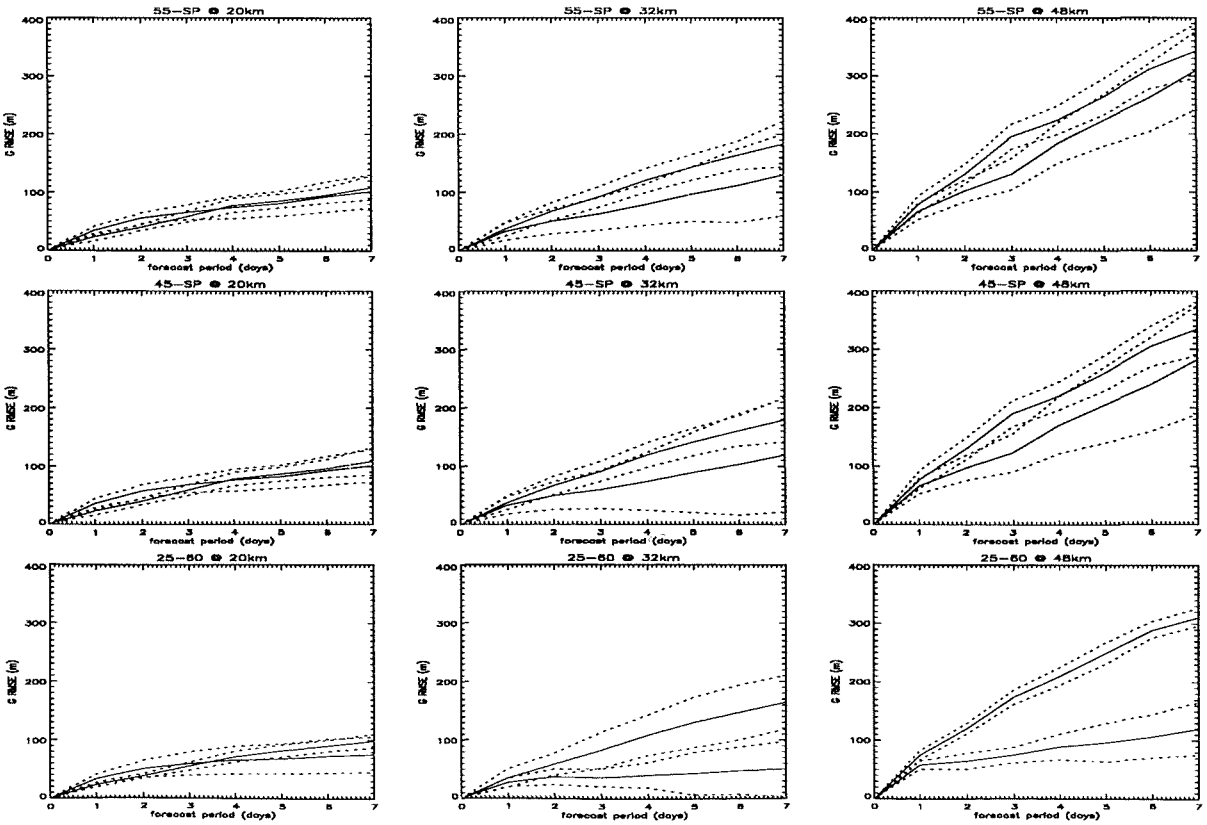

Fig 5.9(c). Geopotential RMSE, Feb 1995. Forecast is in blue and persistence in red (solid) both with ± one standard deviation error bounds (dotted).

The plots for February 1995 (SH Summer) reveal quite a different story to those of October 1994 (SH winter). Despite forecast RMS errors being smaller than the RMS errors for persistence at 20km for most cases, forecast ability is generally poor through all regions and heights indicated by the overlap of the persistence error bounds with RMSE values for forecast differences. In many cases at 32km and 48km RMSE values for persistence were actually smaller than those calculated from the forecast fields. For example in the region 55°S-SP at 48km, temperature RMSE for persistence is ~45% of the model forecast RMSE. The means that the model is predicting a larger change in the state of the atmosphere over those regions than is actually occurring. Values of RMS errors are however smaller in magnitude for forecasts in summer than in winter highlighted by an example of temperature RMS errors over the region 55°S-SP at 48km. In October the average five-day forecast RMSE was ~6.4±1.7K while for February was ~3.9±0.3K.

Again forecast ability at 48km close to the model lid is poor and errors were smallest at 20km and grew in all cases with increasing forecast period.

The most probable cause for the poor performance of the model in the Southern Hemisphere summer is the lack of dynamical control of the atmosphere at that time. During winter the polar vortex dominates the winter hemisphere stratosphere which the above results suggest is modelled significantly better than the summer hemisphere.

5.6.3 RMSE Height Variation

As an extension of the previous analysis, the height variation of the RMS errors was investigated over the region 45S-SP for each of the quantities temperature, winds and geopotential. This region was chosen as it encompasses the polar vortex in the winter and as a contrast, the same analysis was applied to the February data in the absence of the vortex.

Figures 5.10(a)-(d) present the RMSE vs. height plots for both October 1994 and February 1995. Each plot gives the errors associated with the different forecast periods. Since the errors increase with forecast period, the line on the far left of each plot represents the one-day forecast while the line on the far right is for the five-day forecast in the October case and the seven-day forecast in the February case.

The plots clearly show the errors are smaller in the summer than in the winter although do maintain the same structure. For example, consider figure 5.10(a) showing the RMS errors for temperature. At both times of the year the two largest error locations in the stratosphere are at 38km and 50km as previously outlined in section 5.4 due to the incorrect position of the warm stratopause. Furthermore errors are generally smaller toward the bottom of the stratosphere between 15km and 20km with the largest errors around the stratopause and tropopause.

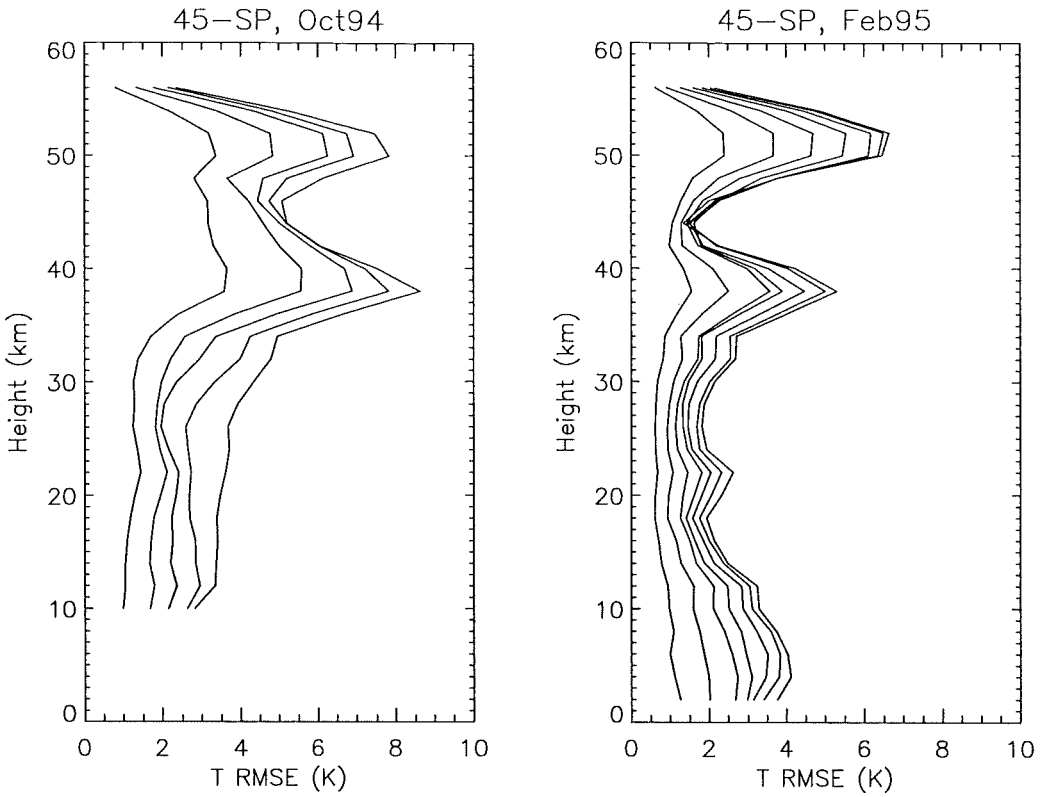

Fig 5.10(a). Height variation of the temperature RMSE in October 1994, forecast days 1-5 (left) and in February 1995, forecast days 1-7 (right).

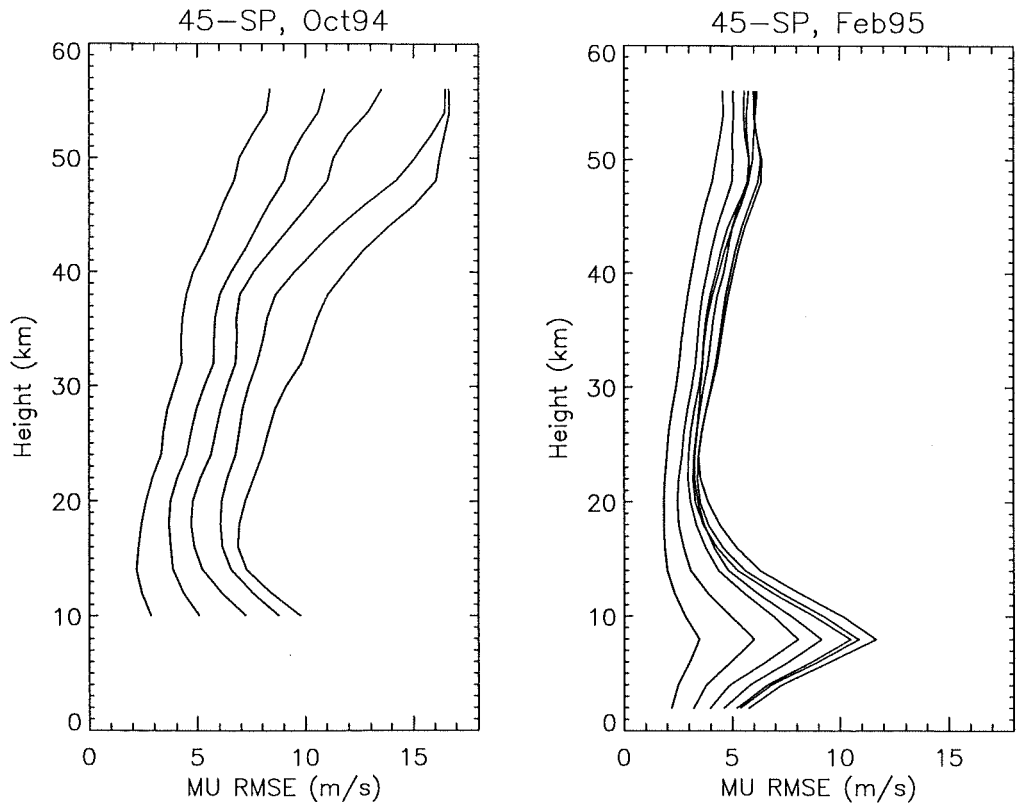

Fig 5.10(b). Height variation of the zonal wind RMSE in October 1994, forecast days 1-5 (left) and in February 1995, forecast days 1-7 (right).

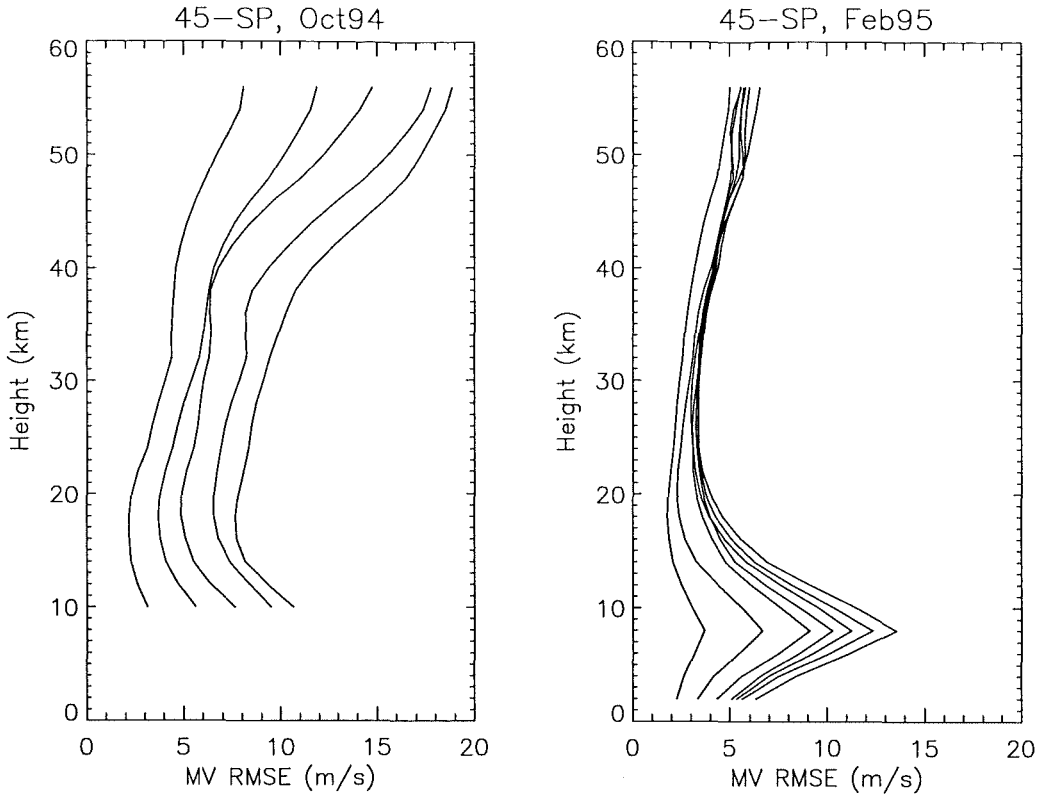

Fig 5.10(c). Height variation of the meridional wind RMSE in October 1994, forecast days 1-5 (left) and in February 1995, forecast days 1-7 (right).

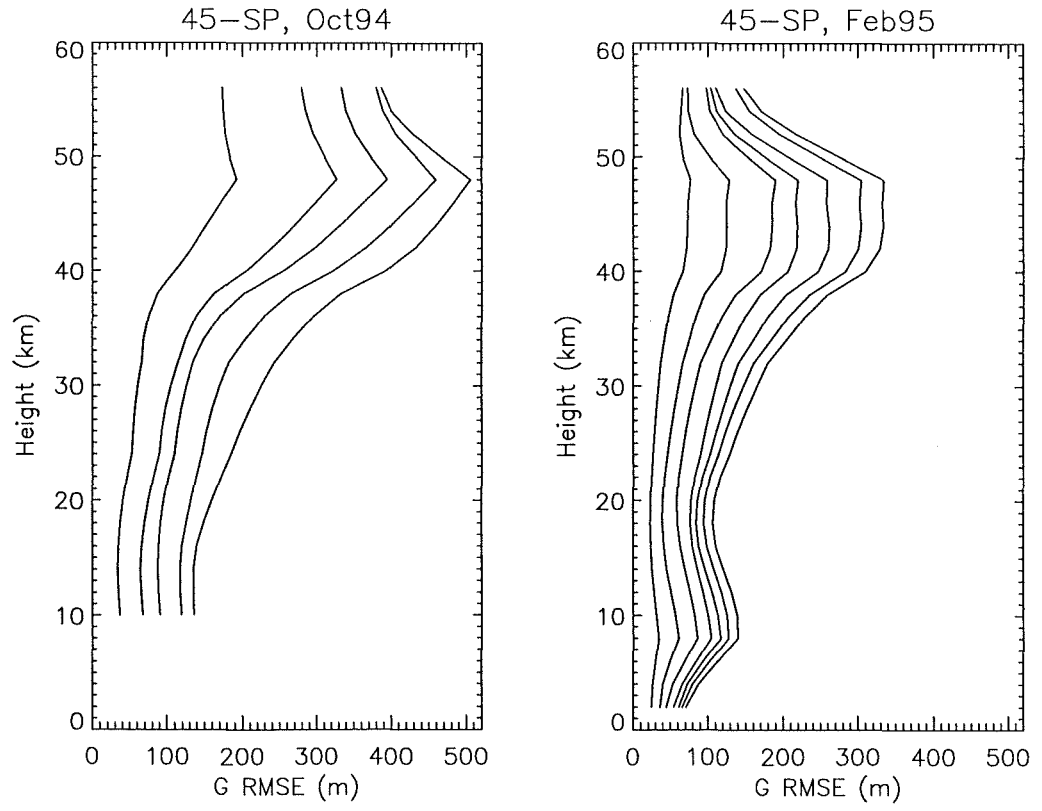

Fig 5.10(d). Height variation of the geopotential RMSE in October 1994, forecast days 1-5 (left) and in February 1995, forecast days 1-7 (right).

5.7 Aircraft/Model-Assimilation Temperature Comparisons

To this point analysis of model performance has concentrated on comparisons of analysed fields with forecast fields. We now turn to an independent data source for the purposes of verifying the accuracy of the model fields. For this study the ASHOE aircraft measurements are used to compare with both the analysed and forecast fields during the Southern Hemisphere winter when flights were made from Christchurch, New Zealand.

Of the 26 flights made from Christchurch plus the two transit flights, 10 had available UKMO analysis fields for comparison (see Appendix A and B). Flight data collected from each flight was interpolated into the appropriate UKMO analysed temperature field for comparison with the outside air temperature (OAT) readings from the ER-2 meteorological measurement system.

All of the UKMO analysed data fields were generated for 1200 Universal Co-ordinated Time (UTC), however the flights made from Christchurch spanned mid-day New Zealand Standard Time (NZST) which corresponds to 0000 UTC. To overcome this large time difference when making comparisons, consecutive UKMO fields were simply averaged to give a best approximation of the state of the atmosphere at 0000 UTC, which normally fell mid-way through the flight. This still leaves a time difference between the start and finish of the flight with the model field time of around four hours, thus for the purpose of this study it is assumed that the temperature field does not change significantly over these timescales.

The flight dates (UTC) used in the analysis were 28 May, 1 August and 22 October for flights north of New Zealand and 1 June, 28, 30 July, 10, 13, 16, and 20 October for flights south of New Zealand. All differences here are calculated as aircraft minus model where the ER-2 data has been taken as the best measurement of the true state of the atmosphere along the aircraft track within the accuracy of the instrument.

Results show a distinct bias towards the ER-2 measuring the temperature warmer than the model temperatures and that flights north of New Zealand in general gave larger differences than those south of New Zealand. For example the average maximum difference for the flights north of NZ was ~6K while for flights south of NZ was ~4.5K.

One such example of the bias is given in figure 5.11(a) and (b) for the flight on 16 October 1994. The top plot gives the along track temperature profiles for both the aircraft (red) and the model (black) while the bottom plot shows the differences for the outbound leg (blue) and the inbound leg (green). Comparisons were only made for when the aircraft was established on track at altitude thus all climb and dive periods were ignored.

A second point worth noting here is that the model assimilation fields are gridded to 3° latitude by 3° longitude with 2km height resolution in the MADPO program, while the ER-2 samples temperature every second (see sample data file in Appendix B) corresponding to a horizontal distance of about 200m. Figure 5.11 shows straight differences for all aircraft data points before any averaging has taken place. Later data is averaged every degree to remove the large amount of fine structure not present in the model fields. That resolution was also chosen as it is obtained by the back trajectory analysis scheme.

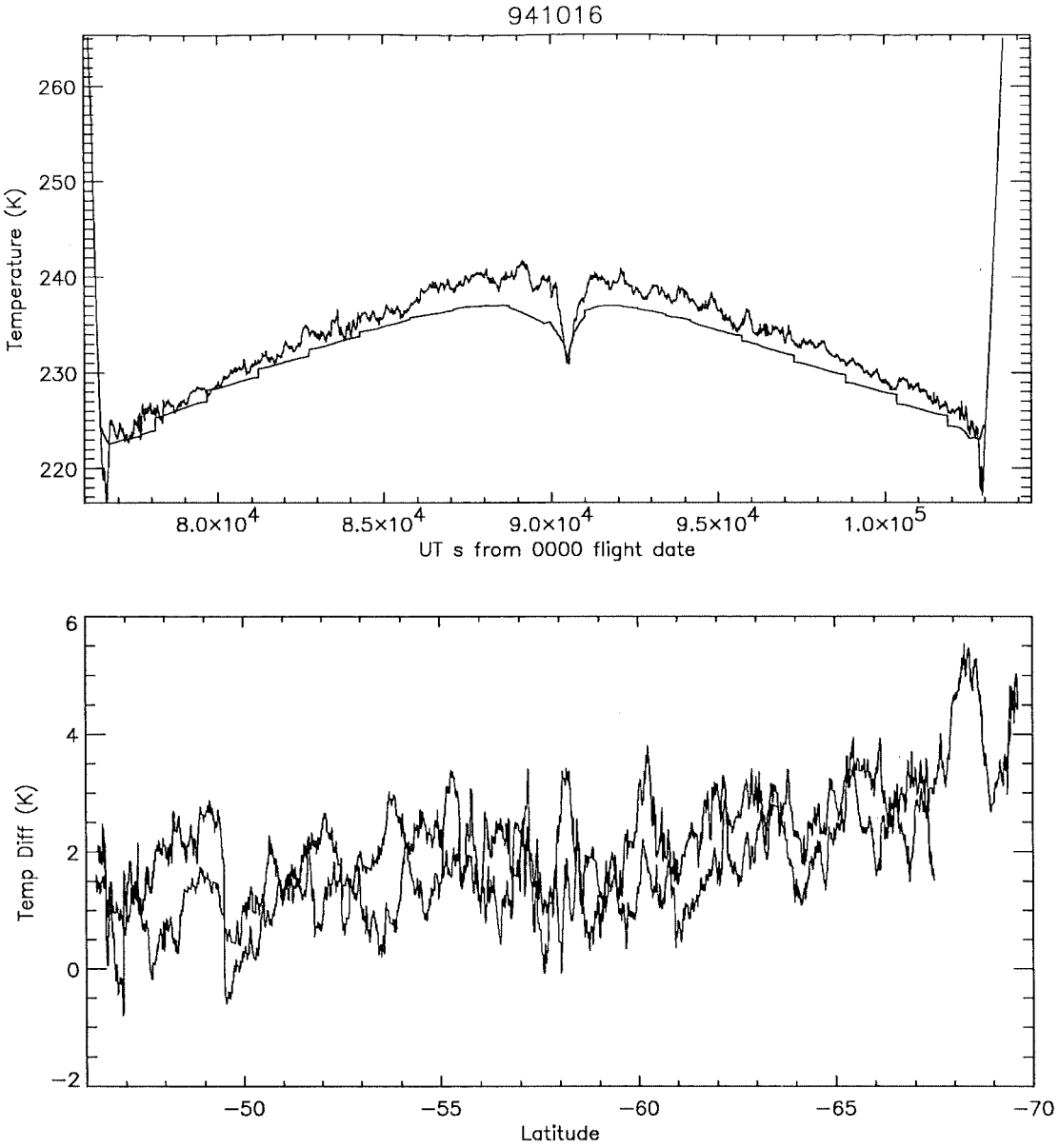

Fig 5.11(a) and (b). (a) Aircraft measured temperature (red) and analysed temperature (black) as a function of time and (b) the differences for the outbound and inbound tracks (blue and green lines respectively).

As can be seen from both plots, there is a distinct bias towards the model assimilation producing cooler temperatures than the aircraft measurements with differences increasing approaching the pole. On this occasion the largest difference was ~5.5K at ~68°S.

When the temperature difference is combined for each flight leg and averaged into one-degree bins, the variation of errors for the seven flights south of NZ was roughly -0.7K to 4.5K, with a larger variation of roughly –2.3K to 6.3K for the three flights north of NZ. The mean temperature difference and mean RMSE for flights north and south of NZ and averaged by month are shown in figure 5.12(a) and (b). The red lines represent flights at the end of May (28 May (N) and 1 June (S)), the green lines for flights at the end of July (28 and 30 July (S) and 1 August (N)) and the blue lines for flights during October (10, 13, 16 and 20 (S) and 22 (N)) all during 1994.

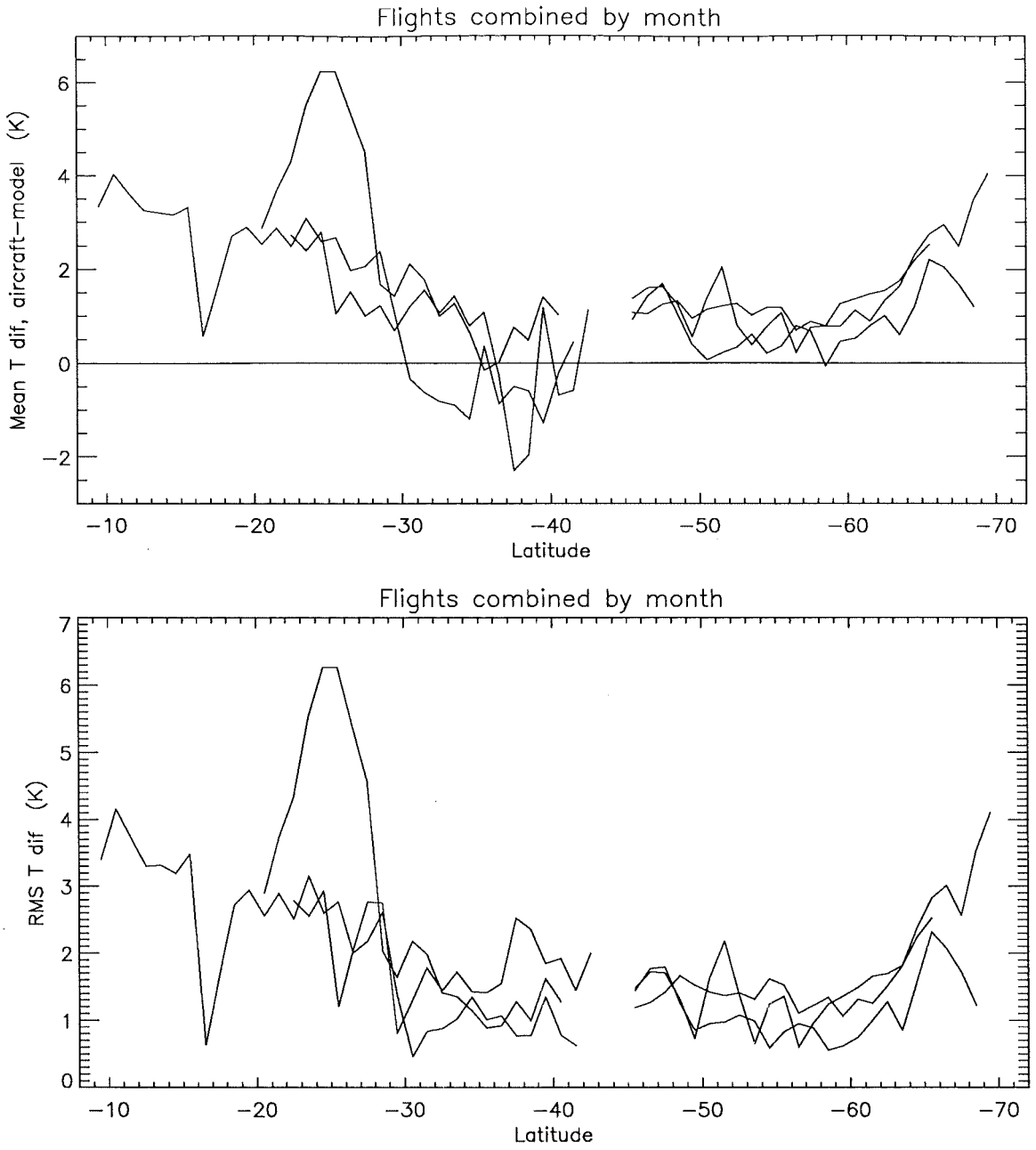

Fig 5.12(a) and (b). (a) Mean temperature difference at 1° resolution for aircraft OAT minus model-analysed temperature for flights from Christchurch. (b) Mean RMSE for the same flights. The red lines represent flights at the end of May, green for flights at the end of July and blue for flights during October.

Note that the profiles for flights north of NZ are comprised of only one flight in each case and in fact only one leg for the flights on 1 August and 22 October (as the former had the return leg discarded due to a second dive period and the latter was a transit flight with only one leg). As a result the northward profiles in figure 5.12 exhibit considerably more variability than those south of NZ which are an average of multiple legs and flights. Note also that the latitude range of the profiles in figure 5.12 vary due the different length of individual flights and the time spent in the climb or dive periods. Again the bias between the model and the aircraft temperatures can be seen clearly in 5.12(a) for flights south of NZ. The increase in the errors toward the pole, especially in October, shows the polar region in particular is too cool in the model assimilation compared with the real atmosphere. A possible cause for this

cold bias is outlined by *Garcia et al. (1994)*. They studied the effects of gravity-wave drag on the mean meridional circulation in the mesosphere and on the temperature distribution at lower levels in the polar winter stratosphere. Their results suggested "that the omission of gravity-wave drag in the mesosphere could be the cause of the cold bias in GCM simulations of the polar winter stratosphere, particularly in the Southern Hemisphere" [*Garcia et al. (1994)*].

Comparisons of aircraft temperature with forecast temperatures showed more variation with several cases over-predicting temperature and several under-predicting. Figure 5.13 shows the same case as that for 5.11 previously, but for comparison of aircraft temperature with forecast temperature. The aircraft temperature profile is again that for 16 October 1994 compared with a 4½-day forecast temperature field. The ½ day arises due to the fact that the forecast fields are for 1200 UTC each day, but the flight-time is either side of 0000 UTC.

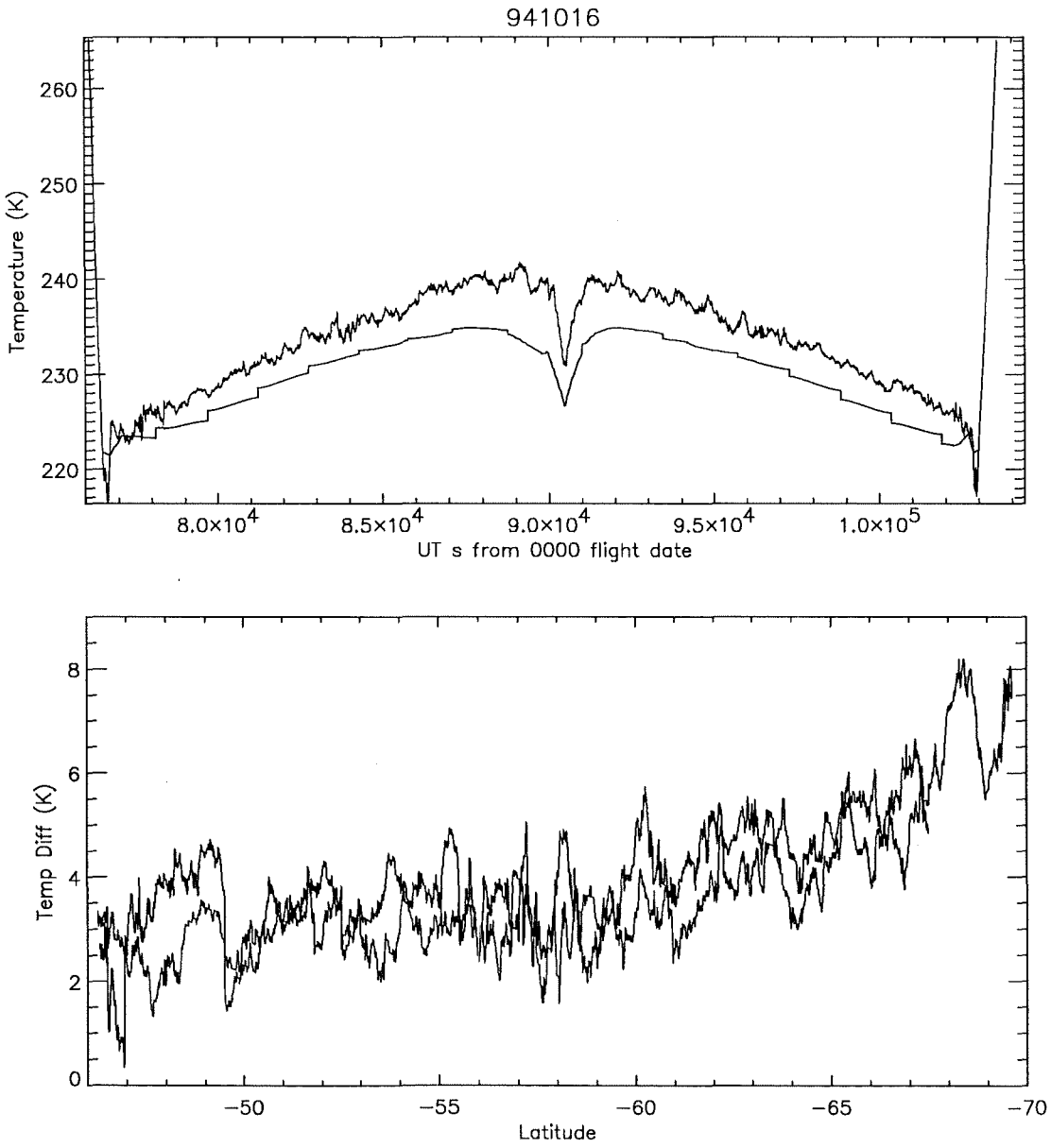

Fig 5.13(a) and (b). (a) Aircraft measured temperature (red) and 4½-day forecast temperature (black) as a function of time and (b) the differences for the outbound and inbound tracks (blue and green lines respectively).

The difference profile above exhibits the same bias as that for the analysed temperature except for the larger magnitude of the errors. Previously errors ranged from roughly 1K to 4K for the analysed winds and range from roughly 2K to 7K for the 4½-day forecast temperature field. Comparisons of aircraft and forecast temperatures were made for eight occasions of flights south of NZ at the end of July and in October 1994. Figure 5.14 shows the RMS errors as a function of latitude with profiles grouped according to the period of the forecast. The black line is the RMSE between the aircraft and analysed field while the red, green, purple and blue lines represent RMS errors for a 1½-day, 2½-day, 3½-day and 4½-day forecast respectively.

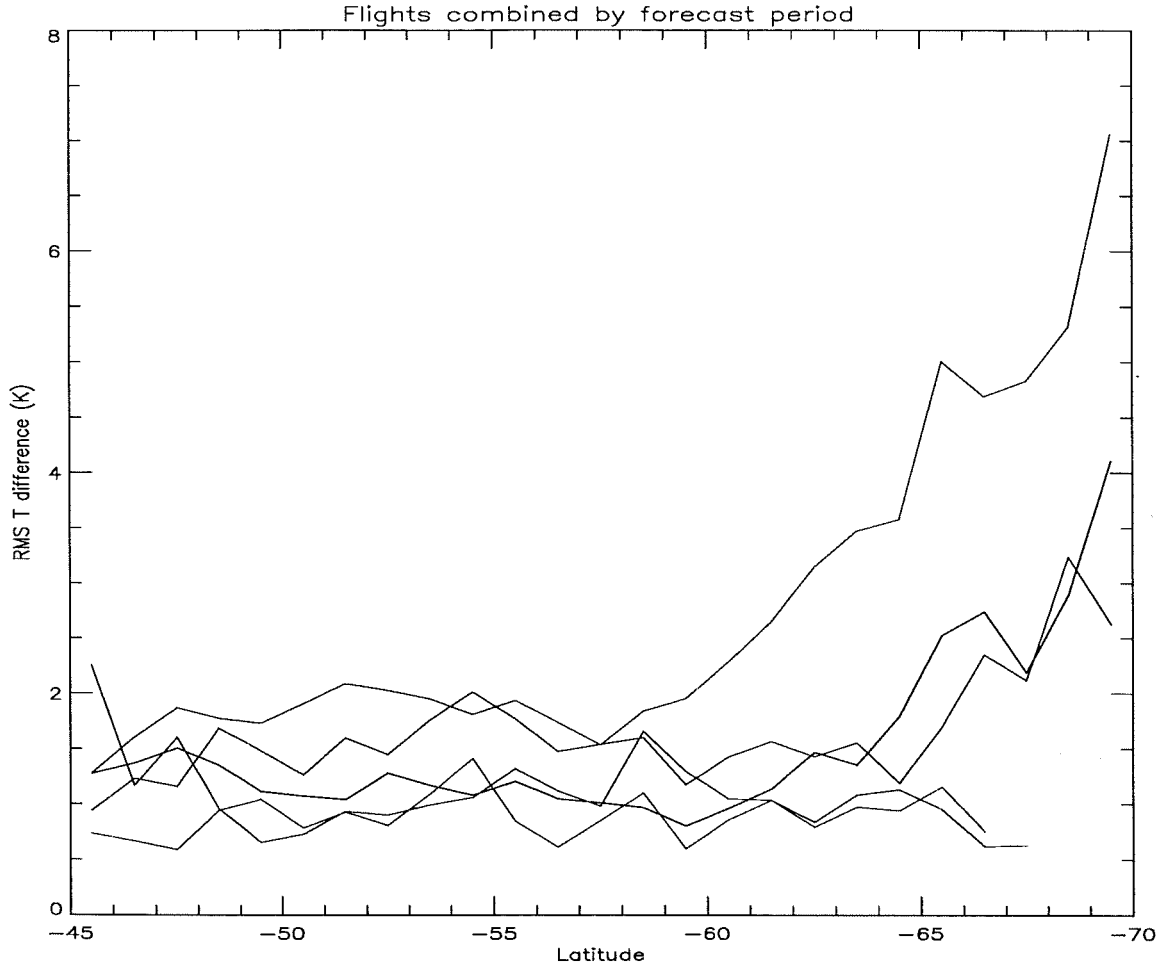

Fig 5.14. Mean RMSE for comparison of aircraft temperature with model fields. Black is for RMSE between aircraft and analysed temperature while red is for a 1½-day forecast field, green for a 2½-day forecast, purple for a 3½-day forecast and blue for a 4½-day forecast.

The larger variability in accuracy of the forecast temperatures is shown by the fact that all forecasts produce both larger and smaller RMS errors than the analysed temperature fields with the exception of the 4½-day forecast which had all RMS errors larger than the analysed field RMS errors.

It is difficult to draw solid conclusions from results such as these due to the large variability arising from a small number of comparisons. Note that the profile for the aircraft/model-analysed temperature RMSE is an average of 5 different occasions, on 28 and 30 July, and 13, 16 and 20 October. The aircraft/model-forecast temperature RMSE profiles are averages of 2

occasions for 1½-day forecasts (13 and 16 Oct, in red) and 2½-day forecasts (28 Jul and 20 Oct, in green) and 3 occasions for 4½-day forecasts (30 Jul, 16 and 20 Oct, in blue). Only one occasion was available for a 3½-day forecast comparison (13 Oct, in purple).

Despite the small number of comparisons, results show that aircraft/model RMS errors averaged per degree are generally less than 2K for all forecast periods in the region 45°S-60°S with RMS errors remaining less than 2K down to 65°S for forecast periods up to 3½ days.

5.8 Lagrangian Approach to Atmospheric Motion

Previously in this chapter, data analysis has concentrated on an Eulerian point of view for any comparisons that have been made. However, when generating high-resolution maps of potential vorticity for the study of filamentary structure, Lagrangian methods must be used for parcel trajectories. We now turn our attention to examining the accuracy of the forecast wind fields for the advection of parcels.

Atmospheric winds are dominated by zonal motion in the stratosphere, especially in the winter from mid-latitudes to the pole during the existence of the stable polar vortex. Winds are westerly (eastward) at higher latitudes and easterly (westward) at lower latitudes near the equator. To demonstrate this, initial positions for parcels were specified at each degree in latitude at four longitude values including the Greenwich Meridian and separated by 90°, thus giving a pole-centred cross. This cross was then advected forward in time for 24 hours by an analysed isentropic wind field. Figure 5.15 shows both the initial and final positions for the one-day advection from 9 October at 500K (~20km). The effect of the strong westerlies around Antarctica forming the polar jet (see figure 5.3) can be easily seen by the larger displacement between initial and final positions of parcels in the jet.

Despite the domination of the wind field by zonal motion, it is also important to accurately predict the meridional component of the wind vector since it is ultimately responsible for motion out of the vortex and hence the transport of ozone-poor air to mid-latitudes. A similar technique to that used above was employed to study the meridional motion as predicted by the forecast wind fields compared to the analysed wind fields. This time, 360 parcels were initialised on each of three rings at 20°S, 40°S and 60°S at each of three heights at 500K, 850K and 1900K (approximately 20km, 32km and 48km respectively) with a parcel separation of one degree on each ring. An example is presented in figure 5.16 that shows the result of three days advection on the 850K surface from 10 October 1994. Note that the parcel beginning on the Greenwich Meridian was coloured differently to the rest of the ring to demonstrate the zonal component of the motion.

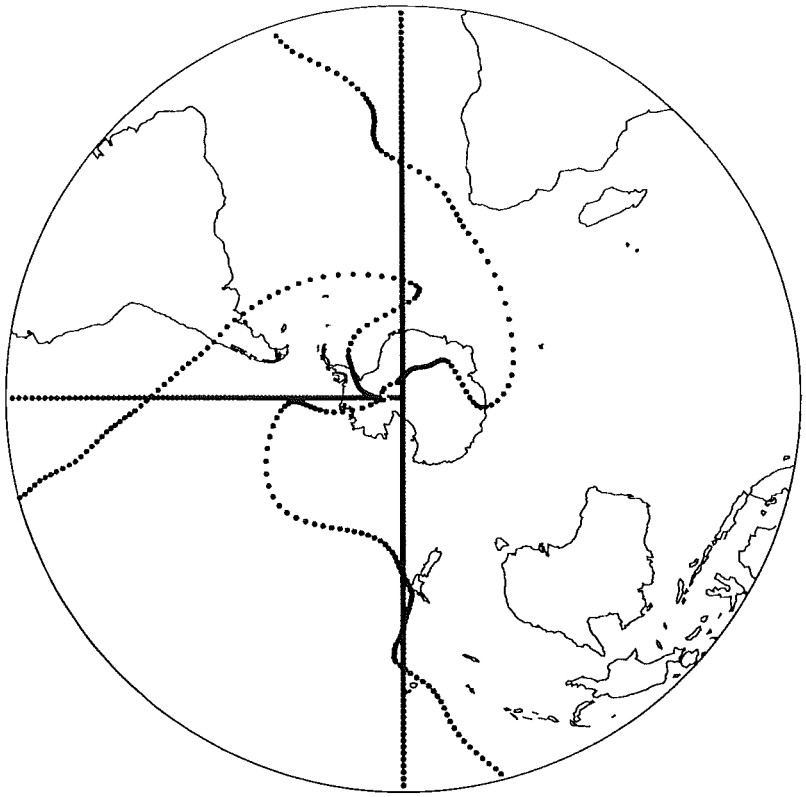

Fig 5.15. Polar stereographic plot showing the initial (the cross) and final positions of parcels that were advected forward in time for one day from 9 October 1994 at 500K. Note the effect of the strong polar jet around Antarctica.

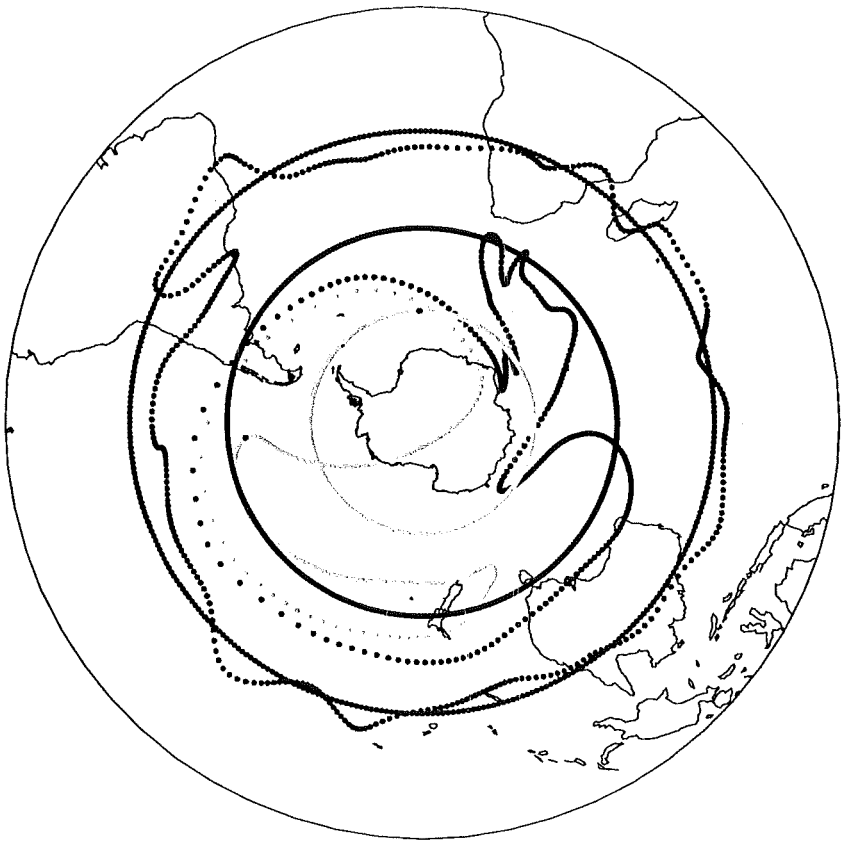

Fig 5.16. Initial and final positions for parcels initialised on three latitude rings at 850K and advected by isentropic winds for three days from 10 October 1994.

In figure 5.16, New Zealand sits under a large tongue of air (shown in yellow) that three days previously was confined to the region poleward of 60°S. It is enlightening to view the geopotential plot at approximately the same height for that time of the month since the winds follow the contours of geopotential and therefore the 'pressure systems' responsible for stripping air from polar latitudes and subsequent transport northward can be visualised. Figure 5.17 shows the geopotential field from a polar stereographic perspective for 11 October 1994 at 32km. The large low-pressure region associated with the vortex can be seen along with a high-pressure region that has drawn the large tongue of air from Antarctica and across New Zealand.

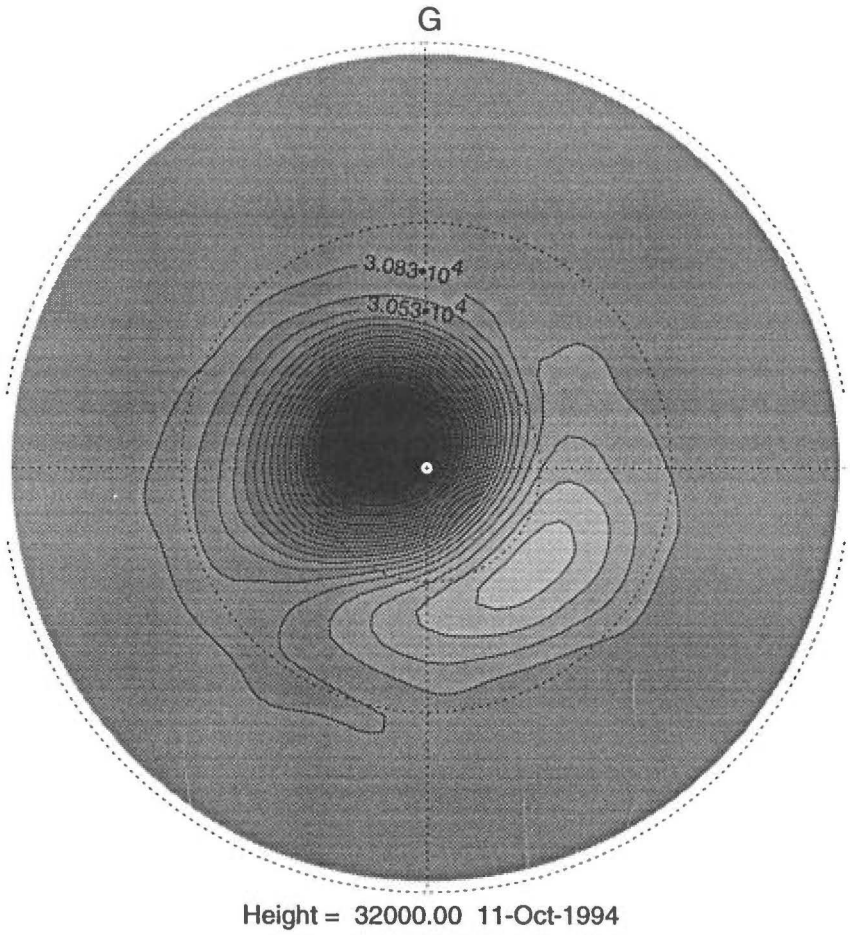

Fig 5.17. Geopotential plot centred on the South Pole for 11 October 1994 at 32km. Note the high-pressure region in the lower right of the plot, which draws air from the vortex region and around itself in an anti-clockwise direction.

To obtain a measure of how accurate the forecast winds are at advecting the rings over varying time periods, the differences between the initial and final positions of the parcels were averaged zonally for each ring. Results were compared for analysed isentropic wind fields with those for forecast isentropic winds. In the case of forecast winds, six specialised wind files were created with the first field being an analysed wind field (of say, 8 Oct), the second field a one-day forecast field (of 9 Oct), the third a two-day forecast field (of 10 Oct) etc. Files were created in this way so that interpolation during the advection scheme sees a sensible progression from known winds through the increasing period of the forecast fields.

The average meridional deviations from the initial positions of the rings at the three heights are shown in figure 5.18. Each profile is the average of the advection scheme applied to each of the six separate wind files that were created for periods in October 1994. Results for analysed winds are shown in blue with those for forecast winds shown in red, both with ± one standard deviation error bounds (dotted in the appropriate colours). Motion was carried out for periods varying from one to five days primarily as no forecast files in October extended longer.

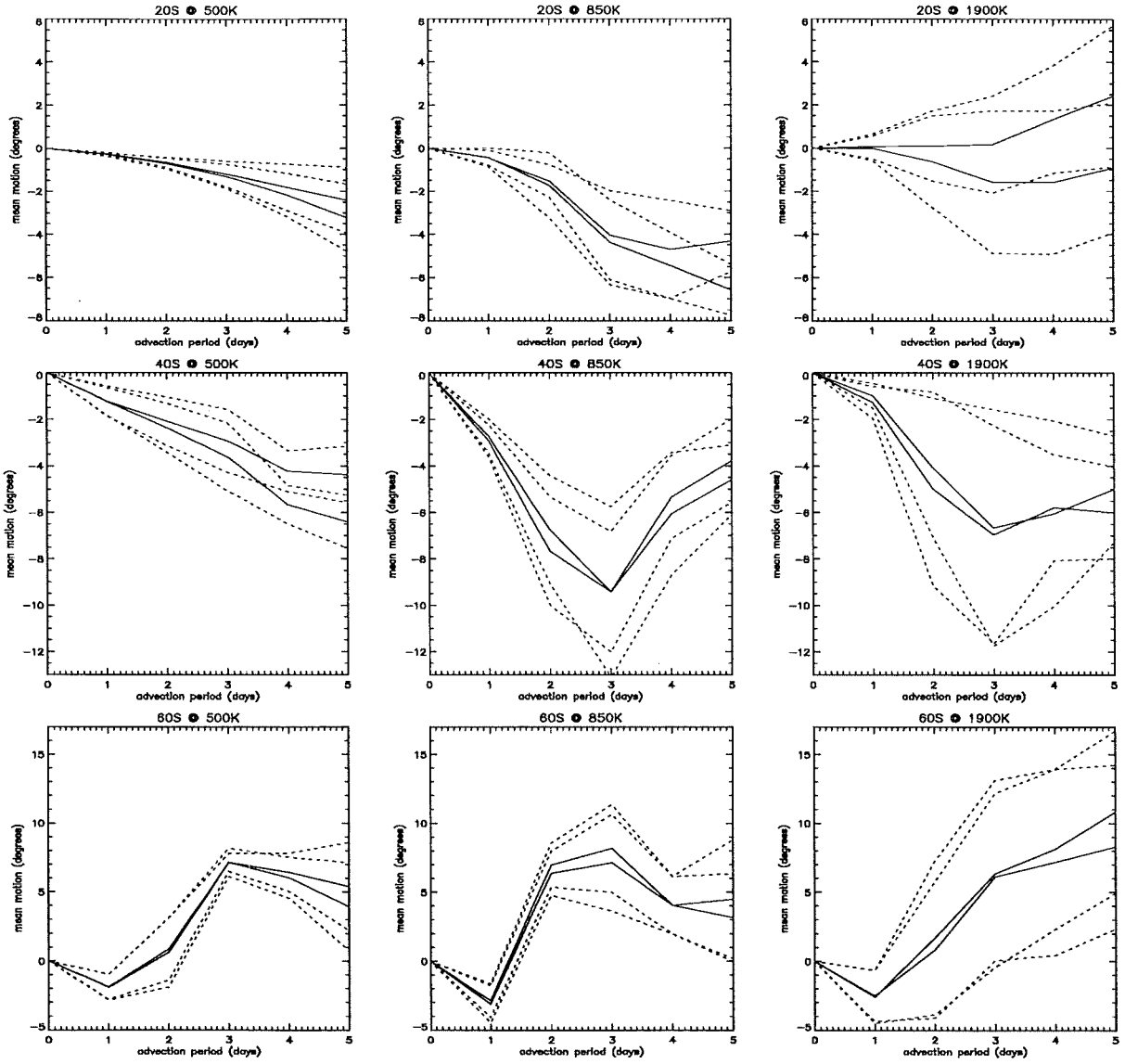

Fig 5.18. Results of the ring advection at heights of 500K, 850K and 1900K using both analysed (blue) and forecast (red) isentropic winds. One standard deviation error bounds are shown by the dotted lines.

The forecast wind fields did not consistently over- or under-predict the meridional motion but in general matched the analysed motion well indicated by the entire overlap of the error bounds in most cases. The only exception being for the advection of the 20°S latitude ring at 1900K where forecast motion on average was in completely the opposite direction. This is presumably due to being in the tropics where the winds are assimilated poorly in the model. Furthermore, 1900K (~48km) is close to the model lid where forecast ability is poorest.

Variability between the individual forecasts in October increased both with time and height shown by the increasing size of the error bounds.

It should be noted that the motion at 850K was northward from 60°S and southward from 40°S indicating that the transport was occurring at different geographical locations. Figure 5.16 demonstrates this well, showing on that occasion, the northward motion from 60°S was around the Pacific Ocean region and the southward motion from 40°S was around the Atlantic and Indian Ocean regions.

RMS errors between the forecast and analysed meridional motion of the rings are shown in figure 5.19.

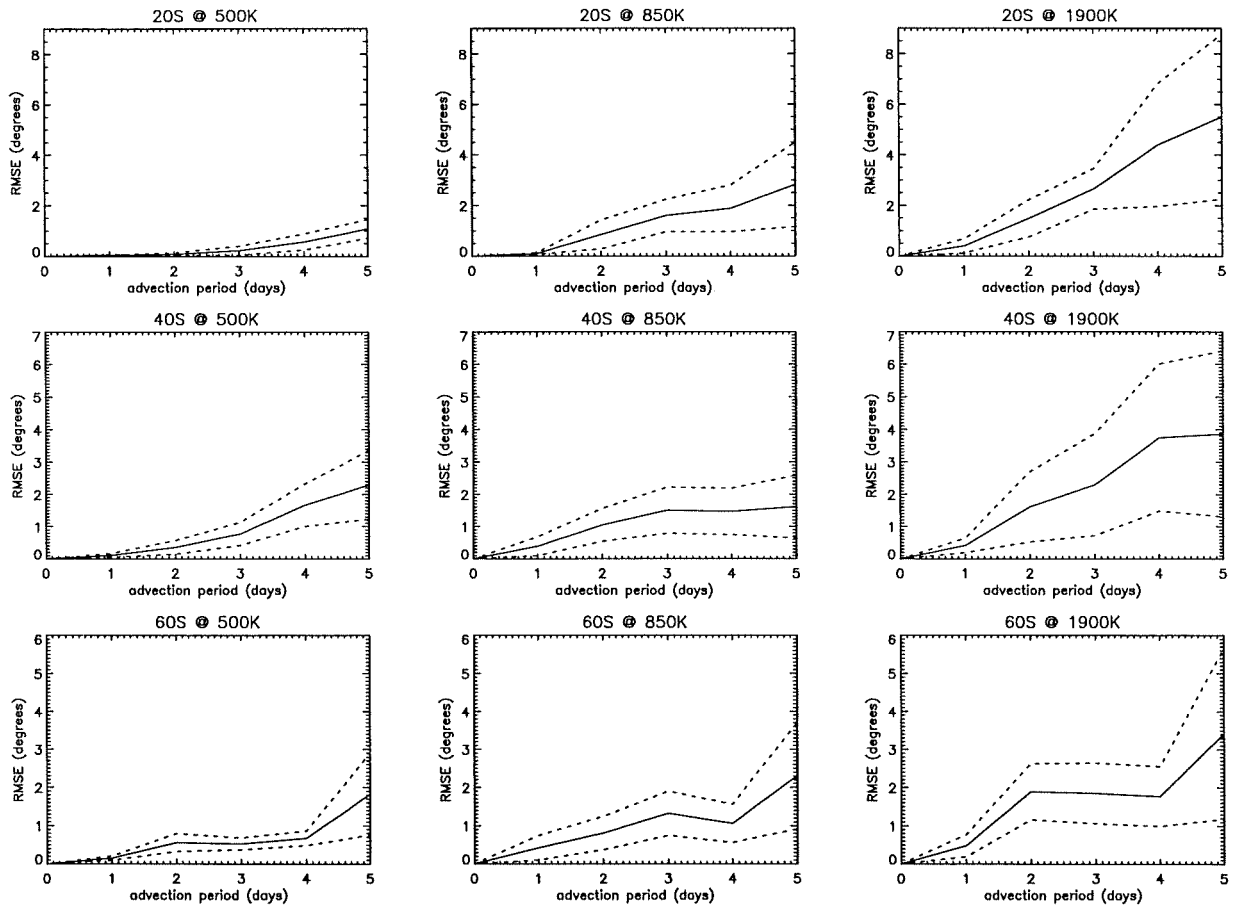

Fig 5.19. RMS differences between analysed and forecast meridional motion form the three latitude rings at the three different heights. The dotted lines represent one standard deviation error bounds.

Errors were smallest at 500K, the lowest level studied in the stratosphere, and grew with height. The mean RMS errors for advection on the 500K and 850K isentropic surfaces (~20km and 32km) were less than 3° and slightly larger on the 1900K surface (~48km), reaching ~5.5° ± 3° for advection from 20°S. Variability increased with increasing forecast period, again shown by the growing error bounds with advection period.

Of greatest relevance to this study is the performance of the forecast winds acting on the 60°S latitude ring at 500K (~20km). Ozone depletion is greatest at around this height in the polar vortex (generally poleward of 60°S) thus motion from here will have to be predicted

accurately for the accurate forecast of filaments. The mean RMSE from 60°S at 500K (~20km) was ~0.15° ±0.05° after one day, ~0.7° ±0.2° after four days, with less accuracy after five days. Forecast northward motion (corresponding to away from the vortex) was larger than analysed motion which would lead to a forecast overestimating the amount of polar air reaching mid-latitudes for example.

An important point to note for analysis made in this section is the origins of the air in a tongue such as that depicted in figure 5.16. While it is entirely correct to state that the air was confined to the region poleward of 60°S before being advected, it did not necessarily originate from inside the vortex. Consider figure 5.17 which showed the geopotential field relevant to the advection of the rings in figure 5.16. On this occasion, as is normally the case, the vortex is not symmetrically centred exactly on the pole but is off to one side, towards South America (upper left) on this day. The view is a polar stereographic projection with the South Pole in the centre thus making the equator at the outer circumference of the plot. The two inner dotted lines represent the latitude circles at 60°S and 30°S. Inspection of the 60°S latitude circle shows that the part of the ring closest to Australia (lower right) is outside the vortex. Advection of the ring will therefore see that region air stripped away from the polar vortex, by winds approximately following the contours in the geopotential plot, and subsequently transported over New Zealand as in figure 5.16.

While results in this section are valid they will not accurately represent the amount of motion out of the polar vortex. To make measurements such as these concerning vortex air requires a contour advection scheme to be used. Implication would see a contour at the edge of the vortex extracted, labelled and advected by the wind field thus accurately showing exactly where a mass of ozone-depleted air for example would travel. The biggest problem with advection schemes is the gaps that tend to develop in the contours (evident in figure 5.16). The main reason gaps will develop is that the length of a circular contour for example will increase as a filament forms and is drawn off it. This can be overcome however by employing a Contour Advection Scheme with Surgery such as that described by *Waugh et al. (1994)*. The basic method sees the addition of parcels as small-scale structure develops with the placement dependant on prescribed parameters, such as the curvature of the contour, thus maintaining the resolution of the contour. The surgery part of the algorithm involves the removable of very fine structure below some cut-off scale thus shortening thin filaments and allowing identical contours to merge or break apart. This then permits the examination of tracer transport on scales smaller than those achieved through the meteorological assimilation analyses.

The work in this thesis does not employ a contour advection scheme but uses a different technique for obtaining high resolution fields to allow the study of fine structure, namely Back Trajectory Mapping.

5.9 Filaments via Back Trajectory Mapping

We now employ the back trajectory scheme outlined in chapter three to generate high-resolution potential vorticity fields on an isentropic surface. A time of five days was chosen for parcel trajectories as *Sutton et al. (1994)* argued that five days would permit sufficient small-scale structure (i.e. filaments) to develop without excessive error growth. Furthermore in the case of the forecast wind files, only five fields were available which, when combined with the initial analysed field, only allows trajectories over five days to be computed.

A filament that has originated from the polar vortex in the SH will appear as a finger of air with a larger negative value of potential vorticity overlying smaller background values at mid-latitudes (since potential vorticity increases negatively towards the pole in the Southern Hemisphere). Figure 5.20 presents one such example, in which a filament extends across Christchurch, New Zealand. The plot comes from a high-resolution map of IPV on the 490K isentropic surface for 13 October 1994, and is a profile down the 173°E meridian. The filament can be seen at 42.5°S. In this case the back-trajectory code was used solely with analysed winds.

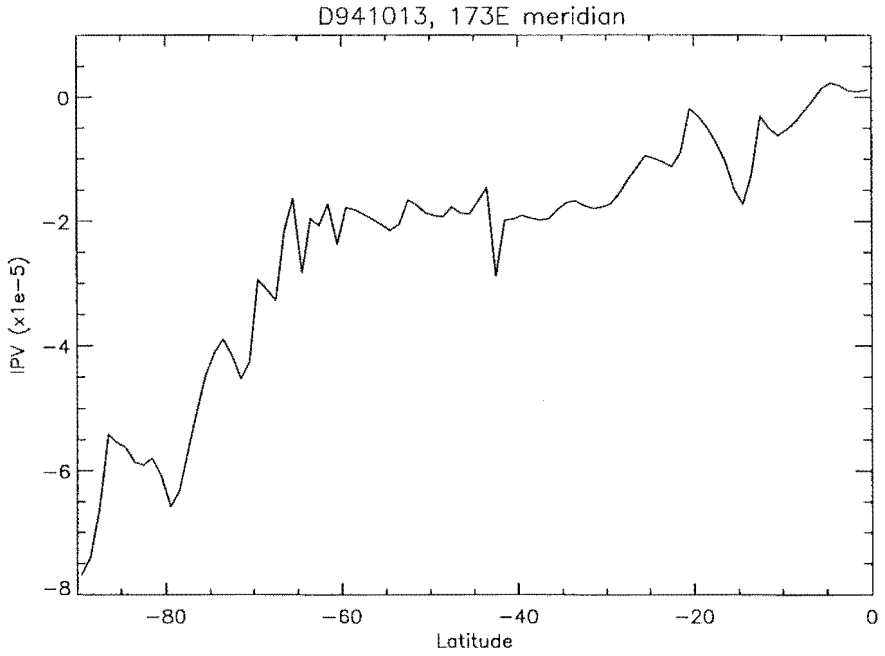

Fig 5.20. Southern Hemisphere IPV profile down the 173°E meridian at 490K for 13 October 1994. Note the filament at 42.5°S.

As can be seen above, the approximate background value for IPV through the mid-latitudes is roughly -2×10^{-5}, with the filament reaching roughly -3×10^{-5}. An important consideration for the prediction of such a filament is the size of the errors at that latitude, arising from the substitution of analysed winds for forecast winds. To obtain some measure of these errors, two different forecast fields of high-resolution IPV were compared with the analysed field on for the above case of 13 October 1994. In one case the configuration of the wind file was five analysed fields followed by one- and two-day forecast fields (5a/2f), while the second case had three analysed fields followed by four forecast fields (3a/4f). Note that seven fields (at 1200UTC) are necessary for five days of back trajectories starting and finishing at midnight. The high-resolution IPV fields from the forecast winds were then compared to the high-resolution field from analysed winds and zonal mean RMS errors then computed. The results are shown in figure 5.21.

As can be expected, larger errors resulted from using more forecast wind fields. Note that the RMS errors at the location of the filament at 42.5°S are roughly 0.25×10^{-5} and 0.4×10^{-5} for the wind file configurations of 5a/2f and 3a/4f respectively. In both cases the errors are much smaller than the total change in IPV for the filament ($\sim1\times10^{-5}$). This shows that a filament of this magnitude at this latitude should be easily resolved in a high-resolution map from forecast wind fields and not lost in the errors in moving from analysed winds to forecast

winds. Note however that this does not allow for any errors in generating the PV fields in the first place.

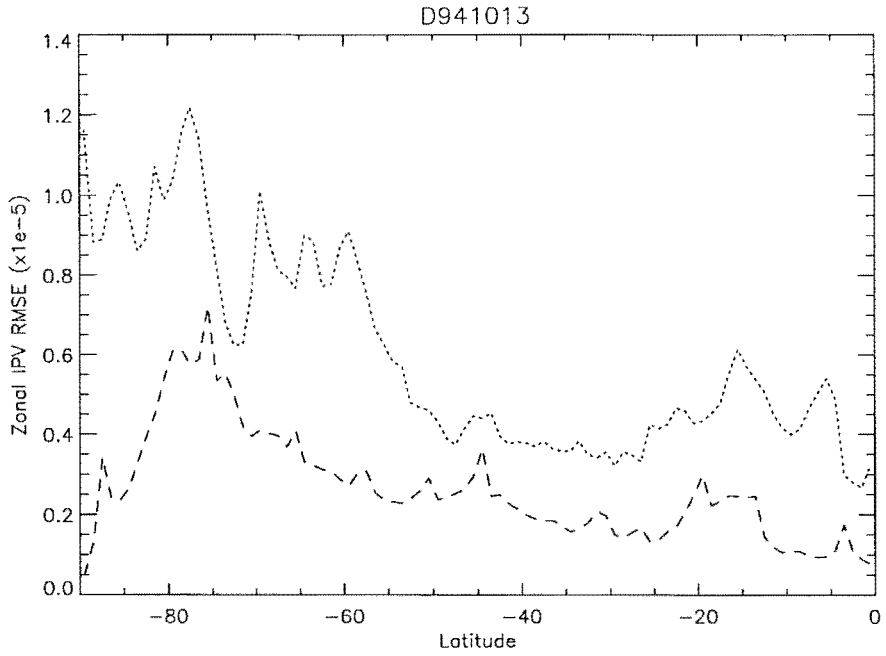

Fig 5.21. Zonally averaged RMS errors for IPV at 490K on 13 October 1994. Dashed line is for the 5a/2f wind fields while the dotted is for the 3a/4f wind fields.

Figure 5.22 shows the analysed profile again, along with the profile from the 5a/2f fields. Note how well the forecast profile matches the analysed profile from mid-latitudes to the pole including the filament. In this case the largest differences are in the region 30°S-10°S although the same structure is produced from forecast winds only further northward.

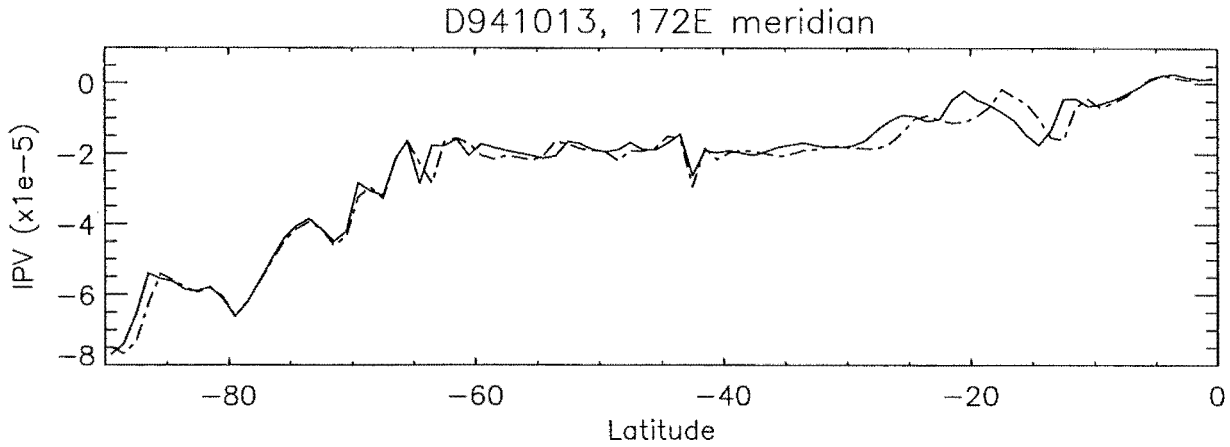

Fig 5.22. IPV profiles down the 172E meridian at 490K for 13 October 1994. Solid is from analysed wind fields and dash-dot from 5a/2f wind fields.

To highlight the performance of the forecast winds compared to the analysed winds figures 5.23(a) and (b) show the entire high-resolution IPV field at 480K on 30 July 1994 generated from analysed wind fields and 2a/5f wind fields respectively.

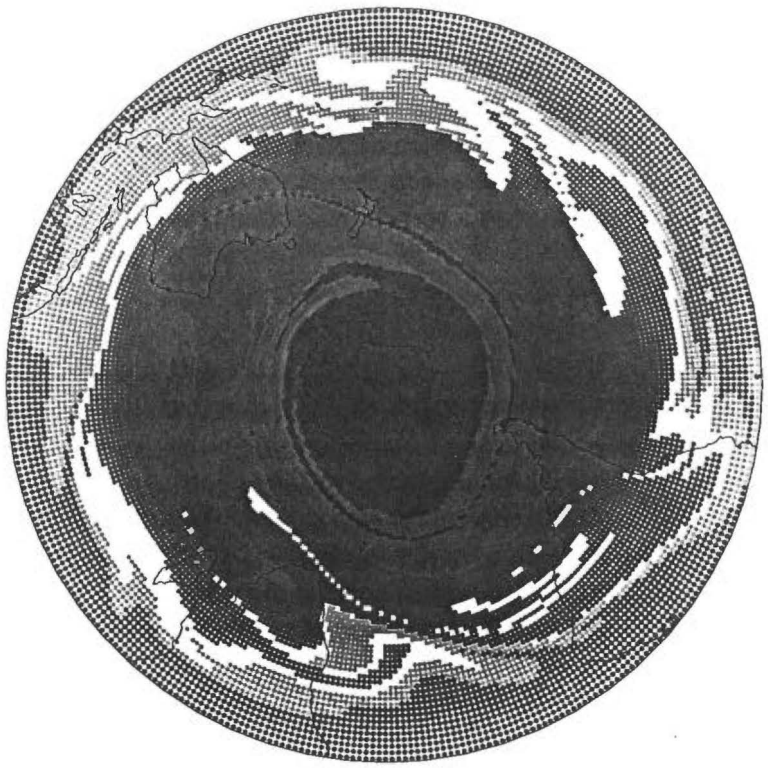

Fig 5.23(a). High-resolution IPV field from analysed wind fields at 480K on 30 July 1994.

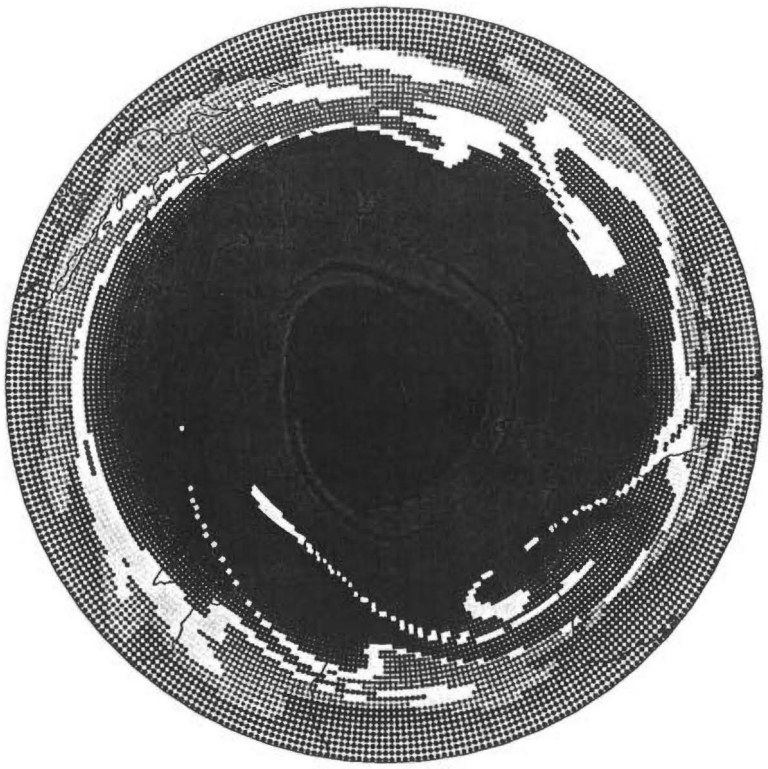

Fig 5.23(b). High-resolution IPV field from 2a/5f wind fields at 480K on 30 July 1994. Note how close the overall structure is to 5.25(a).

Given the fields in figures 5.23(a) and (b), it is clear that the forecast winds are generally very good at producing the same structure as the analysed winds. It should be noted that statistical tests of accuracy for two fields such as these are rather difficult to do sensibly. For example, a thin filament may be forecast with the exact same structure as that given by the analysed wind fields but have a slightly different location. In that case large errors will creep into the statistical analysis thus casting a shadow on the more important result, that being, the presence of the filament in the first place.

5.10 Comparisons with Aircraft Measurements

This final section of the results chapter takes the high-resolution IPV maps and compares them with measurements made by the aircraft during the ASHOE/MAESA campaign in 1994. The purpose of such comparisons is to try and determine whether the structure gained during the back trajectory code is an accurate prediction of the atmosphere and able to be measured independently. To achieve this, flight data is interpolated onto a high-resolution map of IPV and compared with the N_2O data gathered by the aircraft. N_2O, like PV, is approximately conserved in the stratosphere for air parcel motion thus can be used as a tracer of atmospheric motion over a few days.

Comparisons such as these were made by *Fairlie et al. (1997).* Note that references to reverse-domain-filling techniques in their study are the same as the back-trajectory mapping techniques used in this thesis, just under a different name. They used four different sources for meteorological data, namely, (1) U.K. Meteorological Office (UKMO) operational analyses (UO), (2) European Centre for Medium Range Weather Forecasts (ECMWF) operational analyses (EC), (3) the Australian Bureau of Meteorology (ABOM) Global Assimilation and Prediction Scheme (GASP) analyses (GA) and (4) the NASA Goddard Space Flight Center (GSFC) Earth Observing System (GEOS) analyses (GE). The study carried out focused on comparisons of analysed PV and Reverse-Domain-Filled (RDF) PV with Nitrous Oxide with a view to "quantify the level of predictive skill for analysed and RDF PV in accounting for nitrous oxide (N_2O) tracer structure encountered during 20 flights of the ASHOE/MAESA campaign" [*Fairlie et al. (1997)*]. A least squares linear fit was applied to scatterplots of PV vs. N_2O to construct "predicted" N_2O profiles from the PV data following which statistical tests were used to examine the skill of the analysed/RDF PV at predicting the aircraft measured N_2O profiles. The findings of the three statistical tests that were conducted are summarised below.

The first test involved calculating cross-correlation coefficients between five-minute-averaged N_2O profiles and N_2O predictions from analysed/RDF PV. A higher cross-correlation coefficient for RDF PV over analysed PV shows a higher relative forecast skill. Of the 20 flights studied by *Fairlie et al. (1997)*, RDF N_2O predictions were more successful on 10 out of 20 flights for UO, 7/20 for EC and 9/20 for GA and GE. The mean cross-correlation coefficients and their standard deviations (for all 20 flights) for analysed and RDF PV predictions of the N_2O profiles are shown in table 5.1.

	EC	GA	GE	UO
Analysed	0.73(0.19)	0.69(0.15)	0.71(0.22)	0.78(0.15)
RDF	0.71(0.22)	0.61(0.23)	0.71(0.17)	0.75(0.21)

Table 5.1. Mean cross-correlation coefficients and their standard deviations for analysed and RDF PV/N_2O predictions of 5-min-averaged N_2O Data for each centre. [from Fairlie et al. (1997)]

Consistent with the forecast quality as measured from the cross-correlation coefficients was that determined from the RMS differences between the analysed/RDF PV and the ATLAS N_2O data. RMS differences were smaller for RDF PV compared to analysed PV for 10/20 flights for UO, 7/20 for EC and 9/20 for GA and GE. The mean RMS differences and their standard deviations (again for all 20 flights) for analysed and RDF PV predictions of the N_2O profiles are presented in table 5.2.

	EC	GA	GE	UO
Analysed	14.3(3.3)	16.1(4.4)	14.7(4.3)	13.1(3.3)
RDF	14.9(4.2)	17.1(5.7)	15.3(4.6)	13.5(3.6)

Table 5.2. Mean RMS differences and their standard deviations for analysed and RDF PV/N_2O predictions of 5-min-averaged N_2O Data for each centre. [from Fairlie et al. (1997)]

Like the cross-correlation coefficients above, the RMS differences suggest that N_2O predictions from RDF PV have less predictive skill than those from analysed PV since values for analysed and RDF comparisons for each centre fall within the one standard deviation error bounds as listed in the previous tables. This would suggest that there is no significant gain in forecast quality by using the RDF PV instead of the analysed PV.

As noted in the previous section and by *Fairlie et al. (1997)*, errors in the location of sharp gradients or filaments have a large effect on the statistical analysis of the skill of a forecast. For example, cross-correlation coefficients will decrease while the RMS differences will increase with the incorrect location of a filament. To overcome this problem, *Fairlie et al. (1997)* used the Kolmogorov-Smirnov (KS) test [*Gibbons (1985)*] to quantify the agreement between the overall characteristics of the observed and predicted N_2O frequency distributions for each flight. This test is similar to the chi-square test except that the maximum difference between the cumulative frequency distributions is the statistic used as a measure of agreement between the frequency distributions which are less sensitive to different gradient or filament locations (in the chi-square test the statistic used is just the maximum difference between the frequency distributions). KS significance levels give a quantitative measure of the agreement of the two frequency distributions. "A KS significance level of 0.95, indicates a 95% probability that the two distributions are identical" [*Fairlie et al. (1997)*]. Results of the KS significance level tests of *Fairlie et al. (1997)* are presented in table 5.3.

	EC	GA	GE	UO
Analysed	0.32(0.27)	0.26(0.27)	0.31(0.29)	0.43(0.30)
RDF	0.30(0.26)	0.19(0.25)	0.28(0.23)	0.38(0.26)

Table 5.3. Mean KS significance levels and their standard deviations for analysed and RDF PV/N_2O predictions of 5-min-averaged N_2O Data for each centre. [from Fairlie et al. (1997)]

Again the results indicate less skill for predicted N_2O profiles from RDF PV as opposed to analysed PV although all differences for each centre are small and values lie within the one standard deviation error bounds. As for the individual flights, 6/20 had higher KS significance levels for the RDF PV predicted N_2O profiles for data from UO and GA with 8/20 for EC and GE.

In this study, similar comparisons were made but with a more qualitative approach. Here measured N_2O profiles are compared to high-resolution IPV profiles generated using both analysed winds and varying periods of forecast winds.

Implementation of this part of the analysis requires the back-trajectory code to be run with midnight initialisation for comparisons between high-resolution maps and aircraft data due to flight times and model field times. The maps are generated on one isentropic surface thus it is necessary to pick the surface that best approximates the aircraft's altitude. Outbound and inbound tracks were treated independently thus allowing two different approximating surfaces to be used if necessary. Figure 3.2 gave an example of the flight on 28 July 1994 with time plots of the location parameters – latitude, longitude, height and potential temperature. The closest approximating surface for each track was chosen from a time plot of potential temperature such as 3.2(d), in this case the 450K isentropic surface was used for both legs of the flight. The latitude-longitude values of the aircraft's course were then used to extract an along-track profile of IPV from the high-resolution map, whose structure is then compared to the aircraft measured N_2O. In the absence of N_2O data a CH_4 profile was used instead, since the volume mixing ratios for N_2O and CH_4 are correlated thus will show the same structure despite the numerical values being quite different.

The availability of UKMO fields only permitted seven different flights to be studied with five south of New Zealand and two to the north (they were, south: 28 and 30 July, 13, 16 and 20 October, and north: 1 August and 22 October). Each of the northward flights had only a single leg for study as on one occasion there was a second dive period in the return leg (thus it was discarded) and the other one was a transit flight to Nadi, Fiji. All flights south of New Zealand had two legs for comparison. In the case of forecast PV profiles, 10 comparisons were made with aircraft measurements as three of the flights had two different forecast profiles available (from differing forecast periods).

Results showed that in general, large-scale structure is predicted reasonably well by the high-resolution PV fields from the back-trajectory code. This is illustrated in figures 5.24 and 5.25 with comparisons of analysed PV with that from 4a/3f wind fields for both cases. Figure 5.24 shows the northbound leg of the flight south of New Zealand on 28 July 1994 with comparisons of PV on the 450K isentropic surface with CH_4 (on this occasion the N_2O dataset was incomplete). Figure 5.25 is the northbound leg of the flight north of New Zealand on 1 August 1994 with a comparison on the 470K surface of PV and N_2O.

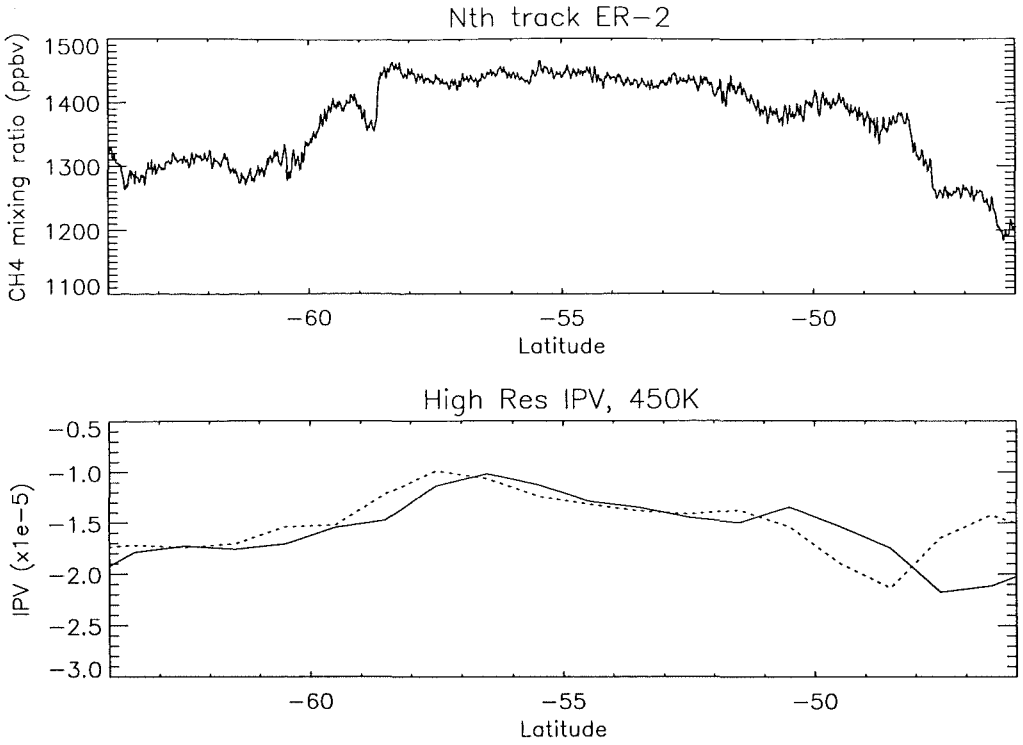

Fig 5.24(a) and (b). (a) CH_4 profile for the flight on 28 July 1994 with the high-resolution PV profiles for comparison (b). Profile from analysed wind fields (solid) and 4a/3f wind fields (dotted).

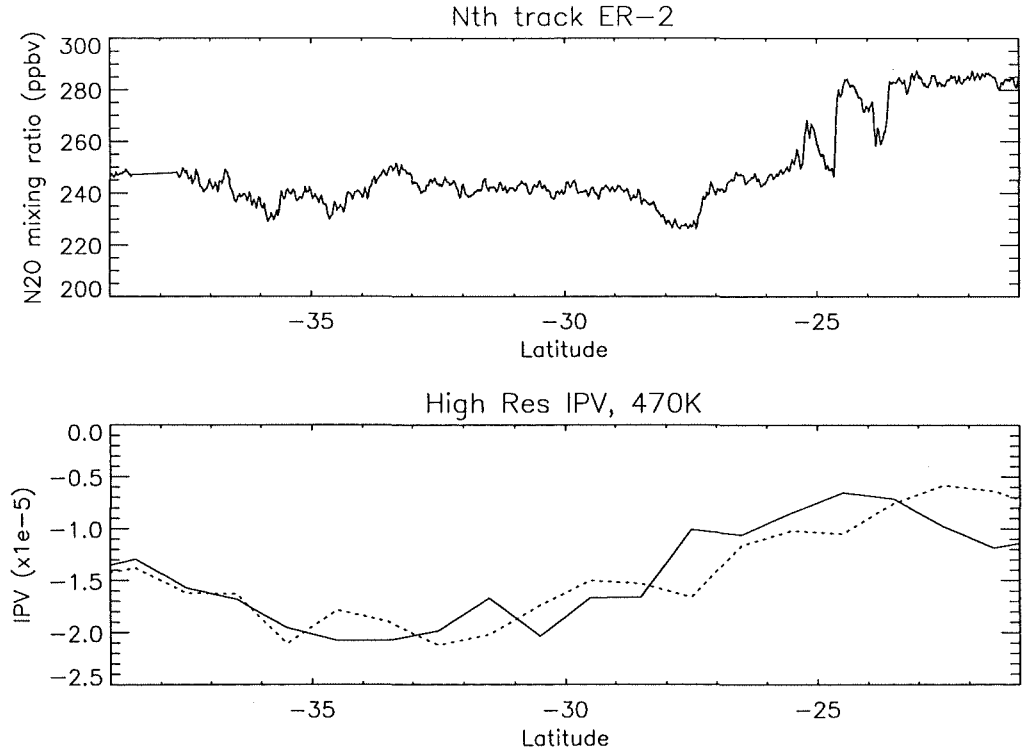

Fig 5.25(a) and (b). (a) N_2O profile for the flight on 1 August 1994 with the high-resolution PV profiles for comparison (b). Profile from analysed wind fields (solid) and 4a/3f wind fields (dotted).

Both cases show reasonable approximation of the PV profiles to the larger scale structure in the aircraft measured profiles. Figure 5.24 shows a close approximation between the analysed PV and measured CH_4 as does the forecast PV poleward of 50°S with less success north of this latitude. In the case of figure 5.25 the forecast PV seems to produce a better approximation than the analysed PV especially at lower latitudes.

Two further examples are given in figures 5.26 and 5.27, both for the southward legs of the flights south of New Zealand on 16 and 20 October 1994 respectively. For each of these cases, two different configurations of forecast wind files were available from the data and as expected the profile for the file with the lesser number of forecast fields gave the closest prediction of the profile from analysed winds only.

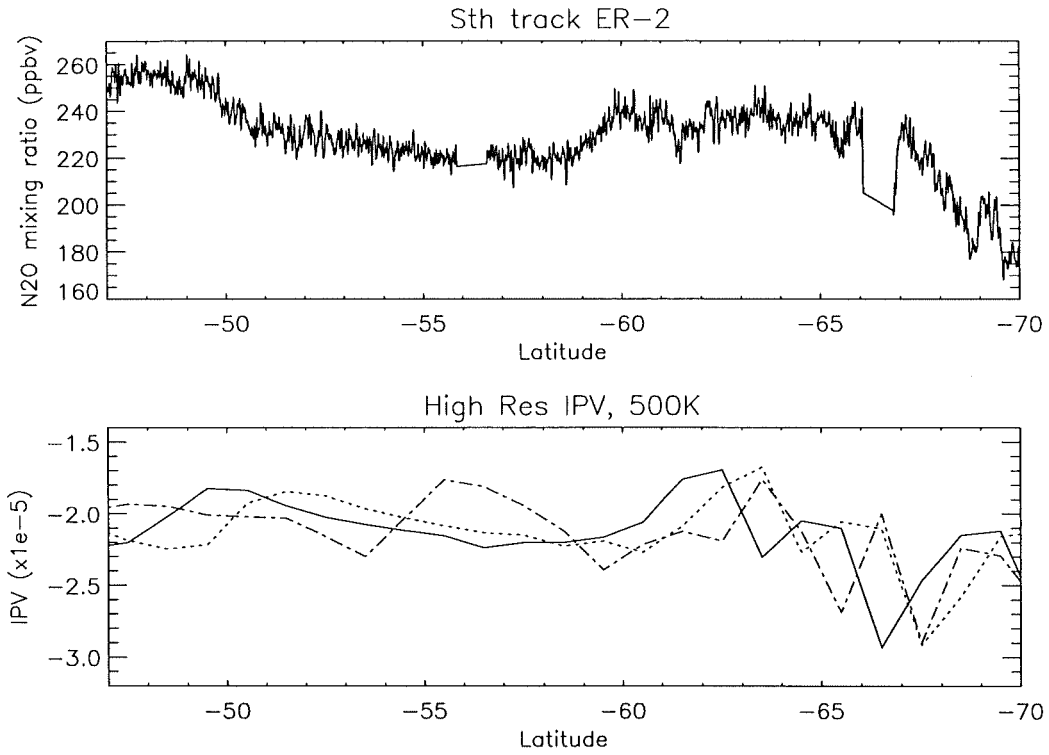

Fig 5.26(a) and (b). (a) N_2O profile for the flight on 16 October 1994 with the high-resolution PV profiles for comparison (b). Profile from analysed wind fields (solid), 5a/2f wind fields (dotted) and 2a/5f wind fields (dot-dash).

As can be seen in figure 5.26, the profile with two forecast fields exhibits the same structure as the analysed profile but displaced by roughly one degree toward the pole. This figure serves as an excellent demonstration of why care must be used when applying statistics to such comparisons. Here RMS errors between the profiles would be large despite the fact that each exhibits the same structure. The case with five forecast wind fields does less well particularly between 50°S and 60°S.

This southward displacement of the forecast profile was present on a few occasions and most apparent in figure 5.26 and also in figure 5.24 previously. The most likely explanation for the displacement of the seemingly correct structure between the analysed and forecast profiles is errors in the zonal winds. Filaments originating from the vortex tend to spiral off from east to west as seen in figure 5.23. Once a filament has formed (a result of the meridional winds), its longitudinal position will be determined by the zonal wind. As shown in figure 5.7(a), wind speed was often over-predicted inside the vortex and under-predicted outside as a result of

forecasting the position of the polar jet incorrectly. The weaker forecast winds outside the vortex would lead to the forecast filament lying to the west of the analysed filament thus producing the displacement in figure 5.26(b) when taking a profile down a meridian.

A further point to note in the above profile is the beginning and end of a large dip in the N_2O data between 66°S and 67°S. The near horizontal part of the profile there indicates a lack of data from the instrument thus it is unclear exactly how deep the dip would be. The analysed PV profile has a similar dip at the same location with both forecast profiles also having a dip but around a degree further south.

The flight on 20 October 1994 (figure 5.27) demonstrates again that the best prediction of the analysed PV profile comes from the file with the lesser number of forecast fields, in this case the 4a/3f file.

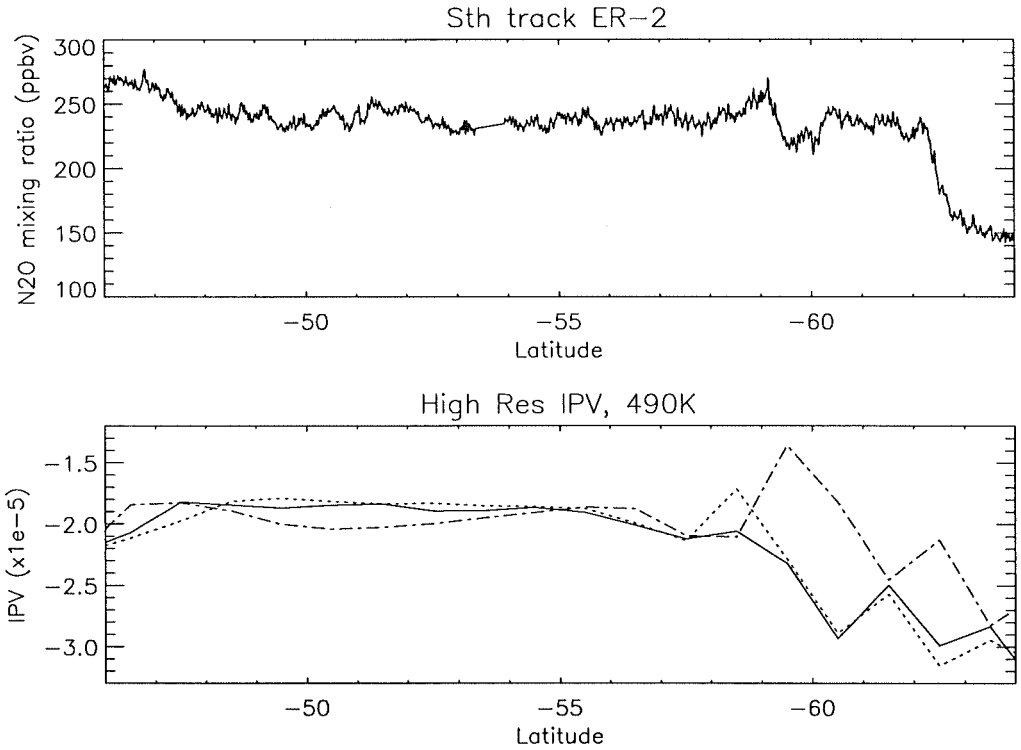

Fig 5.27(a) and (b). (a) N_2O profile for the flight on 20 October 1994 with the high-resolution PV profiles for comparison (b). Profile from analysed wind fields (solid), 4a/3f wind fields (dotted) and 2a/5f wind fields (dot-dash).

Regrettably one of the best cases of a filament encountered by the aircraft (10 October 1994) did not have enough UKMO fields available to utilise the back-trajectory code. On that occasion the N_2O mixing ratio dropped from around 240ppbv early on the southbound leg to around 160ppbv before recovering again. A similar filament was also observed on the return northbound leg. *Fairlie et al. (1997)* did however study this and concluded, "None of the predicted profiles based on analyzed PV capture a filament in the location observed by the aircraft, although the UO and EC profiles show a dip in approximately the same location... RDF profiles for UO and EC show a filament... somewhat displaced from that encountered by the ER-2."

There are many potential sources of error in back-trajectory calculations such as these. *Morris et. al (1994)* concluded that errors in the advecting winds will dominate due to the

neglect of diabatic effects but that these errors will remain small for studies under one week. Most obviously this will cause parcels to follow inaccurate trajectories resulting in incorrect labelling of PV at the initial time. Secondly, wind-field errors will also cause error in the calculation of potential vorticity which is used to label the air parcels (since PV is derived from winds). Other errors include numerical errors in the trajectory calculations themselves and errors in other quantities contributing to PV errors. For example temperature field errors may lead to incorrect calculation of potential temperature thus giving errors in the position of isentropic surfaces onto which the advecting winds are interpolated resulting in PV errors.

As shown by figures 5.23(a) and (b) previously, back-trajectory code applied to files containing forecast wind fields did produce surprisingly accurate high-resolution PV fields even for forecast winds out to five days. Multiple measurements of a filamentary event such as that in figure 5.23 would certainly have provided valuable information on the predictive skill of the high-resolution PV fields.

Chapter 6

Summary and Conclusions

This final chapter summarises the work of the thesis before moving on to concluding remarks, recommendations for future work and acknowledgements.

6.1 Summary

6.1.1 Period Studied

Initial analysis concentrated on October 1994 when the Antarctic vortex was well established before its final break-up in late spring. Furthermore, data was available during that period from aircraft measurements during ASHOE/MAESA along with model fields from the UKMO assimilation scheme. Later analysis was also performed for a period in February 1995 during the Southern Hemisphere summer to compare with the winter results.

6.1.2 Model Forecast Performance

Simple Eulerian comparisons between analysis and forecast fields were carried out to determine the relative size and location of any systematic errors particularly in the temperature and wind fields.

During October 1994 the minimum temperature in the vortex was forecast too cold in 22 of the 30 comparisons that were made. Absolute differences were no more than 3K with the RMSE at five days equalling 1.66K ± 0.85K (one standard deviation). Any bias in the minimum temperature for the vortex could have a large effect on chemical processing in models of stratospheric chemistry. Given the small bias found in this study, a model based on UKMO fields might over-estimate the amount of PSC's forming in the colder vortex, thus allowing increased chemical processing via the heterogeneous surface reactions and hence over-estimation of the amount of ozone depletion.

Consistent with minimum temperatures being too cold were the results from the maximum wind comparisons. Colder temperatures imply a more intense vortex with stronger winds. The maximum zonal wind strength during the October 1994 was over-predicted on 17 of the 30 comparisons made. Absolute differences here were not larger than 7m/s with the RMSE at five days equalling 4.9m/s ± 1.6m/s (one standard deviation). Despite the small bias found in this study, the implication is to over-predict the strength of the vortex and hence the gradients in PV thus permitting less mixing across the vortex boundary. A possible cause for this over-estimation of the strength of the polar jet is the lack of a good gravity-wave drag parameterisation scheme in the model as concluded by *Carver et al. (1994)* in their study of the UGCM. *Garcia et al. (1994)* also studied the effects of gravity waves and concluded "the omission of gravity-wave drag in the mesosphere could be the cause of the cold bias in GCM simulations of the polar winter stratosphere, particularly in the Southern Hemisphere".

Field differences of isentropic potential vorticity on a potential temperature surface revealed a large +/- dipole associated with the gradients forming features at the edge of the vortex. The direction of the dipole indicated that those features were forecast too far eastward as was found by *Waugh et al. (1997)* in their study of the ABOM's GASP. They employed an elliptical diagnostic approach and found the ellipse fitted to the contours of the forecast vortex was orientated east of the ellipse fitted to the same contours of the analysed vortex.

Zonal-mean difference plots of temperature revealed the largest errors lie in the upper stratosphere near the stratopause. During October 1994 there were three main regions with systematic errors. The lower mesosphere near the North Pole was forecast too cool while a large +/- dipole was present either side of the stratopause near the South Pole indicating an error in the position of the stratopause. Temperatures were consistently too cool at around 40km and too warm around 50km suggesting that more descent at those heights is required in the model to bring the warm stratopause lower in the forecast temperature fields thus indicating that the diabatic circulation in the model forecast fields is incorrect. These findings support the results of Manney et al. (1995) who concluded that "diabatic descent rates are too weak almost everywhere in the SH" due to a "possible bias in the SH UKMO temperatures".

The zonal wind field differences showed that the largest errors were associated with the vortex throughout the stratosphere. Again large +/- dipoles were observed, this time either side of the polar jet indicating an error in the prediction of the location of the jet. Winds inside the polar jet were often over-predicted as highlighted by the maximum wind speed comparisons mentioned above.

To evaluate the general performance of the model forecast fields, RMS errors were calculated for different regions in the Southern Hemisphere and at different heights. The regions studied were 45°S-SP, 55°S-SP and 25°S-60°S while the three heights were 20km, 32km and 48km. Calculations were performed for temperature, zonal and meridional winds and geopotential. Errors for forecast fields were then compared with those for persistence fields as a measure of forecast skill. During October 1994 the smallest errors measured fell in the latitude annulus from 25°S-60°S at a height of 20km. At 48km there was often an entire overlap of the forecast and persistence error bounds showing our ability to forecast near the model lid is poor. The skill of the forecasts was best lower in the stratosphere, for example the forecast RMSE for temperature in the region 55°S-SP at five days was roughly 37% of persistence at 20km, 60% at 32km and 84% at 48km.

The same forecast performance analysis was applied to a series of five seven-day forecasts in February 1995 for comparison with the October measurements. The magnitude of the RMS errors were smaller for February, however an entire overlap of the error bounds often existed indicating no significant gain of forecast over persistence. In some cases the persistence RMS errors were actually smaller than those for the forecasts. Results such as these clearly demonstrate that the winter dynamically forced stratosphere is modelled more accurately than the summer stratosphere not containing the stable polar vortex.

6.1.3 Temperature: Model vs. Aircraft

As an independent check on the accuracy of the UKMO analysis and forecast temperature fields, comparisons were made between the model fields and measurements from the aircraft during the ASHOE/MAESA campaign. Flight data was interpolated into the UKMO fields to extract an along track temperature profile to compare with that measured by the instruments on the ER-2. Results showed a distinct bias in the analysis fields to under-predicting the

temperatures with a general increase in the RMS errors at latitudes higher than 65°S. Values for the RMS errors ranged typically from around 1.5K from 45°S-65°S and increased to around 4K on some occasions at 70°S. Comparisons of the forecast fields during October 1994 with the aircraft measurements showed more variation, with some cases having smaller RMS errors than the analysed fields. RMS errors again increased towards the pole at high latitudes for the forecast field comparisons.

Results also highlighted that the polar region in particular is too cool in the model fields compared with the real atmosphere (especially during October). Again this is most probably due to the lack of a good gravity-wave parameterisation scheme in the upper stratosphere and mesosphere [*Garcia et al. (1994)* and *Carver et al. (1994)*].

6.1.4 Lagrangian Motion

An advection scheme was used to investigate the differences between the analysis and forecast winds as applied to specialised parcel locations on an isentropic surface. The main focus was on the meridional component of the wind vector thus to obtain some measure of forecast performance three latitude rings at 20°S, 40°S and 60°S were advected for periods from one to five days at 500K, 850K and 1900K (approximately 20km, 32km and 48km respectively). The deviation from the starting latitude was then averaged for each of the 360 parcel locations around the latitude ring. Meridional motion was generally well predicted using forecast winds in place of analysed winds with an entire overlap of the one standard deviation error bounds for most cases with the only exceptions being from 20°S at 850K and 1900K for four and five-day advection. RMS errors between the forecast and analysed motion increased with both the advection period and height. For advection from the 60°S latitude ring at 500K the RMSE between forecasts and analyses during October 1994 was roughly 0.15° ± 0.05° after one day, 0.7° ± 0.2° after four days with less accuracy after five days.

6.1.5 Filamentary Structure

A back-trajectory mapping technique was employed to allow the visualisation and analysis of filamentary structure originating from the Southern Hemisphere polar vortex. Initial comparison of high-resolution fields generated from analysed and forecast wind fields indicated excellent qualitative agreement for the entire field even for filamentary structure derived from a five-day forecast.

The final piece of analysis saw along track profiles of IPV extracted from the high-resolution maps for comparison with aircraft measured tracer structure for several flights by the ER-2 during the ASHOE/MAESA campaign in 1994. It is difficult to perform statistical tests of comparison for two profiles as the same structure may be present but displaced in one profile leading to large RMS errors for example. Furthermore, due to the small number of comparisons made it would be difficult to draw any conclusions from such tests. To that end, comparison concentrated on a somewhat qualitative approach. The general large-scale structure in the measured profiles of N_2O was reasonably well represented in the high-resolution profiles of PV generated from both analysed and forecast winds. Several cases highlighted that structure in the IPV profile at high-latitudes was forecast south of similar structure in the analysed IPV profile. This was attributed to errors in the strength of the zonal wind such as those in figure 5.7(a) leading to a filament being forecast to the west of the analysed filament thus producing the above displacement of structure in a meridional slice.

None of the flights studied possessed any significant filamentary structure thus no conclusions can be drawn on the accuracy of the back-trajectory maps for this small-scale structure as measured by the aircraft. One of the best cases of a measured filament was studied by *Fairlie et al. (1997)* who found that a high-res. map of PV from UKMO analysed winds did show a filament although it was displaced somewhat from the measured one. They also performed several statistical tests to obtain a quantitative measure of the agreement between the aircraft measured and predicted N_2O profiles. They went on to conclude, "RDF PV showed no statistically significant improvement in forecast skill over analysed PV" and that "RDF predictions generally result in a degradation of forecast skill" [*Fairlie et al. (1997)*].

6.2 Conclusions

The aim of this thesis was to attempt to determine our ability to forecast the position of filaments of air originating from the polar vortex by studying the forecast performance of the UKMO assimilation system and the accuracy of the high-resolution PV maps that can be computed from the model output fields.

A detailed assessment of the stratospheric forecast fields from the UMKO assimilation system has been carried out for a period in October 1994 (SH winter). Conventional RMSE calculations were performed for three different regions in the stratosphere at three different heights for forecast and persistence fields. The same analysis was then applied to a period in February 1995 (SH summer) for comparison with the winter results. Supplementing these comparisons were studies of systematic errors in the temperature and wind fields along with the accuracy of the winds in an advection scheme on specialised parcel location fields. Results for the forecast performance assessment are in general agreement with similar studies by *Waugh et al. (1997)* and *Lahoz (1997)*. The advection of three latitude rings centred on the South Pole showed that forecast winds produce highly similar results for meridional motion to the analysed winds.

Qualitative comparisons of the structure in high-resolution maps of PV from a back-trajectory mapping technique were made with aircraft measured tracer structure from the ASHOE/MAESA campaign of 1994. Results here support the conclusion of *Fairlie et al. (1997)* that large-scale structure is well represented in the high-resolution PV fields, however no conclusive evidence could be obtained for filamentary structure.

It is important to note however that comparisons such as these are only one-dimensional leading to a significant lack of data to base conclusions on. The ideal situation would see simultaneous in-situ measurements of N_2O for example, made in two or even three dimensions – a somewhat impossible task in practice. Despite the apparent lack of skill of the high-resolution PV fields for along-track small-scale structure, it has been demonstrated that the complete hemisphere fields generated from both analysed and forecast winds are in very close agreement, even for filamentary structure at five days.

A back-trajectory mapping technique is a powerful tool to obtain global small-scale structure not achieved in lower-resolution model assimilation fields but is perhaps most useful for visualising atmospheric motions particularly associated with a winter polar vortex.

6.3 Recommendations for future work

The major limiting factor to conclusive evidence throughout this thesis was the relatively small number of comparisons made in any analysis due to the availability of data. For example, only six forecast files were available during October 1994. It would be useful to repeat the forecast performance assessment of the UKMO model presented here with a greater number of forecast data files (perhaps from a later version of the model) to be certain of the numerical results. Further forecast data would also allow several comparisons of the model-forecast fields with the aircraft measurements to be made for a larger number of flights during the ASHOE/MAESA campaign of 1994, following which meaningful results from statistical tests such as those used by *Fairlie et al. (1997)* could be computed. For this study, only two or three flights at most could be compared with the model-forecast assimilation fields for the same forecast period.

Application of the Elliptical Diagnostics method [*Waugh (1996)*] to the polar vortex during the SH winter of 1994 as forecast by the UKMO's assimilation scheme would certainly provide a valuable comparison to the results of *Waugh et al. (1997)* in their 'vortex oriented' analysis during the same period for the ABOM's GASP. It is a sensible and elegant approach when studying the polar vortex to fit an ellipse to a particular contour at the edge of the vortex thus allowing analysis to be carried out with ease. Parameters such as the area, orientation, centre and aspect ratio of the ellipse can be calculated quite simply and thus provide an exact definition of the location and size of the vortex.

Section 5.8 presented the results from a Lagrangian approach to study the accuracy of the forecast winds at predicting meridional motion. A useful extension to this section of the thesis would be employing a contour advection scheme such as that described by *Waugh et al. (1994)*. The scheme could be applied using both analysed and forecast wind fields to contours at the edge of the vortex to allow study of the evolution of the contour and any subsequent filaments that may be drawn off it. This would provide an alternative method for studying small-scale structure originating from the polar vortex to the back-trajectory mapping technique used in this thesis.

Finally, any further use of forecast high-resolution PV fields in the flight planning of aircraft campaigns into the lower stratosphere can only be beneficial to our knowledge on their potential for refining small scale structure not present in meteorological analyses.

6.4 Acknowledgements

I wish to thank firstly my supervisor Dr Bryan Lawrence. I am indebted to him for his guidance in the production of this thesis, the wealth of knowledge he shared with me on an understandable level and for solving my sometimes trivial computing problems.

Also to my other examiner Professor David Karoly for his useful suggestions and corrections for the finishing touches on this thesis.

Thanks must also go to my roommates over the past year. Dave Frame for answering a lot of questions and for the many discussions of politics, philosophy and of course sport, which made a pleasant break to the atmospheric work. Also to Adam Dunford and Doug Ferrier who joined us later in the year. There have been many useful discussions with others in the department, in particular Steve Marsh, Dave Galligan and Gareth Thomas along with the rest of the atmospheric group.

My parents have been a great inspiration and immense source of support throughout my University career. A big thank-you to Mum. I will miss her encouragement, love and the willingness to listen whenever I started burbling about physics and the sometimes difficult concepts involved. And to Dad for his guidance and continuing strength and support especially during the last few months of my thesis. Also to my sister Nicola, thank-you for providing a fresh face and a smile on your visits to our room for a chat.

Thanks to my girlfriend Brig and flatmates Thur and Jem for their friendship and the good times we had together. Finally to all my friends including; Boney, Roger, Eliza, Gordi, Grant, Deano, Rodge, Steph, Si, Al, G-man, Tina, Doogs, and Rovers for the golf, BBQ's and beers and for helping to maintain my sanity.

Appendix A

UKMO Data Information

A.1 UKMO Forecast Data Availability

Year	File Dates		No.	Timecode	cf.
	First	Last	Fields		No.
1994	2-Jan	6-Jan	5	D94002	1
	2-Feb	6-Feb	5	D94033	2
	29-May	2-Jun	10	H941490012	3
	24-Jul	28-Jul	5	D94205	4
	27-Jul	31-Jul	5	D94208	4
	31-Jul	4-Aug	5	D94212	4
	9-Oct	13-Oct	10	H942820012	5
	11-Oct	15-Oct	10	H942840012	5
	13-Oct	17-Oct	10	H942860012	5
	16-Oct	20-Oct	10	H942890012	5
	17-Oct	23-Oct	14	H942900012	5
	19-Oct	23-Oct	10	H942920012	5
	11-Dec	15-Dec	10	H943450012	6
	15-Dec	19-Dec	10	H943490012	6
	18-Dec	22-Dec	10	H943520012	6
	25-Dec	3-Jan	10	D94359	7
1995	8-Jan	12-Jan	10	H950080012	8
	15-Jan	19-Jan	5	D95015	9
	22-Jan	28-Jan	7	D95022	10
	29-Jan	4-Feb	7	D95029	10
	1-Feb	7-Feb	7	D95032	10
	5-Feb	11-Feb	7	D95036	10
	8-Feb	14-Feb	7	D95039	10
	13-Feb	19-Feb	7	D95044	10
	27-Feb	5-Mar	7	D95058	11
	16-Mar.	22-Mar	7	D95075	12
	21-Mar	27-Mar	7	D95080	12
	31-Mar	6-Apr	7	D95090	13

Table A.1. Shown above are the dates of available forecast files during 1994/95. Interpretation of the timecode is as follows: the 12-hourly code H941490012 has its first field at 0000UTC on day 149 in 1994 with the next field 12 hours later. Daily timecodes list only the year and day. Numbers in the far right column refer to the reference number of the appropriate analysis file for comparison.

A.2 UKMO Analysis Data Availability

Year	File Dates		No.	Timecode	Ref.
	First	Last	Fields		No.
1994	1-Jan	6-Jan	6	D94001	1
	1-Feb	6-Feb	6	D94032	2
	28-May	2-Jul	6	D94148	3
	23-Jul	4-Aug	13	D94204	4
	8-Oct	31-Oct	24	D94281	5
	10-Dec	22-Dec	13	D94344	6
	24-Dec	3-Jan	11	D94358	7
1995	7-Jan	12-Jan	6	D95007	8
	14-Jan	19-Jan	6	D95014	9
	21-Jan	19-Feb	30	D95021	10
	26-Feb	5-Mar	8	D95057	11
	15-Mar	27-Mar	13	D95074	12
	30-Mar	6-Apr	8	D95089	13

Table A.2. As for table A.1 except for the availability of analysis data.

A.3 Sample UKMO Data File Headers

```
--- INPUT FILE HEADERS ---
ASHOE_94100900_TPLUS12.PPOK
RICHARD SWINBANK FORECAST - FROM 12GMT 08/10/94
UKMO Assimilation via MAD UKAGRD V1.2 11-Oct-94 05:23:17
--------------------------


-- MADPO RECORD --------- [T  ] ----------- [MAD UKMO ASSV30A]
  TcodeID: H  Date: 1994 282    0     0  Nav:      1 Int:  12
  GridID:     1  VcoordID:   0   [120, 60, 24]   H:   6950.00
  Lat:  -88.5  3.0    Lon:    .0  3.0    Hgt: 10000.0  2000.0
------------------------------------------------------------

-- MADPO RECORD --------- [T  ] ----------- [MAD UKMO ASSV30A]
  TcodeID: H  Date: 1994 282 1200     0  Nav:      1 Int:  12
  GridID:     1  VcoordID:   0   [120, 60, 24]   H:   6950.00
  Lat:  -88.5  3.0    Lon:    .0  3.0    Hgt: 10000.0  2000.0
------------------------------------------------------------

-- MADPO RECORD --------- [T  ] ----------- [MAD UKMO ASSV30A]
  TcodeID: H  Date: 1994 283    0     0  Nav:      1 Int:  12
  GridID:     1  VcoordID:   0   [120, 60, 24]   H:   6950.00
  Lat:  -88.5  3.0    Lon:    .0  3.0    Hgt: 10000.0  2000.0
------------------------------------------------------------
...
```

Interpretation: The fields are 12 hourly temperature data with the first field for 0000hrs on day 282 (9 October) 1994. The grid has 120 longitude points from 0°, with 3° spacing and 60 latitude points from 88.5°S, also with 3° spacing. There are 24 vertical levels with the bottom at 10km spaced by 2km and the scale height is taken as 6950m.

THE LIBRARY
UNIVERSITY OF CANTERBURY
CHRISTCHURCH, N.Z.

Appendix B

ASHOE ER-2 Information

B.1 ASHOE/MAESA ER-2 Flight Information

Date (yymmdd)	Description	From	To	Aprx Dur'n (hrs)	Remarks
940121	TestFlt MASP/FCAS	Ames	Ames	2+	
940202	D&RTestFlt	Ames	Ames	2+	
940204	D&RTestFlt->59N	Ames	Ames	8	
940214	TestFlt	Ames	Ames	2+	wake enctr
940218	TestFlt->55N	Ames	Ames	8	ClO>240;vortex
940219	TestFlt	Ames	Ames	2+	wake enctr
940314	TestFlt MMS only	Ames	Ames	2+	
940318	TransitFlt	Ames	B Pt	5+	no dip
940320	FltSth->16N	B Pt	B Pt	2+	
940321	FltSth->2S	B Pt	B Pt	8	
940322	FltSth->6N	B Pt	B Pt	5	2 dips
940327	TransitFlt	B Pt	Nadi	7	no dip
940329	TransitFlt	Nadi	Chch	4+	T<-86C;1 dip
940330	FltSth->68S	Chch	Chch	8	
940403	FltNth->19S	Chch	Chch	8	
940405	FltSth->65S	Chch	Chch	8	
940408	FltSth->68S	Chch	Chch	8	
940413	D&RFltSth->68S	Chch	Chch	8	V/edge 52S
940415	D&RFltNth->38S	Chch	Chch	3	hydraulics
940523	FltSth->47S	Chch	Chch	3	
940524	FltSth->68S	Chch	Chch	8	
940528	FltNth->21S	Chch	Chch	8	
940601	FltSth->65S	Chch	Chch	8	bottomdip
940603	FltSth->67S	Chch	Chch	8	ClO climbout
940605	D&RFltSth->68S	Chch	Chch	8	no HIS
940608	D&RFltSth->45S	Chch	Chch	1	maxalt 47 kft
940728	FltSth->68S	Chch	Chch	8	PSC
940730	FltSth->68S	Chch	Chch	8	PSC
940801	FltNth->19S	Chch	Chch	8	2 dips
940806	FltSth->68S	Chch	Chch	8	O3 loss 67S
940808	D&RFltSth->69S	Chch	Chch	8	dehydr dip
940810	D&RFltSth->67S	Chch	Chch	8	
941003	D&RFltSth->68S	Chch	Chch	8	V/edge 53S
941005	D&RFltSth->65S	Chch	Chch	8	
941008	FltEofNZ	Chch	Chch	4	Concorde wake
941010	FltSth->70S	Chch	Chch	8	
941013	FltSth->69S	Chch	Chch	8	HCl=Cly in dip
941016	FltSth->70S	Chch	Chch	8	
941020	FltSth->64S	Chch	Chch	8	
941022	TransitFlt	Chch	Nadi	7+	dip at 10S
941024	TransitFlt	Nadi	B Pt	8	dip at 3S
941026	FltSth->2N	B Pt	B Pt	7	H2O layers in dip
941029	FltSth->2S	B Pt	B Pt	8	ditto
941102	TransitFlt	B Pt	Ames	6+	1 dip;headwind
941104	FltNth->59N	Ames	Ames	8	HCl/Cly < in SH

Table B.1 (previous page). Catalogue of all flights during ASHOE/MAESA 1994. [adapted from documentation on the *NASA ASHOE/MAESA CD-ROM*]

Approx. Positions:	Ames	(37°N,122°W)
	Barber's Point	(21°N,158°W)
	Nadi	(18°S,177°E)
	Christchurch	(44°S,173°E)

Total Hours:	289.4
Total Flights:	45
Test Flights:	7
Transit Flights:	6
Full Payload South from Chch:	14
Full Payload North from Chch:	3
D&R Payload South from Chch:	7
D&R Payload North from Chch:	1
Full Payload South from B Pt:	5
Full Payload North from Ames:	1
Full Payload Concorde Chase:	1

Table B.2. Supplementary flight information for ASHOE/MAESA 1994. [adapted from documentation on the *NASA ASHOE/MAESA CD-ROM*]

Figure B.1. ER-2 transit route from Ames, U.S.A. – Barber's Point, Hawaii – Nadi, Fiji – Christchurch, New Zealand.

B.2 Brief ER-2 Instrument Description

The following descriptions are adapted from the ASHOE/MAESA project handbook on the *NASA ASHOE/MAESA CD-ROM.*

ACATS IV	Four-Channel Airborne Chromatograph for Atmospheric Trace Species. Measures a variety of chlorine and long-lived species, including various CFC's.
ALIAS	Aircraft Laser Infrared Absorption Spectrometer. A high resolution tunable diode laser spectrometer measures NO_2, HCl, CH_4 and N_2O.
APS	Ames Particle Sampler Impactor Experiment. Particles are collected on palladium or gold wires. Their size, shape and chemical composition are identified in scanning transmission electron microscopes interfaced with x-ray energy dispersive analyzers.
ATLAS	Airborne Tunable Laser Absorption Spectrometer. An active target gas is detected by measuring the infrared absorption from a tunable diode laser.
ClO/BrO	Multiple Axis Resonance Fluorescence Chemical Conversion Detector for ClO and BrO. UV radiation is used to induce resonance scattering of Cl and Br (after conversion from ClO and BrO by addition of NO).
CNC	Two-Channel Condensation Nucleus Counter. The first measures particles 0.07-1μm diameter, and the second, the same size particles after airstream heated to ~200°C. Also, MACS, the Multi-Sample Aerosol Collection System, measures particles >0.01-0.03μm diameter.
CO_2	High-Sensitivity Fast-Response CO_2 Analyzer. CO_2 concentrations determined from a non-dispersive infrared analyzer.
CPFM	Composition and Photodissociative Flux Measurement. Intensities of two linear polarization components of radiation near the horizon are measured as well as the intensity of the direct solar beam.
HO_x	High-Altitude OH Experiment. OH detected by direct laser-induced fluorescence.
MASP	Multiple-Angle Aerosol Spectrometer Probe. Size and concentration of particles from 0.2-20μm with index of refraction for selected sizes.
MMS	ER-2 Meteorological Measurement System. System consists of an air motion sensing system, an inertial navigation system and the data acquisition system. Data consists of pressure, temperature, potential temperature, wind vector, aircraft position, pitch, roll, heading, angle of attack, angle of sideslip, true airspeed, eastward/northward velocity and vertical acceleration.
MTP	Microwave Temperature Profiler. The thermal emission from oxygen molecules for a selection of elevation angles is measured by a passive microwave radiometer.
NOAA Ozone	Dual-Beam UV-Absorption Ozone Photometer. Ozone number density is calculated from the absorption of light from a mercury lamp.
NO/NO_y	Reactive Nitrogen. Measures nitric oxide and the sum of reactive nitric oxides. NO from detecting light from the chemiluminescent reaction between reagent ozone and NO in the ambient sample.
Water Vapour	Lyman α Hygrometer. H_2O mixing ratio is measured from the fluorescence of excited hydroxyl radicals dissociated from a fraction of the water by a short-wavelength light source.

B.3 Sample ASHOE/MAESA Data Files

These sample file header and data extracts are from the data files on the *NASA ASHOE/MAESA CD-ROM.*

B.3.1 Sample Aircraft Flight Data File

```
27 1001                                                ;header lines/format index
CHAN, Roland
NASA - Ames Research Center
Aircraft Flight Data from ER-2's MMS
ASHOE/MAESA
1 1
1994 07 28   1994 07 30                                ;flight-date    process-date
0                                                      ;0=non-uniform time increment
Elapsed UT seconds of flight date
4                                                      ;number of primary variables
1.0   0.001  0.001   0.1                               ;scale factors
99999 999999 9999999 9999                              ;missing values
Pressure Altitude (feet)
Latitude +N (deg)
Longitude +E (deg)
True Air Speed (m/s)
1
PRELIMINARY DATA
8
Using Po1 sn #1564, Wang calibrated June 1994
Configuration: LTN-92 + GPS + OH nose + Back_Up Tf sensor & Amplifier
1Hz data are desampled from 5Hz data.
5Hz data file is available upon request, containing: GMTS,Psta,Tsta,TAS,
U,V,W,LAT,LONG,PALT,POT,ROLL,HDG,PIT,Ydot,Xdot,Zdot,Q,YAW,AOA,MACH,Zdotdot,
YAWdp,AOAdp                              (approx. 3 Mbyte per flight hour)
h:\mms\e_940728.cv
 UT        P_ALT LAT    LONG    TAS
...
 86395.3 65227 -67922  172354 1974
 86400.3 65226 -67923  172336 1973
 86405.3 65224 -67924  172318 1974
 86410.3 65226 -67923  172299 1972
 86415.3 65222 -67916  172281 1973
 86420.3 65225 -67914  172263 1973
 86425.3 65229 -67917  172246 1973
 86430.3 65218 -67913  172230 1974
 86435.3 65215 -67903  172215 1973
 86440.3 65204 -67898  172201 1972
 86445.3 65200 -67893  172188 1972
 86450.3 65199 -67886  172177 1974
 86455.3 65196 -67885  172167 1973
 86460.3 65197 -67878  172159 1973
 86465.3 65190 -67865  172153 1970
 86470.3 65175 -67862  172149 1965
 86475.3 65152 -67849  172147 1964
 86480.3 65103 -67845  172147 1966
 86485.3 65088 -67831  172148 1966
 86490.3 65130 -67823  172150 1964
 86495.3 65177 -67820  172151 1967
 86500.3 65212 -67813  172155 1968
 86505.3 65245 -67799  172156 1969
 86510.3 65281 -67795  172157 1968
 86515.3 65310 -67787  172158 1967
 86520.3 65333 -67773  172160 1968
...
```

B.3.2 Sample Meteorological Data File

```
29 1001
CHAN, Roland
NASA - Ames Research Center
Meteorological Data from ER-2's MMS
ASHOE/MAESA
1 1                                                    ;ivol nvol
1994 07 28   1994 07 30                                ;flight-date    process-date
0                                                      ;0=non-uniform time increment
Elapsed UT seconds of flight date
6                                                      ;number of primary variables
0.1    0.1   0.1   0.1   0.1   0.1                     ;scale factors
99999  9999  9999  9999  9999  9999                    ;missing values
Static Pressure (mb)
Static Temperature (deg K)
Theta - potential temperature (deg K)
U - horizontal E-W wind speed (m/s)
V - horizontal N-S wind speed (m/s)
W - vertical wind speed (m/s)
1
PRELIMINARY DATA
8
Using Po1 sn #1564, Wang calibrated June 1994
Configuration: LTN-92 + GPS + OH nose + Back_Up Tf sensor & Amplifier
1Hz data are desampled from 5Hz data.
5Hz data file is available upon request, containing: GMTS,Psta,Tsta,TAS,
U,V,W,LAT,LONG,PALT,POT,ROLL,HDG,PIT,Ydot,Xdot,Zdot,Q,YAW,AOA,MACH,Zdotdot,
YAWdp,AOAdp                              (approx. 3 Mbyte per flight hour)
h:\mms\e_940728.cv
GMT        Psta Tsta Thta   U    V    W
...
 86395.3    558 1903 4340  424   -5   -3
 86396.3    558 1903 4340  423   -7   -3
 86397.3    558 1903 4340  422   -6   -3
 86398.3    558 1903 4340  424   -7   -3
 86399.3    558 1903 4340  424   -7   -3
 86400.3    558 1903 4340  423   -7   -3
 86401.3    558 1903 4340  424   -7   -3
 86402.3    558 1903 4340  425   -6   -3
 86403.3    558 1903 4330  425   -5   -3
 86404.3    558 1903 4330  426   -6   -3
 86405.3    558 1903 4340  425   -7   -3
 86406.3    558 1903 4340  425   -7   -2
 86407.3    558 1903 4340  426   -7   -2
 86408.3    558 1903 4340  425   -8   -2
 86409.3    558 1903 4340  425   -9   -2
 86410.3    558 1903 4340  425  -10   -2
 86411.3    558 1903 4340  425  -10   -2
 86412.3    558 1903 4340  425  -10   -2
 86413.3    558 1903 4340  425  -11   -2
 86414.3    558 1903 4340  426  -11   -2
 86415.3    558 1903 4340  425  -12   -2
 86416.3    558 1903 4340  425  -12   -2
 86417.3    558 1903 4340  426  -13   -2
 86418.3    558 1903 4340  426  -14   -2
 86419.3    558 1903 4340  425  -15   -2
 86420.3    558 1903 4340  426  -15   -2
...
```

B.3.3 Sample ALIAS Data File

```
21   1001
Webster, Chris   May, Randy
JPL
ALIAS
ASHOE
1   1
1994 07 28    1994 07 30
0
Elapsed UT seconds from 0 hours on the takeoff date
5
1.0e-9 1.0e-9 1.0e-9 1.0e-9 1.0e-9
9999 9999 9999 9999 9999
N2O  volume mixing ratio
CH4  volume mixing ratio
NO2 volume mixing ratio
HCL  volume mixing ratio
CO  volume mixing ratio
1
ALIAS PRELIMINARY DATA.
1
 Time     N2O      CH4       NO2       HCL       CO
...
86395.0 223.03 1283.08 9999.000 9999.000 5.753
86399.0 222.46 1289.55 9999.000 9999.000 5.739
86403.0 222.35 1288.18 9999.000 9999.000 5.706
86406.0 223.59 1289.99 9999.000 9999.000 5.730
86410.0 224.88 1296.44 9999.000 9999.000 5.769
86413.0 225.42 1298.10 9999.000 9999.000 5.799
86417.0 226.11 1297.50 9999.000 9999.000 5.867
86421.0 225.67 1296.35 9999.000 9999.000 5.926
86429.0 226.14 1294.67 9999.000 9999.000 5.980
86433.0 225.56 1293.38 9999.000 9999.000 6.019
86437.0 225.21 1293.48 9999.000 9999.000 6.007
86440.0 224.98 1292.21 9999.000 9999.000 5.958
86444.0 224.41 1291.30 9999.000 9999.000 5.849
86447.0 223.42 1288.59 9999.000 9999.000 5.805
86451.0 224.35 1288.44 9999.000 9999.000 5.805
86455.0 224.35 1288.35 9999.000 9999.000 5.930
86458.0 225.05 1288.48 9999.000 9999.000 5.915
86466.0 226.45 1288.19 9999.000 9999.000 5.871
86470.0 227.73 1291.78 9999.000 9999.000 5.862
86473.0 228.54 1292.94 9999.000 9999.000 5.788
86477.0 228.75 1292.72 9999.000 9999.000 5.806
86480.0 227.38 1294.06 9999.000 9999.000 5.847
86484.0 226.55 1294.55 9999.000 9999.000 5.980
86488.0 225.74 1291.68 9999.000 9999.000 6.142
86491.0 224.06 1290.91 9999.000 9999.000 6.109
86495.0 223.88 1292.48 9999.000 9999.000 5.984
86503.0 223.37 1290.26 9999.000 9999.000 5.887
86506.0 224.86 1294.35 9999.000 9999.000 5.781
86510.0 227.70 1297.70 9999.000 9999.000 5.719
86514.0 227.88 1298.34 9999.000 9999.000 5.743
86517.0 227.60 1297.05 9999.000 9999.000 5.895
86521.0 228.57 1298.94 9999.000 9999.000 5.969
...
```

References

Andrews, D.G., Holton, J.R. and Leovy, C.B., 1987. *Middle Atmosphere Dynamics.* Academic Press Inc., Orlando, Florida.

Bendorf, S.H., 1997. *Stratospheric Ozone Depletion over New Zealand.* Undergraduate Project Report, University of Canterbury, Christchurch, New Zealand.

Carver, G.D., Norton, W.A. and Pyle, J.A., 1994. A Case Study in Forecasting the Stratospheric Vortex During EASOE. *Geophys. Res. Lett.*, **21**, No. 13, 1451-1454.

Clough, S.A., Grahame, N.S. and O'Neill, A., 1985. Potential Vorticity in the Stratosphere Derived using Data from Satellites. *Q. J. R. Met. Soc.*, **111**, 335-358.

Dunford, A.J., 1997. *Radar Observations of Atmospheric Phenomena.* Ph.D. thesis, Department of Physics and Astronomy, University of Canterbury, Christchurch, New Zealand.

Fairlie, T.D., Pierce, R.B., Grose, W.L., Lingenfelser, G., Loewenstein, M. and Podolske, J.R., 1997. Lagrangian Forecasting During ASHOE/MAESA: Analysis of Predictive Skill for Analyzed and Reverse-Domain-Filled Potential Vorticity. *J. Geophys. Res.*, **102,** No. D11, 13169-13182.

Garcia, R.R. and Boville, B.A., 1994. "Downward Control" of the Mean Meridional Circulation and Temperature Distribution of the Polar Winter Stratosphere. *J. Atmos. Sci.*, **51**, No. 15, 2238-2245.

Gibbons, J.D., 1985. *Nonparametric Methods for Quantitative Analysis, 2nd Ed. American Series in Mathematical and Management Sciences*, Am. Sci. Press.

Hofmann, D.J. and Solomon, S., 1989. Ozone Destruction Through Heterogeneous Chemistry Following the Eruption of El Chicon. *J. Geophys. Res.*, **94**, No. D4, 5029-5041.

Hoskins, B.J., McIntyre, M.E. and Robertson, A.W., 1985. On the Use and Significance of Isentropic Potential Vorticity Maps. *Q. J. R. Met. Soc.*, **111**, No. 470, 877-946.

Lahoz, W.A., 1997. Predictive Skill of the UKMO Unified Model in the Southern Lower Stratosphere. Submitted to *Q. J. R. Met. Soc.*

Lawrence, B.N., 1997. Geophysical Fluid Dynamics – Lecture Notes for Physics 316. University of Canterbury, Christchurch, New Zealand.

Makhijani, A. and Gurney, K.R., 1995. *Mending the Ozone Hole: Science, Technology, and Policy.* The MIT Press, Cambridge, Massachusetts.

McIntyre, M.E. and Palmer, T.N., 1983. Breaking Planetary Waves in the Stratosphere. *Nature*, **305**, 593-600.

McIntyre, M.E. and Palmer, T.N., 1984. The 'Surf Zone' in the Stratosphere. *J. Atmos. Terr. Phys.*, **46**, No. 9, 825-849.

McIntyre, M.E. and Palmer, T.N., 1985. A Note on the General Concept of Wave Breaking for Rossby and Gravity Waves. *Pure Appl. Geophys.*, **123**, 964-975.

Manney, G.L., Zurek, R.W., O'Neill, A. and Swinbank, R., 1994. On the Motion of Air through the Stratospheric Polar Vortex. *J. Atmos. Sci.*, **51**, No. 20, 2973-2994.

Manney, G.L., Zurek, R.W., Lahoz, W.A., Harwood, R.S., Gille, J.C., Kumer, J.B., Mergenthaler, J.L., Roche, A.E., O'Neill, A., Swinbank, R. and Waters, J.W., 1995. Lagrangian Transport Calculations Using *UARS* Data. Part I: Passive Tracers. *J. Atmos. Sci.*, **52**, No. 17, 3049-3068.

Morris, G.A., Schoeberl, M.R., Sparling, L.C., Newman, P.A., Lait, L.R., Elson, L., Waters, J., Suttie, R.A., Roche, A., Kumer, J. and Russell, J.M.III, 1995. Trajectory Mapping and Applications to Data from the Upper Atmosphere Research Satellite. *J. Geophys. Res.*, **100**, No. D8, 16491-16505.

NASA ASHOE/MAESA CD-ROM, 1995. National Aeronautics and Space Administration, Ames Research Center, Moffett Field, California.

Nilsson, A., 1996. *Ultraviolet Reflections. Life Under a Thinning Ozone Layer.* John Wiley and Sons Inc., Chichester, England.

Pierce, R.B., Fairlie, T.D., Grose, W.L., Swinbank, R. and O'Neill, A., 1994. Mixing Processes within the Polar Night Jet. *J. Atmos. Sci.*, **51**, No. 20, 2957-2972.

Pitari, G., Visconti, G. and Verdecchia, M., 1992. Global Ozone Depletion and the Antarctic Ozone Hole. *J. Geophys. Res.*, **97**, No. D8, 8075-8082.

Polvani, L.M. and Plumb, R.A., 1992. Rossby Wave Breaking, Microbreaking, Filamentation, and Secondary Vortex Formation: The Dynamics of a Perturbed Vortex. *J. Atmos. Sci.*, **49**, No. 6, 462-476.

Pyle, J.A., Harris, N.R.P., Farman, J.C., Arnold, F., Braathen, G., Cox, R.A., Faucon, P., Jones, R.L., Megie, G., O'Niell, A., Platt, U., Pommereau, J.-P., Schmidt, U. and Stordal, F., 1994. An Overview of the EASOE Campaign. *Geophys. Res. Lett.*, **21**, No. 13, 1191-1194.

Randel, W.J., 1987. The Evaluation of Winds from Geopotential Height Data in the Stratosphere. *J. Atmos. Sci.*, **44**, No. 20, 3097-3120.

Rosier, S.M., 1996. *Dynamical Evolution of the Northern Stratosphere in Early Winter, 1991/92: Observational and Modelling Studies.* Ph.D. thesis, Department of Physics, University of Oxford, Oxford, Great Britain.

Salby, M.L. and Garcia, R.R., 1990. Dynamical Perturbations to the Ozone Layer. *Physics Today*, **43**, No. 3, 38-46.

Schoeberl, M.R., Lait, L.R., Newman, P.A. and Rosenfield, J.E., 1992. The Structure of the Polar Vortex. *J. Geophys. Res.*, **97**, No. D8, 7859-7882.

Schoeberl, M.R. and Newman, P.A., 1995. A Multiple-Level Trajectory Analysis of Vortex Filaments. *J. Geophys. Res.*, **100**, No. D12, 25801-25815.

Sutton, R., 1994. Lagrangian Flow in the Middle Atmosphere. *Q. J. R. Met. Soc.*, **120**, 1299-1321

Sutton, R.T., MacLean, H., Swinbank, R., O'Neill, A. and Taylor, F.W., 1994. High-Resolution Stratospheric Tracer Fields Estimated from Satellite Observations Using Lagrangian Trajectory Calculations. *J. Atmos. Sci.*, **51**, No. 20, 2995-3005.

Swinbank, R. and O'Neill, A., 1994. A Stratosphere-Troposphere Data Assimilation System. *Mon. Wea. Rev.*, **122**, 686-702.

Tuck, A.F., Watson, R.T., Condon, E.P., Margitan, J.J. and Toon, O.B., 1987. The Planning and Execution of ER-2 and DC-8 Aircraft Flights over Antarctica, August and September 1987. *J. Geophys. Res.*, **94**, No. D9, 11181-11222.

Tuck, A.F., Brune, W.H. and Hipsind, R.S., 1997. Airborne Southern Hemisphere Ozone Experiment/Measurements for Assessing the Effects of Stratospheric Aircraft (ASHOE/MAESA): A Road Map. *J. Geophys. Res.*, **102**, No. D3, 3901-3904.

Waugh, D.W., Plumb, R.A., Atkinson, R.J., Schoeberl, M.R., Lait, L.R., Newman, P.A., Lowenstein, M., Toohey, D.W., Avallone, L.M., Webster, C.R. and May R.D., 1994. Transport out of the Lower Stratospheric Arctic Vortex by Rossby Wave Breaking. *J. Geophys. Res.*, **99**, No. D1, 1071-1088.

Waugh, D.W. and Plumb, R.A., 1994. Contour Advection with Surgery: A Technique for Investigating Finescale Structure in Tracer Transport. *J. Atmos. Sci.*, **51**, No. 4, 530-540.

Waugh, D.W., 1996. Elliptical Diagnostics of Stratospheric Polar Vortices. Submitted to *Q. J. R. Met. Soc.*

Waugh, D.W., Plumb, R.A., Elkins, J.W., Fahey, D.W., Boering, K.A., Dutton, G.S., Volk, C.M., Keim, E., Gao, R.-S., Daube, B.C., Wofsy, S.C., Lowenstein, M., Podolske, J.R., Chan, K.R., Proffitt, M.H., Kelly, K.K., Newman, P.A. and Lait, L.R., 1997. Mixing of Polar Vortex Air into Middle Latitudes as Revealed by Tracer-Tracer Scatterplots. *J. Geophys. Res.*, **102**, No. D11, 13119-13134.

Waugh, D.W., Sisson, J.M. and Karoly, D.J., 1997. Predictive Skill of a NWP Model in the Southern Lower Stratosphere. Submitted to *Q. J. R. Met. Soc.*

World Meteorological Organisation. *Scientific Assessment of Ozone Depletion: 1994.* Global Ozone Research and Monitoring Project – Report No. 37. Geneva, Switzerland.

Zeilik, M. and Smith, E.v.P., 1987. *Introductory Astronomy and Astrophysics, 2nd Edn.* Saunders College Publishing, Philadelphia.